UiT
THE ARCTIC
UNIVERSITY
OF NORWAY
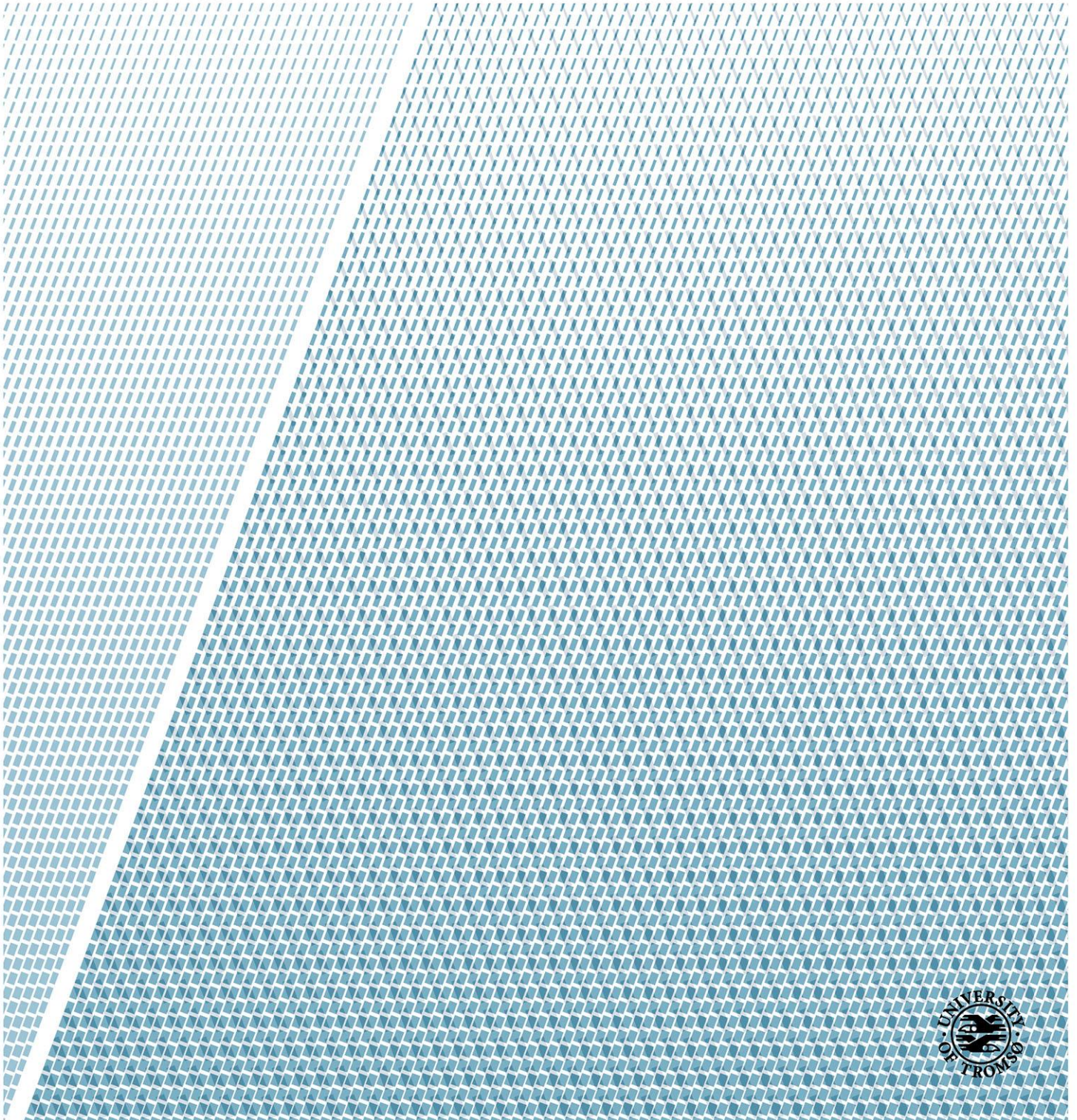
Faculty of Science and Technology

A detailed Investigation of a Geological CO$_2$-Storage Reservoir

—

Anna Maria Hatland
Master's Thesis in Energy, Climate and Environment, EOM-3901, June 2015

UNIVERSITY OF TROMSØ

Abstract

Increased CO_2-concentrations within the atmosphere of the Earth have encouraged development of "carbon capture and storage" (CCS). It is important to avoid global warming, and CO_2 may be stored within geological formations in the subsurface. This thesis focuses on the possibilities of storing CO_2 in a reservoir of Middle Triassic-Middle Jurassic age in The Nordkapp Basin, The Southern Barents Sea. The thesis tries to map out the extent of a reservoir and a cap rock, calculate the amount of injectable CO_2, and assess the potential risks of leakage for the CO_2-storage complex.

The evaluation is based on a migrated 3D-seismic dataset, ST9403, with 7228/7-1A as a reference well. The well penetrates several formations, where the formations of Stø-Tubåen are considered the best reservoir unit, consisting of a homogenous sandstone with good properties. The cap rock constitutes the formations of Hekkingen and Fuglen, which is tight, covering and homogenous. The trap type is linked to extensive salt domes, enclosed by faulted structures. The salt domes are stable and the faults inactive and tight. Possible hazardous, chemical reactions between the salt, the injected CO_2 and a Permian carbonate are considered the largest safety risks for the CO_2-storage complex.

I

II

Acknowledgements

IV

"It's not a Great Wall. It's an all right wall. It's The all right Wall of China".

- Karl Pilkington

VI

Table of Contents

1   Introduction

1.1   Objective

The objective of this master's thesis is to evaluate and map out structures in The Nordkapp Basin and investigate the possibility of storing CO_2 in a geological reservoir of Middle Triassic-Middle Jurassic age. The reservoir comprises parts of the stratigraphic formations Stø, Nordmela, Tubåen, Fruholmen and Snadd, encountered in 7228/7-1A (NPD, 2015). This well will function as an injection- and reference well for this thesis. The evaluation of geological extensiveness and properties are based on interpretation of seismic data with additional information from the well logs of 7228/7-1. A storage capacity calculation and a risk table for the CO_2-storage complex will be included at the end.

1.2   Increased CO_2 in the Atmosphere

The climate of the Earth is changing. Rising sea levels, a growing number of wildfires, more extreme rainfalls and longer drought periods are only some observed changes. Global temperatures are increasing, the ice in the polar regions is melting and floods are occurring more frequently (IPCC, 2014). Moreover, these changes seem to be accelerating. Why is this occurring?

1.2.1   The Greenhouse Effect

Variations in the climate have occurred throughout the times. Natural variability causes a change in the average temperatures of the Earth, making the climate colder or warmer. The climate is still changing as a part of a natural cycle, but an increasing number of scientists are agreeing upon humanity both affecting and accelerating these natural fluctuations (Cohen, 2010). The Intergovernmental Panel on Climate Change (IPCC) has concluded that humanity has accelerated global warming for the last 50-60 years with a certainty of 90% (IPCC, 2007). A recent report states:

> *Anthropogenic greenhouse gas emissions (GHGs)…are now higher than ever. Their effects,…have been detected throughout the climate system and are **extremely likely** to have been the dominant cause of the observed global warming… (IPCC, 2014).*

These GHGs are carbon dioxide (CO_2), methane (CH_4), nitrous oxide (N_2O) and fluor-inated gases (HFCs, PFCs and SF_6), where CO_2 is considered to be the main contributor. GHGs

are gases that trap the incoming radiation (ultraviolet light) from the Sun in the atmosphere of the Earth, and prevent the heat (infrared light) from escaping. This trapping mechanism is known as "The Greenhouse Effect" (Figure 1-1).
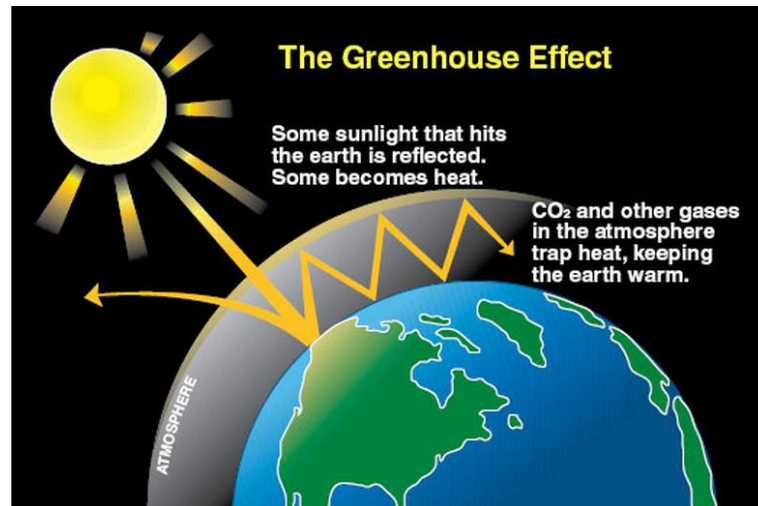
Figure 1-1: "The Greenhouse Effect" is caused by GHGs inhibiting heat to escape from the atmosphere. After Department of Ecology (n.d.).

1.2.2   Increasing CO_2-Emissions

CO_2 is considered to be the main contributor to the increasing greenhouse effect (Figure 1-2A). Almost 80% of the total GHG-emissions come from CO_2. The abundancy of CO_2 is primarily due to the combustion of fossil fuel, such as coal, oil and gas, which are mainly composed of hydrogen and carbon. Fossil fuel is used for e.g. electricity, transportation and industry. In addition to fossil fuel, CO_2-levels increase as a result of deforestation, decay of biomass etc. (The National Research Council, 1984, IPCC, 2005, IPCC, 2007, IPCC, 2014).

The largest fossil fuel contributor to the CO_2-emissions is coal (Figure 1-2B). Approximately 60% of the global CO_2-emissions are emitted from coal-power plants. Capturing of CO_2 from coal-power plants is therefore considered particularly important in reduction of the global CO_2-emissions (Koeijer et al., 2013).

Figure 1-2: A) Shares of anthropogenic greenhouse gas emissions by origin. CO₂ is the largest contributor to GHG-emissions (91%). Modified after IPCC (2007). B) Shares of global anthropogenic CO₂-sources. The main contributor (60%) is coal. Modified after Koeijer et al. (2013).

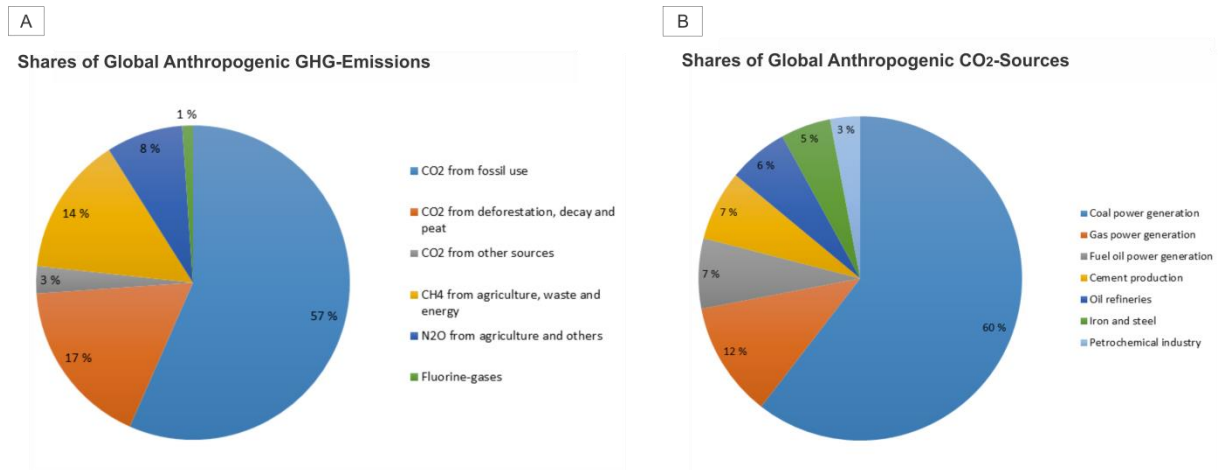Combustion of fossil fuel adds about 8 billion tons of CO_2 to the environment every year. Some of this is taken up by "carbon sinks", such as the ocean and the land biosphere, but an average of 4 billion tons of CO_2 is added annually to the Earth's atmosphere. Predictions state that if the world does not reduce the CO_2-emissions now, it will be adding 16 billion tons CO_2 to the atmosphere every year, by 2050 (Hotinski, 2011, Büenz et al., 2014).

Scientific observations indicate that the growing CO_2-emissions have resulted in a global mean temperature increase of 0.6°C since the 19th century. The "global goal" is considered to stay below an average temperature increase of 2°C. However, this goal demands instantly, severe reductions in emission rates.

1.3 Mitigation Options

How may the increasing CO_2-emissions be avoided?

1.3.1 The Kyoto Protocol

The European Union (EU) is currently attempting to mitigate the increasing global CO_2-emissions through e.g. The Kyoto-Protocol. The participating countries need to reduce their total GHG-emissions in 2020 by 20% from 1990-levels. The protocol has been signed by 192 countries, and the countries try to inhibit their emissions by e.g. buying emission allowances, a so-called "cap-and-trade" system or invest in greener technologies (Böhringer et al., 2009, GLOBALIS, n.d., Bruvoll and Larsen, 2004). However, The Kyoto-Protocol has been criticized for several shortcomings, e.g. by affecting some countries to a larger extent than others

(Böhringer et al., 2009). An overview of the largest GHG-contributors is displayed in Figure 1-3.
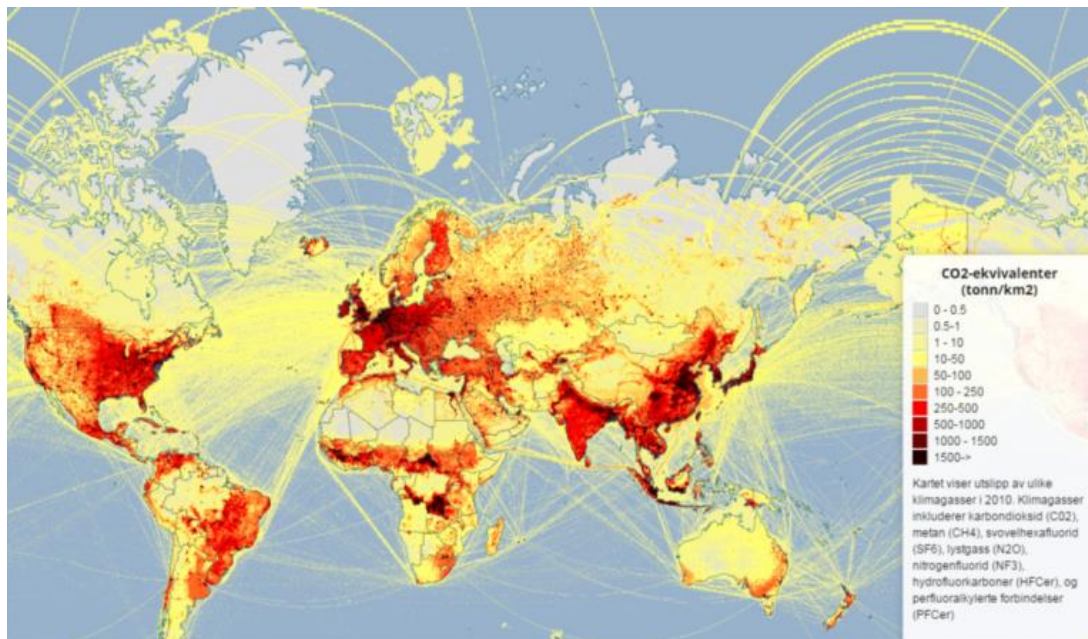
Figure 1-3: The figure displays countries emitting GHGs in CO₂-equivalents in t/km2 in 2010. Countries like India, China, the U.S.A and EU-countries are currently emitting the most extensive amount of CO₂ (GLOBALIS, n.d.).

1.3.2   Carbon Tax

Another solution to a reduction in CO_2-emissions is carbon taxes. A "carbon tax" or a "carbon fee" is a fee placed on greenhouse gas pollutants, often burning fossil fuels, such as carbon-based fuels or pollution from industrial processes (Poterba, 1991). This solution has proven to be one of the most powerful incentives to reduce CO_2-emissions in a country, such as Norway (a fee of \$50/t released CO_2 from gasoline) (Herzog, 1998, Bruvoll and Larsen, 2004). The tax is an encouragement for industry and households to invest in cleaner technologies. This may increase the demand for completely new and more energy-efficient products, or stimulate innovation and investment within already developing sciences, such as carbon-capture and storage (CCS) (Bruvoll and Larsen, 2004).

1.3.3   The Stabilization Triangle

So far, carbon taxes and protocols are listed as possible solutions to mitigate CO_2-emissions. But what options exists to actually emit less CO_2? What other energy sources are available?

The Carbon Mitigation Initiative proposes a possible solution. This is visualized as "The Stabilization Triangle" (Figure 1-4A), a so called "flat path". This flat path implies that the

current level of emitted CO_2 needs to be held constant (8 billion per annum), until 2050, to avoid the worst predicted climate-scenarios. The worst scenario is depicted as where 16 billion tons CO_2 is emitted to the atmosphere every year (the "business as usual"-path). This means 8 billion CO_2-emissions need to be replaced by other sources of energy. Each solution, proposed by the CMI, amounts to 1 billion tons of CO_2-equivalents. 8 different solutions, out of 15 suggested possibilities, therefore need to be implemented, and these solutions are all currently available forms of sciences (Hotinski, 2011). Generally, these 15 different implementations can be divided into 5 categories:

1. *Renewables and Bio-Storage*

The world needs to start producing electricity based on an increased amount of solar or wind. Replacement of fossil fuel by biofuel, or hydrogen fuel from wind, is also an option. Storage in forests or in the Earth's soil is a feasible, additional solution.

2. *Increased Efficiency and Conservation*

Increased efficiency in transport is a probable solution. Less travelling and a growing number of mass transit options are also achievable. Increased efficiency in buildings and electricity production is needed, together with reductions in the emissions of new buildings. The same effect may be achieved by doubling the efficiency for coal plants in electricity-production.

3. *Fuel Switching*

Electricity is produced on a large scale from coal-based power plants. These power plants can be changed for natural gas plants, as natural gas has lower carbon content.

4. *Nuclear Energy*

Today, nuclear fission provides 17% of the global electricity. By replacing coal-electric plants with nuclear, the number of nuclear power plants needs to be tripled. Nuclear power plants produce no CO_2.

5. *Carbon-Capture and Storage (CCS)*

The world is able to continue to use coal, gas and oil (fossil fuel) in the future, if the waste CO_2 is not vented to the atmosphere. CO_2 may be captured at large power plants and stored underground. This is called "carbon-capture and storage" (CCS). CCs may be applied to e.g.

large coal-power plants, gas-power plants, hydrogen-power plants or coal-based synfuel facilities (Hotinski, 2011).

A quick summary of these different mitigation options are displayed in Figure 1-4B below. In addition to the solutions proposed by the CMI (Hotinski, 2011), a reduction in consumption is also added as a possible option to mitigate climate change.
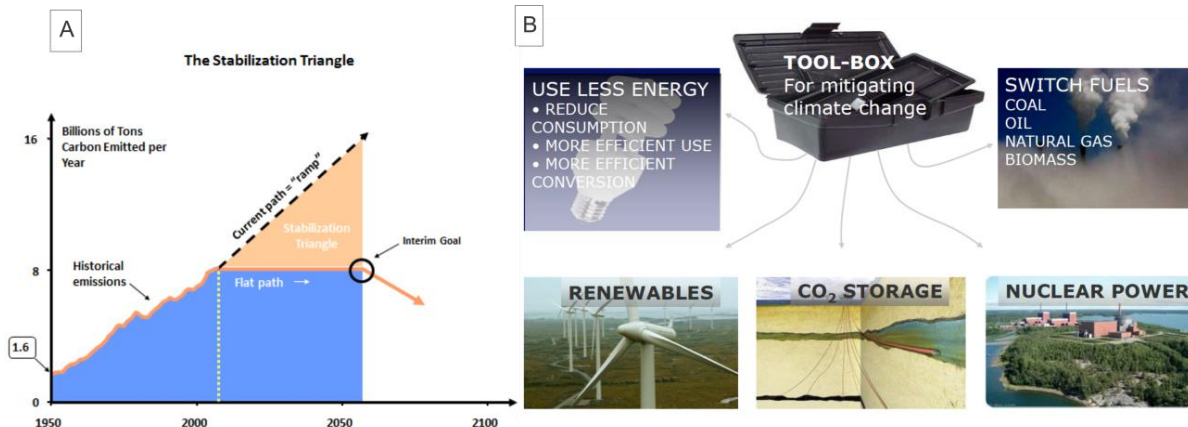

Figure 1-4: A) The predicted increase in CO$_2$-emissions by 2050. To avoid the worst global climate changes a "flat path" in CO$_2$-emissions needs to be implemented. This involves replacing some of the future global energy suppliers with other solutions. After Hotinski (2011). B) The "toolbox" is a quick summary of what society needs to do in the future to mitigate climate change. This toolbox involves fuel-switching, increased use of renewables and/or nuclear power, reduced consumption, higher efficiency in energy extraction or CCS. The toolbox displays the proposals made by CMI, with an additional option of a reduction in consumption. After Koeijer et al. (2013).

1.4 Carbon-Capture and Storage

CCS may be applied to more facilities than the examples listed above. Everywhere in the world, where the CO$_2$-emissions are extensive, and circumstances make it economical and feasible to achieve, CCS may be applied.

1.4.1 What is CCS?

As mentioned in the previous subsections, CCS is a short form of "carbon-capture and storage" or "carbon-capture and sequestration". The scope of CCS involves the science of capturing CO$_2$ from an industrial- or energy-related source, the transport of it to the storage point, and the long-term storage in the subsurface. The storage may be conducted on land or offshore and the goal of CCS is to prevent CO$_2$ from leaking to the atmosphere and pollute the environment (IPCC, 2005).

CO$_2$ is emitted from fossil fuel facilities (oil, gas and coal), biomass facilities and from industrial processes. Combustion fuels are often used in industry to e.g. produce electricity,

cement or steel, and are important factors in chemical plants and other refineries. The emitted CO_2 from these large point sources may then be captured and stored.

Three different storing techniques are available today for CO_2-storage. These techniques are industrial storage, oceanic storage and geological storage of CO_2. Industrial storage involves fixation of CO_2 into inorganic carbonates, oceanic storage leads to storage of CO_2 within the oceanic water column or on the deep seabed, and geological storage includes storage of CO_2 within the pores of a reservoir rock. As mentioned in section 1.1, the focus of this thesis will be on geological storage. This will be further addressed in section 1.4.2.

An overview of the entire CO_2-capture process, from the extraction of fuels to processing and storage options, is displayed in Figure 1-5 (Büenz et al., 2014, IPCC, 2005).
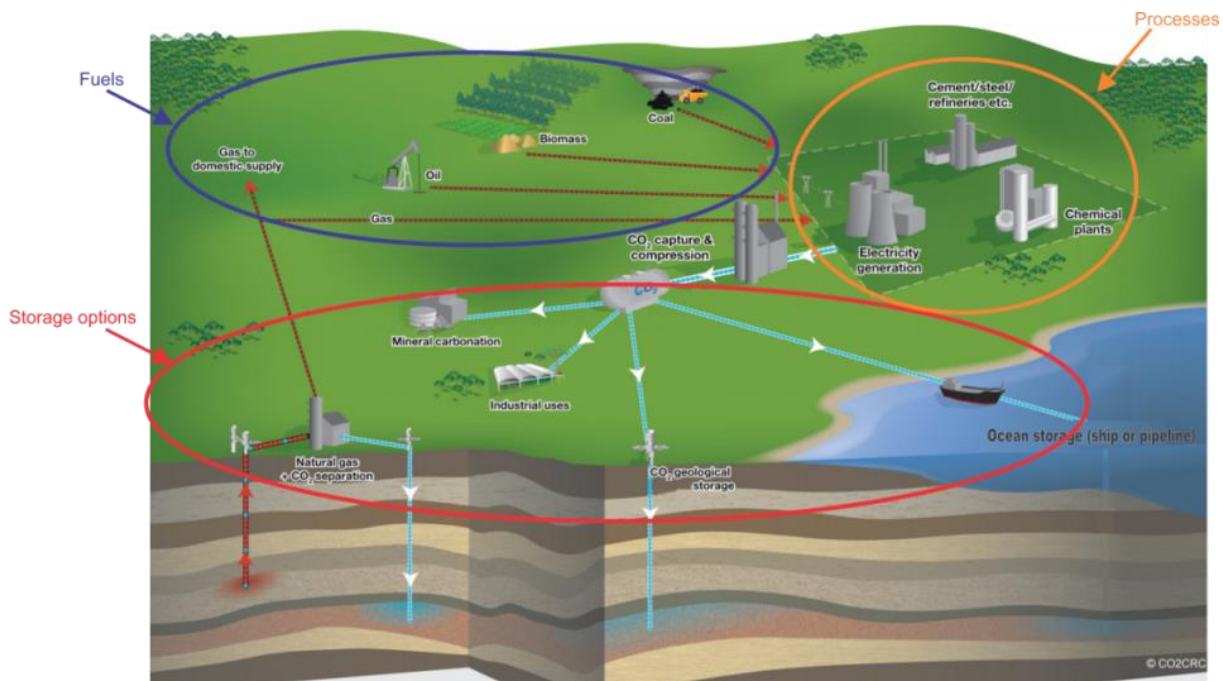
Figure 1-5: Carbon-capture and storage overview. Different fuels are marked in blue (coal, biomass etc.), refining processes in orange (chemical plants, electricity etc.) and different storage alternatives in red (industrial uses with mineral carbonation, CO_2-storage in the ocean water column, or on the deep seabed, and CO_2-storage within a geolocal formation. Modified after CO_2 CRC Limited (2011).

1.4.1.1 Public Concerns

Are there any public concerns related to CCS? The answer is "yes", as the general public opinion is often characterized by the term *"Not in my backyard!"* This concern is partially related to general ignorance, as a new and strange form of science seems intimidating, but also due to knowledge about what a possible disaster a CO_2-leakage might cause. Leaking CO_2 from natural reservoirs have proven earlier to be fatal to human health (Koeijer et al., 2013). In

Mammoth Mountain, California, in the 1990s, three deaths and several symptoms of early-stage human asphyxia were linked to CO_2 leaking from a natural reservoir in the area. Measurements of >95% CO_2 were observed close to the seepage site. CO_2 is denser than air, and replaces the air on the ground. A CO_2-content of >10% is usually toxic to humans. It is also tasteless, odorless and colorless at concentrations beneath 20%, which makes it difficult to register without suitable equipment. In addition, an even more dramatic episode took place near Lake Nyos, Cameroon in 1986. More than 1700 people died of asphyxiation, as a result of a limnic eruption of CO_2 from the lake (Bruant et al., 2002).

1.4.1.2 *Storage Facilities and Economics*

In Norway, CCS is implemented at The Sleipner Site in The North Sea, and The Snøhvit Site in The Barents Sea (Baklid and Korbøl, 1996, Hansen et al., 2013, Chadwick et al., 2004). CCS is implemented at these sites by injecting CO_2 into aquifers within the subsurface. A CCS-project is under investigation on land in Longyearbyen, Svalbard (Braathen et al., 2012). CCS-projects on land are often considered more economic, due to less travel distance and good infrastructure (Büenz et al., 2014), and land-projects are ongoing in e.g. In Salah, Algeria and The Rangely Project, U.S.A (Liu and Liang, 2011).

CCS is implemented in an effort to prevent the CO_2 from being vented to the atmosphere, but also due to economic reasons like carbon taxes and EU-legislations. In addition, there is a futuristic perspective to the CCS. Norway is leading within this field of science, and with its extensive knowledge Norway might be able to sell its expertise and services to other countries at a later stage (Halland et al., 2013, Büenz et al., 2014).

However, CCS is yet to be implemented on an extensive global scale. Many countries do not have carbon taxes and have not signed the Kyoto protocol, which leads to a high increase in expenses, if CCS is introduced. Calculations made by The CCS Institute of Canberra implied a rise of 80% in expenses, if CCS was to be implemented at a power plant. Half of these expenses are initial expenses, while the other half is related to operating costs (transport and injection/monitoring). An increase in efficiency will therefore lower these costs significantly. However, the general conclusion is undoubtedly that a power plant with CCS is more expensive than a power plant without CCS (Sivertsen and Hommedal, 2013, Liu and Liang, 2011).

1.4.2 Geological Site Characterization

The focus of this thesis will be on geological storage of CO_2, as mentioned in section 1.4.1. Geological site-characterization, with various trapping mechanisms, important reservoir properties and possible chemical reactions between the CO_2 and the reservoir, are therefore outlined in the following sections.

1.4.2.1 Different Geological Storage Sites

The most widespread form of CO_2-storage within geological storage sites are within depleted hydrocarbon (HC) reservoirs or deep saline water-saturated aquifers. In addition, CO_2-storage within salt caverns is also an option, together with enhanced coal bed methane-recovery or enhanced oil-recovery (EOR) (Lokhorst and Wildenborg, 2005). An overview of different geological storage sites is displayed in Figure 1-6.
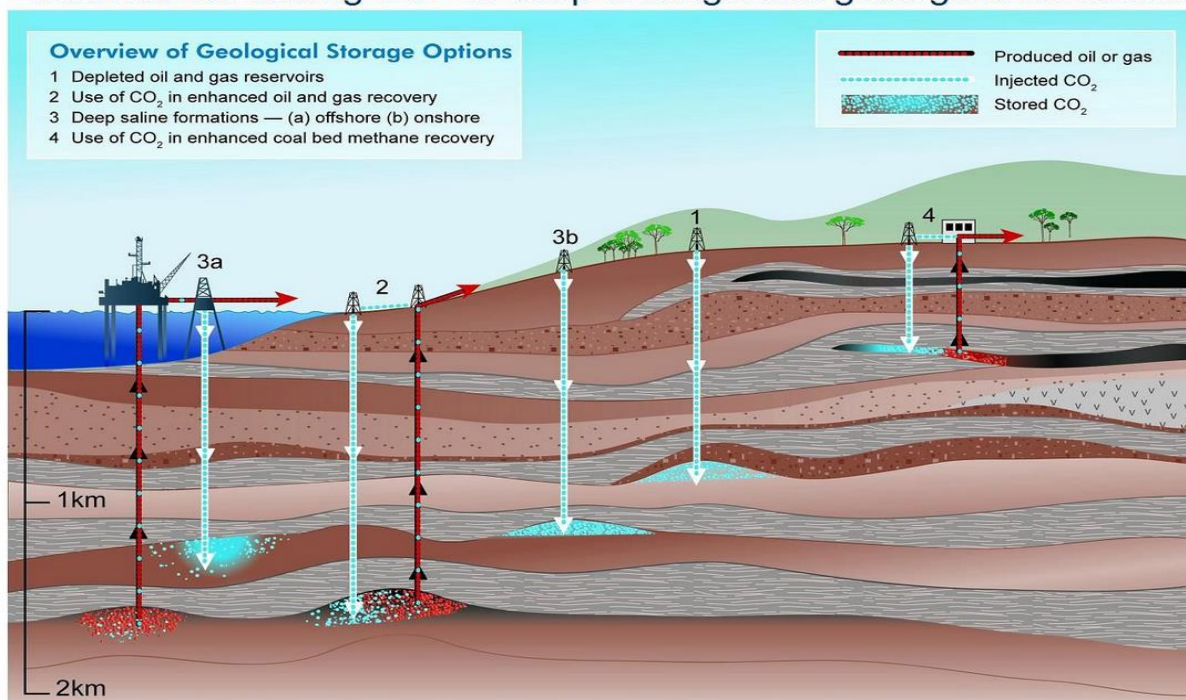
Figure 1-6: An overview of different geological storage options for CO_2. CO_2 may be stored in depleted oil and gas reservoirs (both onshore and offshore), be used in EOR, be stored in water-saturated deep saline formations (both onshore and offshore) or used in enhanced coal bed methane recovery. Storage in salt caverns is an addition option. After IPCC (2005).

1.4.2.2 Reservoir Characterization

Storage of CO_2 is implemented by injecting CO_2 through an injection well. The geological storage sites are often chosen due to their proximity to point sources of CO_2-emissions,

locations at reasonable depths and their placement within well-known, geologically mapped areas (Bruant et al., 2002).

Several aspects and quality requirements needs to be in place for a reservoir to be classified as a possible CO_2-storage. These qualities scope the rock's volume, its ability to contain fluids and its capacity to hold these fluids in place after injection. The qualities of a reservoir are often evaluated in the same manner as in the oil- and gas industry. The requirements for a geological site characterization involve e.g. measurements of the bulk volume, the porosity, permeability, injectivity, the storage efficiency factor (S_{eff}) and net-to-gross ratio (N/G). In addition, a reliable trapping mechanism and a suitable cap rock needs to be mapped and be present. This is crucial for the CO_2 to be held in place during and after injection (Rider, 1986, Selley and Sonnenberg, 1998, Koeijer et al., 2013).

One important factor in geological site characterization is estimations of the bulk volume. The bulk volume constitute the total area of the rock, including the pore volume and the matrix volume (volume of rock when pore volume is excluded). The bulk volume is generally measured when conducting site characterization by simply estimating the total volume of the formation. The pore volume within the rock, or the porosity, is a measurement of the void space within the formation. It is generally measured in percentages (%) and is often initially saturated with formation water. This available pore space determines the amount of injectable CO_2. The porosity of the formation is a complex factor to estimate for a geological reservoir, as it is highly dependent on burial depth, rate of burial, grain size of the formation etc. (Selley and Sonnenberg, 1998). Generally, an observable decrease in porosity (φ) with increased depth (z) is common to assume, and is given by The Athy Equation (Kawakita and Tsutsumi, 1966) displayed in Equation 1-1. The equation indicates that the original porosity (φ_0) decreases with depth (z). K is the compaction coefficient (m^{-1}), and is dependent on the particular formation. $\Phi(z)$ is the resulting compaction after burial.

$$\phi(z) = \phi_0 e^{-kz}$$

Equation 1-1: The Athy Equation. A general decrease in porosity with depth ($\varphi(z)$) is dependent on the compaction coefficient (k), initial porosity ($\varphi0$) and depth (z). The compaction coefficient is dependent on the particular formation.

The permeability is a measure of the fluid flow through the sediments. Permeability is measured in Darcy (D) and defines the injectivity of the reservoir. The higher the permeability, the easier it is to inject CO_2 into the reservoir (Halland et al., 2013, Selley and Sonnenberg, 1998, Rider, 1986, Koeijer et al., 2013). The permeability is, in resemblance to the porosity,

difficult to estimate accurately for a geological reservoir. Often a porosity- and permeability-range is calculated, based on results of e.g. burial-history of the area and information from analogous well logs. Well logs will be addressed further in section 1.4.2.5. A range is often more safe to utilize, as formations are generally having variable permeability- and porosity-values across the reservoir (Selley and Sonnenberg, 1998).

The storage efficiency factor (S_{eff}), when conducting a geological mapping of an area, is often the most difficult factor to calculate correctly. The S_{eff} estimates the fraction of pore space the injected CO_2 will occupy within the reservoir, and is therefore very difficult to calculate accurately pre-injection. The S_{eff} is therefore often based on a combination of available information regarding the CO_2-reservoir with additional information from analogous areas. Generally an S_{eff} above 5% for a reservoir is considered good (Halland et al., 2013).

The net-to-gross ratio of a reservoir imply the ratio of suitable reservoir rock relative to the total volume of the formation. When conducting geological mapping, N/G is based on e.g. well logs or core samples. Core samples give first-hand knowledge, and result in relative accurate measurements, while well logs are related to a higher degree of uncertainty. A high N/G is generally preferable (Selley and Sonnenberg, 1998, Halland et al., 2013).

1.4.2.3 Trapping Mechanisms

In addition to the factors mentioned above, the existence of a suitable trapping mechanism is crucial, to hold the migrating CO_2 in place after injection. To locate a reliable trap is therefore important. The most common traps, and consequently the most reliable, are listed below. These traps are e.g. structural trapping and stratigraphic trapping, located from geological mapping pre-injection. These traps form before injection starts. Residual-, solubility- and mineral-trapping occur within the formation after injection. Different combinations of such trapping mechanisms are common, and dependent on the content and flow within the reservoir (Selley and Sonnenberg, 1998, Halland et al., 2013).

i.   Structural traps are considered reliable traps, as they are very well explored by the HC-industry. Structural traps are made of structures forming or changing in the subsurface and the traps may form due to diapiric-, gravitational-, tectonic- or compactional processes, such as antliclines and faults (Selley and Sonnenberg, 1998).

ii. Stratigraphic traps are, in resemblance to structural traps, also considered reliable forms of trapping. Stratigraphic traps form due to changes in lithology of the subsurface. These

changes may be depositional or post-depositional, such as pinch-out traps against a non-porous sealing rock or unconformity traps due to erosion (Selley and Sonnenberg, 1998). The listed examples of different stratigraphic and structural traps are shown in Figure 1-7 below.
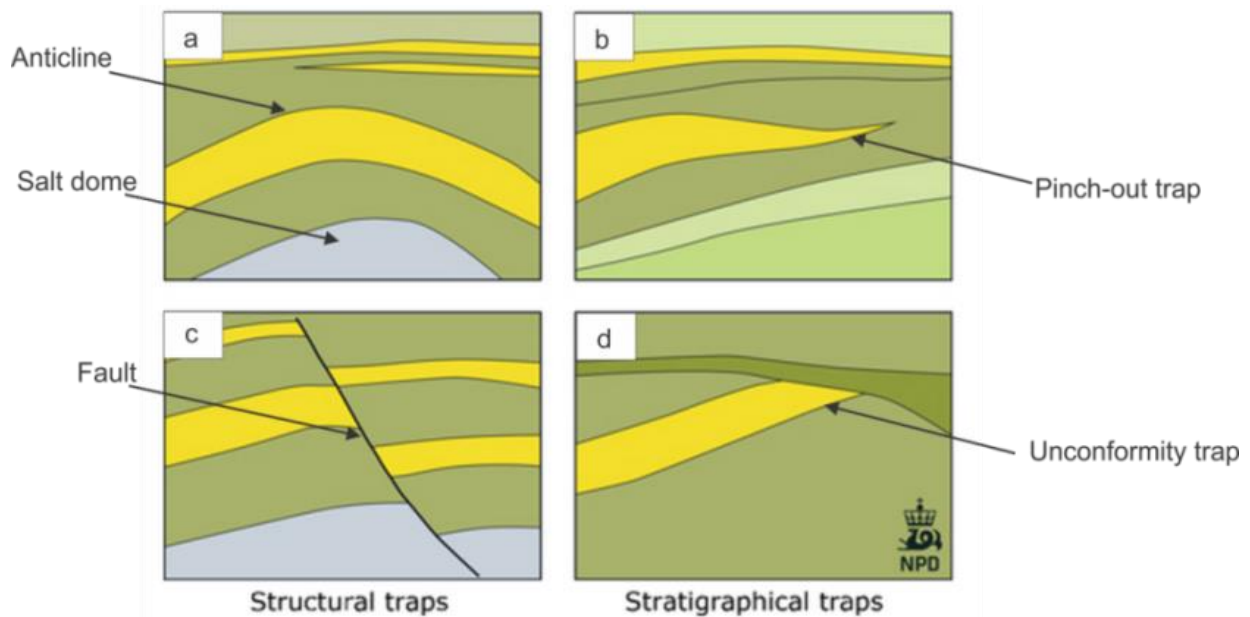

Figure 1-7: Some examples of structural and stratigraphical traps able to trap CO$_2$ in a reservoir. A) A diapir may form anticlines (deformation trap). B) A diapir can also form proximal pinch-out traps if it penetrates the sediments (post-depositon). C) A fault may form traps if the fault is tight (fault trap). D) Unconformity traps form from e.g. erosion (post-deposition). Modified after Halland et al. (2013).

iii.   Residual trapping occur after CO$_2$-injection and functions as an additional trap to the structural- or stratigraphic traps listed above. Residual trapping uses the capillary pressure of the pore throats to trap the CO$_2$ within the pores of the rock. Some gas bubbles are trapped within the pores as the CO$_2$ plume is migrating within the reservoir. When the CO$_2$-injection stops, the water moves back into the pores, which are now filled with CO$_2$. This added amount of water traps the CO$_2$ further, as the increased capillary pressure by the water column exceeds the buoyancy of the CO$_2$ (Hermanrud et al., 2009, Halland et al., 2013).

iv.   Some of the injected CO$_2$ will also dissolve in the water (approximately 10-20%). This is called solubility trapping. The reaction creates carbonic acid (H$_2$CO$_3$), a weak acid denser than the formation water (Equation 1-2). It therefore sinks towards the bottom of the reservoir and prevents the CO$_2$ from escaping through the cap rock (Büenz et al.,

2014, Koeijer et al., 2013). This reaction rate will increase with increased temperature (Izgec et al., 2006).

$$CO_2 + H_2O \leftrightarrow H_2CO_3 \leftrightarrow HCO_3^- + H^+ \leftrightarrow CO_3^{2-} + 2H^+$$
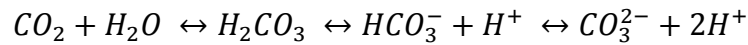
Equation 1-2: CO2 reacts with water (H2O) and forms carbonic acid (H2CO3). Carbonic acid precipitates bicarbonates (HCO_3^-) and carbonates (CO_3^{2-}) (salt) together with hydrons (H+-ions). These hydrons may alter the pH of the fluids in the formation, by making them more acidic. This acidification increases with an increase in temperature of the formation (Koeijer et al., 2013, Büenz et al., 2014, Izgec et al., 2006).

v. Mineral trapping is the last form of trapping, and is considered the safest and most stable form of CO_2-trapping. The minerals bond the CO_2 chemically to the matrix formation, and create new, sable minerals (Equation 1-3). However, this reaction may take thousands of years (Halland et al., 2013, Koeijer et al., 2013).

$$3K\ feldspar + 2H_2O + 2CO_2 \leftrightarrow 6\ SiO_2 + Muscovite + 2K^+ + 2HCO_3^-$$
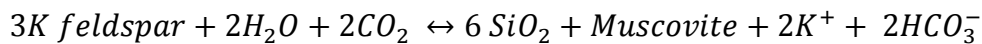
Equation 1-3: CO2 reacts with water (H2O) and the formation minerals (potassium feldspar) and forms bicarbonates ($2HCO_3^-$), quartz (SiO2), muscovite and potassium-ions (K+). This trapping mechanism may take thousands of years, but is considered the safest and most stable method of CO2-storage (Koeijer et al., 2013).

An overview of how different trapping mechanisms affect a reservoir over time is displayed in Figure 1-8. Structural- and stratigraphic traps are located during geological mapping (pre-injection), while residual-, solubility-, and mineral trapping occurs after injection.
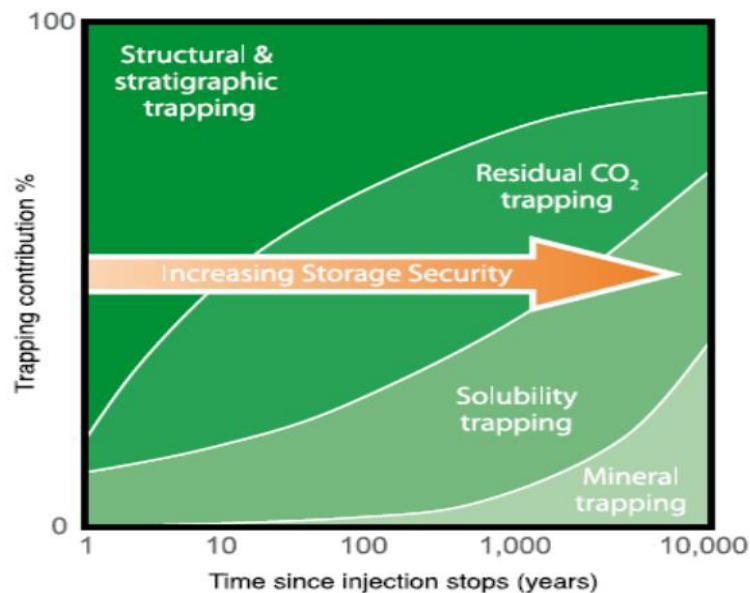

Figure 1-8: An overview of how different trapping mechanisms affect a reservoir over time. Structural and stratigraphic trapping is the initial form of trapping, but after injection of CO_2, the formation fluid is affected by residual, solubility, and mineral trapping. After Hermanrud et al. (2009).

13

1.4.2.4 Cap Rock Characterization

The cap rock is a low permeable lithological unit, which is able to prevent the CO_2 from escaping the trap. Therefore, when conducting a geological site characterization, the cap rock is crucial in relation to evaluation of leakage. If the cap rock is leaking, the risk of the CO_2 escaping is higher, and consequently the risk of failure of the CCS-project increases. To prevent this, the cap rock needs to be tight, extensive and preferably thick (Selley and Sonnenberg, 1998).

Various tools are available to map the thickness, tightness and extensiveness of a cap rock. Examples of such tools are seismic data and well logs (see section 1.4.2.5 below). A thickness of >50m is generally considered adequate for a cap rock, according to Halland et al. (2013). In general, a cap rock is considered safer with increasing thickness, and overburden, above the cap rock, may contribute as an additional seal (Selley and Sonnenberg, 1998).

However, leakage might occur through the cap rock, even if the cap rock is sufficiently thick. E.g. faults, extending through the cap rock, may contribute to leakage, if leakage occurs along the fault plane. Leakage might also occur if the cap rock is not extensive enough to cover the whole reservoir. The CO_2 may then migrate beyond the extent of the cap rock and escape, even if the cap rock is thick enough elsewhere. Shale, anhydrite ($CaSO_4$) and salt (NaCl) are generally considered reliable cap rocks (Selley and Sonnenberg, 1998). This is due to relatively impermeable properties of the rock formations, in permeability ranges of 10^{-6}-10^{-8} Darcy (Schlumberger, 2015).

1.4.2.5 Well Logs

Well logs give valuable information about the physical properties of a lithological unit, as outlined in section 1.4.2.2 and 1.4.2.4, and is hence a useful tool in geological site characterization. Well logs may provide information through e.g. gamma logs, sonic logs, resistivity logs, density logs and caliper logs, and are useful tools in measuring lithology, formation fluids, density, borehole size and other physical parameters of both the cap rock and the reservoir. Other logs are neutron porosity logs (measuring amounts of hydrogen), SP logs (measuring electric potential) and magnetic resonance logs (measuring the nuclear magnetic resonance response) (Rider, 1986), but these are beyond the scope of this thesis, and will consequently not be further explained.

A gamma log response (GR) is a record of the radioactivity of the formation. Different rocks results in various GR-responses, and makes it possible to differentiate e.g. a shaly cap rock from a sandy reservoir. The ability of the formation to transmit sound waves is measured by the sonic log (the acoustic log). The sonic is closely linked to porosity measurements, as mentioned in section 1.4.2.2. The resistivity log is important in estimations of presence, phase and saturation of formation fluids. The resistivity measures the ability of the formation to conduct electricity and varies with pore fluids., as noted in Selley and Sonnenberg (1998) and Rider (1986). The density log measures the overall bulk density of the formation. The caliper log measures the size and shape of the borehole. The caliper log may therefore indicate possible cave-ins inside the borehole, which could have affected other log measurements. For more information about well logs, see Rider (1986) and Selley and Sonnenberg (1998).

1.4.2.6   Chemical Properties

Some chemical properties of the CO_2 are important to highlight, to estimate injection and reactions within geological formations. This is e.g. to avoid leakage from the reservoir and pressure build-up scenarios.

1.4.2.6.1   Reservoir Conditions

The CO_2 is injected as a supercritical fluid. CO_2 in a supercritical state takes up the least amount of space within the reservoir, but still has a lower density than the surrounding formation fluids (e.g. water). The CO_2 will then gain the migration benefits of a gas, but hold the volume advantages of a fluid. This enables the CO_2 to diffuse relatively easy through the pore spaces and occupy the minimum amount of space within the reservoir.

CO_2 is in a supercritical phase above 31.1°C and 73.9 bar as displayed in Figure 1-9 (Bruant et al., 2002). If an assumed geothermal gradient of 30°C/km and a pressure gradient of 105bar/km of The Nordkapp Basin is used (Bugge et al., 2002), then the injected CO_2 may be stored in a supercritical state at approximately 800m below seabed. This means that the injection depth needs to be greater than 800m to achieve the beneficial properties. However, if water is assumed to contain 15% total dissolved solids by mass, this buoyancy effect is lost below 5000m (Pruess, 2008). Therefore, storage within the interval of 800-5000m is preferable, but still as high up as possible for economic reasons.
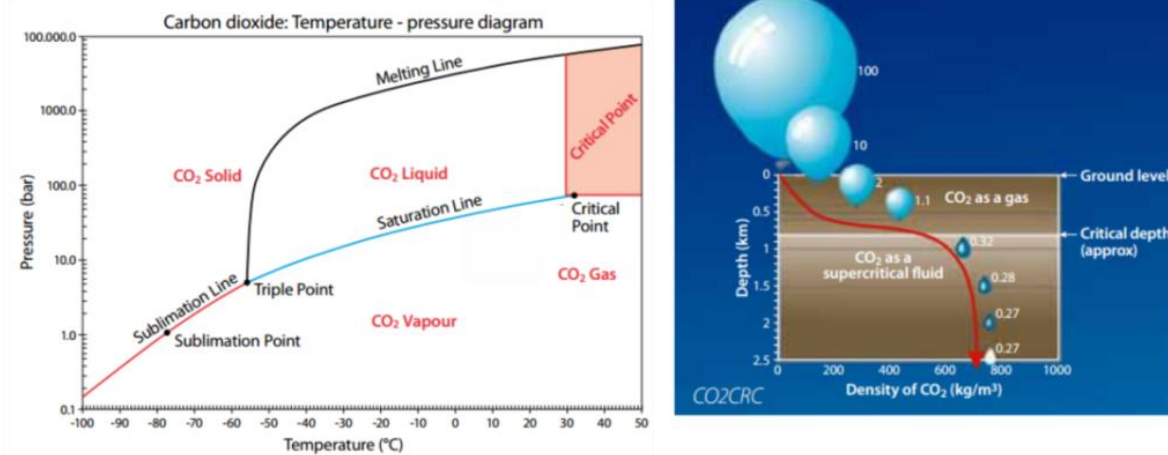
Figure 1-9: A visualization of approximate depth for CO₂ to be stored as a supercritical fluid (>800m within The Nord-kapp Basin). At such reservoir conditions, the CO₂ has the migration properties of a gas while it still holds the volume properties of a fluid. After Halland et al. (2013).

The CO_2 is injected at a pressure less than the fracturing pressure (the pressure causing the formation to fracture hydraulically), but larger than the capillary pressure (the pressure needed to enter a pore throat). This is to force the CO_2 to distribute across the reservoir. The injection pressure will remain constant throughout the injection period, and avoid pressure build-up, if the formation is in contact with e.g. a larger aquifer. The injected CO_2 will then push the water further away, as the injection proceeds, and avoid overpressure-scenarios. Pressure build-up scenarios may cause considerable damage to well equipment, or fracture the cap rock, and hence release the CO_2. This is therefore important to avoid at all costs (Halland et al., 2013, Koeijer et al., 2013, Holloway, 2005).

1.4.2.6.2   CO₂-Reactions with Salt

CO_2 may be stored in salt caverns, as mentioned in section 1.4.2.1. In addition, salt may act as a trap or seal within a CO_2-reservoir. This is due to salt often show good sealing properties (Lokhorst and Wildenborg, 2005, Bachu, 2000). Salt-related traps will be discussed further in section 5.2.3.1.

Salt caverns are generally used for temporary CO_2-storage. Caverns are considered uneconomical for long-term storage, due to associated high costs and waste causing significant environmental problems (Bachu, 2000). CO_2-storage within a deep-saline formation, with a limited amount of halite, may therefore be a better solution. Salt domes often limit an underground reservoir in only a few directions, and has therefore less costs and environmental impacts associated with it.

However, the salt reacts geochemically with the injected CO_2 and the reservoir. Salty water (brine) absorbs less CO_2 than brackish water. A salt dome within a basic siliciclastic reservoir may increase the salt content of the water, and therefore decrease the geochemical reactions of the CO_2 with the formation fluid (e.g. solubility- and mineral trapping). This could possibly lead to a pressure build-up within the reservoir, as a result of less dissolved CO_2.

An increase in salt content of the formation fluid may also lead to salt precipitation, forcing another possible pressure build-up scenario. Salt precipitate in the pore spaces of the formation, and decreases the permeability of the reservoir considerably (Bachu et al., 1994, Lokhorst and Wildenborg, 2005, Bachu, 2000, Crossley, 1998, Muller et al., 2009). In addition, salt may precipitate as a result of dry CO_2 (<50 parts per million water content) flushing and drying the rock formation. This is e.g. assumed to have occurred at the Snøhvit injection site, as outlined by Hansen et al. (2013). However, this precipitation decreased when the CO_2-injection stopped or the water-content of the CO_2 was changed.

1.4.2.6.3 CO_2-Reactions with Carbonates

CO_2 dissolves within the formation water and creates carbonic acid, as outlined in section 1.4.2.3. This carbonic acid will in turn alter the pH of the formation, by making the formation fluid more acidic. This is a result of an increase in hydrons (H^+) in the fluid, and the relation between pH and hydrons is displayed in Equation 1-4 below.

$$pH = -\log_{10}(H^+)$$

Equation 1-4: Relation between pH and the amount of hydrons (H+) in a solution. An increase in hydrons will decrease the pH-value, making the solution more acidic.

It is commonly known that acidic solutions dissolve carbonate rocks ($CaCO_3$). This lower pH of the formation fluid may in turn lead to dissolution of the carbonate rocks (Koeijer et al., 2013, Izgec et al., 2006). However, carbonate rocks are less prone to dissolution as the reservoir temperature increases (retrograde solubility) (Selley and Sonnenberg, 1998, Koeijer et al., 2013). This is the opposite case of CO_2 dissolved in water (see section 1.4.2.3).

In addition, chemical reactions may occur between the CO_2, $CaCO_3$ and the formation water Equation 1-5. The reactions form calcium bicarbonate ($Ca(HCO_3)_2$), which may precipitate within the reservoir, if the formation fluid becomes oversaturated. In resemblance to salt precipitation in section 1.4.2.6.2, precipitation may cause pressure build-up scenarios

within the reservoir. In general, precipitation of calcium bicarbonate tends to increase with an increase in pH and temperature of the formation (Izgec et al., 2006).

$$H_2O + CO_2 + CaCO_3 \leftrightarrow Ca(HCO_3)_2 \leftrightarrow Ca^{2+} + 2HCO_3^-$$
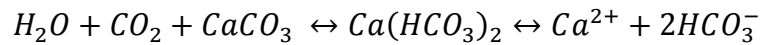
Equation 1-5: Water (H2O) reacts with CO2 and carbonate rocks (CaCO3) and form calcium bicarbonate Ca(HCO3)2 or calcium- (Ca2+) and bicarbonate-ions (HCO_3^-), depending on temperature, pressure and pH of the formation (Izgec et al., 2006).

In addition to reactions between salt (halite) and formation water, outlined in section 1.4.2.6.2, halite may be influenced directly by the injected CO_2. This may in return affect the carbonate rocks of the formation. Hydrons may be released when CO_2 dissolves in water. These hydrons may react with the halite and form hydrogen chloride (HCl). This acid is known to dissolve carbonate rocks. In addition, the chemical reaction between HCl and $CaCO_3$ releases more CO_2, which may increase the reservoir pressure (Izgec et al., 2006, Koeijer et al., 2013). The general chemical reaction is displayed in Equation 1-6.

$$CaCO_3 + 2HCl \rightarrow CaCl_2 + H_2O + CO_2$$
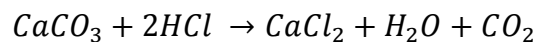
Equation 1-6: Carbonate rocks (CaCO3) react with hydrogen chloride (HCl) and form calcium chloride (CaCl2), water (H2O) and carbon dioxide (CO2). The result may be a pressure-increase within the reservoir. However, this reaction is dependent on halite (NaCl) reacting with hydrons (H+) released from carbonic acid (H2CO3), and is therefore dependent on several factors.

The study area investigated in this thesis is heavily populated with halite deposits (NaCl). A carbonate block ($CaCO_3$) was hit during drilling in 1S (NPD, 2015), and the potential salt-related traps and possible reactions between CO_2, H_2O, NaCl and $CaCO_3$ need to be evaluated in relation to the criteria mentioned above, as they could affect the safety and storage potential of the reservoir. This will be further assessed in section 5.2.3.

1.4.2.7 Leakage of CO_2

Seepages from a CO_2-storage reservoir may occur. It is almost impossible to keep a CCS-reservoir completely tight throughout the whole storage period, hundreds to thousands of years, but it is important to keep the damage to the environment to an absolute minimum (Koeijer et al., 2013). Seepages of CO_2 may occur along fault zones, abandoned wells and single faults, and may contaminate shallower water zones (drinking water), if not detected (Halland et al., 2013).

In addition to leakages of CO_2 from the rocks in the subsurface, the entire water column acts as a potential CO_2-storage. Salinity and temperature are closely related to the ability of the ocean to absorb CO_2, and the ocean is assumed to have stored up to 50% of the anthropogenic

emissions ever released (Maier-Reimer and Hasselmann, 1987). A small seepage from a CO_2-reservoir is therefore unlikely to reach the atmosphere, as the CO_2 is expected to be absorbed by the water column. However, an increase in the mean, global temperature is linked to a higher rate of vaporization from the oceans (Marshall and Plumb, 2008). The increased vaporization will also increase the amount of CO_2 vented to the atmosphere, both as a result of a reduced water column and as a consequence of an increase in salinity (Büenz et al., 2014).

1.4.2.8 Risking and Storage Capacity Calculations

Risking is important in evaluation of a potential storage facility. Risking includes assessing and describing the properties and trapping mechanisms of the CO_2-reservoir, cap rock properties and possible leakage-scenarios. A high risk is often related to a low score in the evaluation. Some of the factors, used in risking, is displayed in Table 1-1, after Halland et al. (2013). Examples of high and low scores are included.

A

CHECKLIST FOR SEALING PROPERTIES			NPD
Typical high and low scores			
Sealing Properties	High	Low	Unacceptable values
Sealing layer	More than one seal	One seal	No known sealing layer over parts of the reservoir
Properties of seal	Proven pressure barrier/ > 100 m thickness	< 50 m thickness	
Composition of seal	High clay content, homogeneous	Silty, or silt layers	
Faults	No faulting of the seal	Big throw through seal	Tectonically active faults
Other breaks through seal	No fracture	sand injections, slumps	Active chimneys with gas leakage
Wells (exploration/ production)	No drilling through seal	High number of wells	

B

CHECKLIST FOR RESERVOIR PROPERTIES		NPD
Typical high and low scores		
Reservoir Properties	High	Low
Aquifer Structuring	Mapped or possible closures	Tilted, few /uncertain closures
Traps	Defined sealed structures	Poor definition of traps
Pore pressure	Hydrostatic or lower	Overpressure
Depth	800- 2500 m	< 800 m or > 2500 m
Reservoir	Homogeneous	Heterogeneous
Net thickness	> 50 m	< 15 m
Average porosity in net reservoir	> 25 %	< 15 %
Permeability	> 500 mD	< 10 mD

Table 1-1: Different risks often evaluated in a CCS-project. A high risk is here related to a low score. A) Risks related to the sealing capability could be e.g. drilled nearby wells, faults or fractures and thickness of the seal. B) Risks related to reservoir storage could e.g. be closure of trap, pore pressure, porosity, permeability etc. After Halland et al. (2013).

In addition to risking of a geological area, the storage capacity of the reservoir is also important to include. The storage capacity indicates how much CO_2 (in kg) which may be injected into the reservoir (Figure 1-10) (Halland et al., 2013). The parameters used in the calculation is further outlined in section 1.4.2.2.

$$M_{CO_2} = Vb \times \varnothing \times n/g \times \rho_{CO_2} \times S_{eff}$$

- M_{CO_2} mass of CO_2
- Vb bulk volume
- $\varnothing$ porosity
- n/g net to gross ratio
- ρ_{CO_2} density of CO_2 at reservoir conditions
- S_{eff} storage efficiency factor

(Geocapasity 2009)

Figure 1-10: Estimate of total amount (kg) of injectable CO_2 into a formation. The calculation depends on volume of the formation (Vb), porosity (Ø), N/G, the density of CO_2 at reservoir conditions (ρ) and the storage efficiency factor (S_{eff}). After Halland et al. (2013).

2 Study Area

The study area investigated in this thesis is located within The Nordkapp Basin, Southwestern Barents Sea. The interpreted 3D-seismic dataset, ST9403, is correlated with the well 7228/7-1A.

7228/7-1 consists of several drilled tracks, but the track 7228/7-1A will be investigated in particular detail for this thesis. For simplicity, this well track will sometimes be referred to as "1A". The remaining well tracks of 7228/7-1 include 7228/7-1S and 7228/7-1B, but these tracks are lacking well log information in parts of the investigated interval of Middle Triassic-Middle Jurassic age. Data from 7228/7-1S will be included if information is missing from 1A and will sometimes be referred to as "1S", in resemblance to "1A". 1S is considered, in favour of 1B, as it contains more information within the investigated reservoir interval.

The sediment deposits found in 1A, with a short geological description and development history is outlined below.

2.1 Geological Setting of the Barents Sea

The Barents Sea is located between the Norwegian mainland and Svalbard and covers 1,3Mkm^2. The general circulation trend of the waters of the Barents Sea is counterclockwise, which bring warm waters from the Atlantic current northeastwards and cold water from the Bjørnøy Stream southwestwards. This circulation keeps the southern parts of the Barents Sea free of ice during wintertime and makes it suitable for storage of CO_2. The Barents Sea is considered a part of the Arctic Ocean, and is connected to the Norwegian Sea to the west, the Greenland Sea to the northwest and the Kara Sea to the east. It is an intracratonic basin, meaning it is a basin located in between stable continental crustal masses (Nichols, 2009, Halland et al., 2013).

A number of tectonic events has influenced the Barents Sea since the end of the Caledonian orogeny, which ended in Late Silurian/Early Devonian. The orogeny was a mountain building era influencing Scandinavia, eastern Greenland, Svalbard and the British Isles, and was caused by collisions of the continents of Baltica, Laurentia and Avalonia (McKerrow et al., 2000). The western and the eastern parts of the southern Barents Sea developed differently after the end of the Caledonian orogeny, and The Ringvassøy-Loppa- and

The Bjørnøyrenna Fault Complexes, marks the boundary of these parts. These fault complexes are dominantly trending in an N-S to NNE-SSW direction, dividing the southern Barents Sea.

The southeastern part of the Barents Sea is dominated by E-W, ENE-SSW and WNW-ESE faults, with thick Upper Paleozoic and Mesozoic sequences. A significant unconformity at the base of the Cretaceous sediments is also found in this region and magmatic sill-intrusions of Jurassic age are also located here. The southwestern part, on the other hand, is dominated by extensive Tertiary, Cretaceous and Paleozoic sediments with NNE-SSW and NE-SW dominating faults, with elements of local N-S faults. This area was particularly active throughout the Late Mesozoic and Cenozoic times, resulting in thick deposits of sediments in the Harstad-, Bjørnøya- and Tromsø basins (Henriksen et al., 2011b, Halland et al., 2013).

The Hammerfest Basin, The Nordkapp Basin, The Loppa High, and The Finnmark- and Bjarmeland Platforms are considered the most important structures of the Southern Barents Sea. However, smaller structures like The Norsel High, Veslemøy High and The Polheim Sub-platform are also present in the area. The main structures are partly defined by complex fault zones, such as the Ringvassøy-Loppa-, Måsøy-, Nysleppen-, Asterias- and Troms-Finnmark fault complexes (Halland et al., 2013). Some of these fault complexes and the main geological structures within the Southern Barents Sea are displayed in Figure 2-1A and Figure 2-1B. ST9403 is also highlighted in the figure (yellow rectangle), together with the chronostratigraphy and different facies of The Nordkapp Basin (Figure 2-1C).
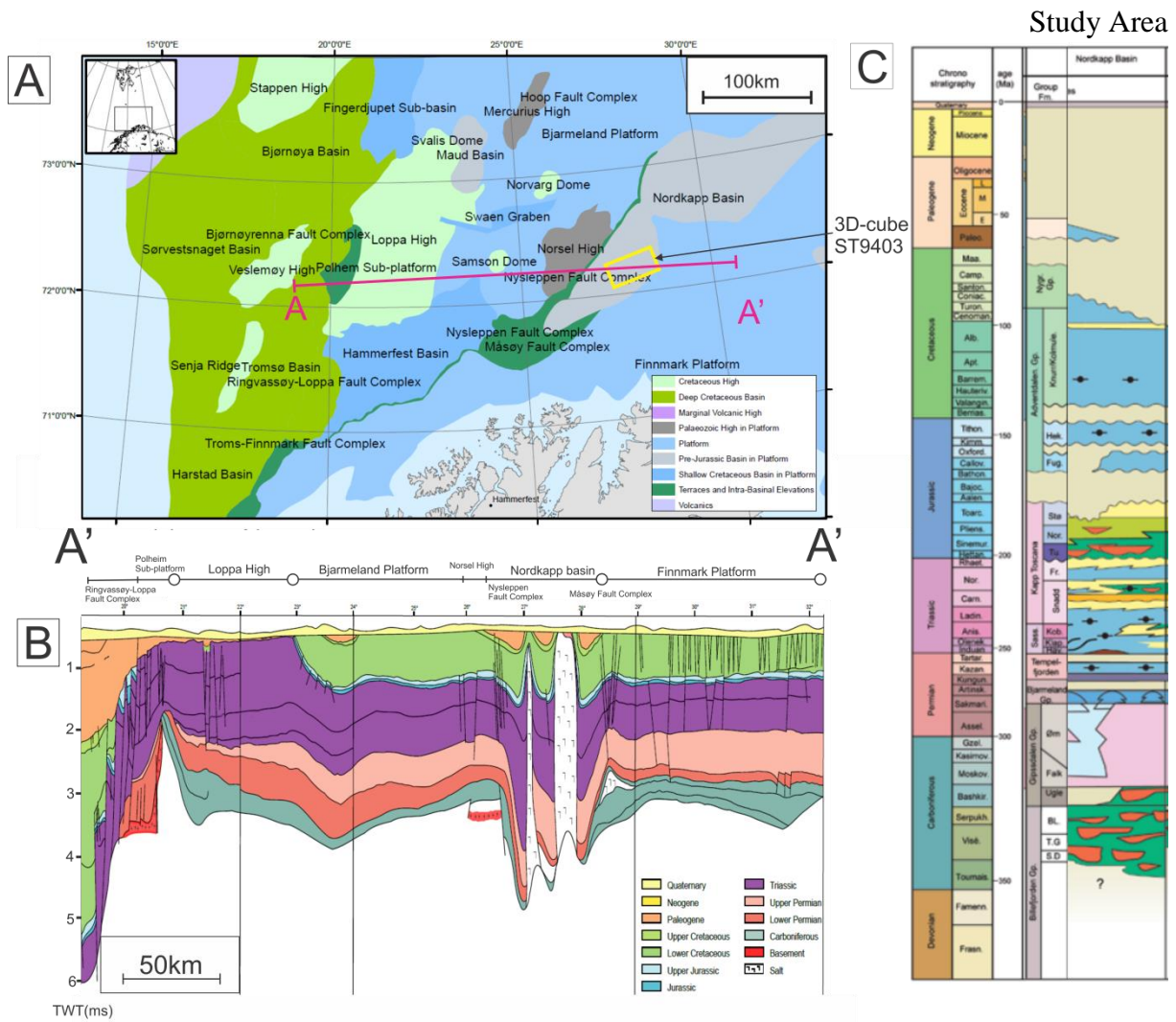
Figure 2-1: A) The Southern Barents Sea and its main structural elements. The 3D-cube is marked as a yellow rectangle. B) A section (A-A') from The Southern Barents Sea. The main basins, platforms and fault complexes are displayed. C) An overview of the chronostratigraphy and different facies for The Nordkapp Basin. Modified after Halland et al. (2013) and Henriksen et al. (2011b).

The Barents Sea region is majorly affected by tectonism, uplift and erosion. The main uplift episodes occurred in Early Tertiary, while the subsequent erosional periods took place in Late Tertiary. The uplift is related to large-scale tectonism, linked to the opening of The Atlantic and The Arctic Oceans. A later phase of uplift and erosion is assumed linked to sediment unloading (isostasy) and glacial periods (e.g. the Quaternary glaciation), and has been extensive. The net uplift is at its largest in the northwestern part of the Southern Barents Sea, towards Stappen High and Bjørnøya, where calculations have implied uplifts up to 3000m (Figure 2-2). This uplift decreases towards the east and south, resulting in a tilting of the

formations. The formations are therefore dipping towards the southeast (Henriksen et al., 2011a, Halland et al., 2013).
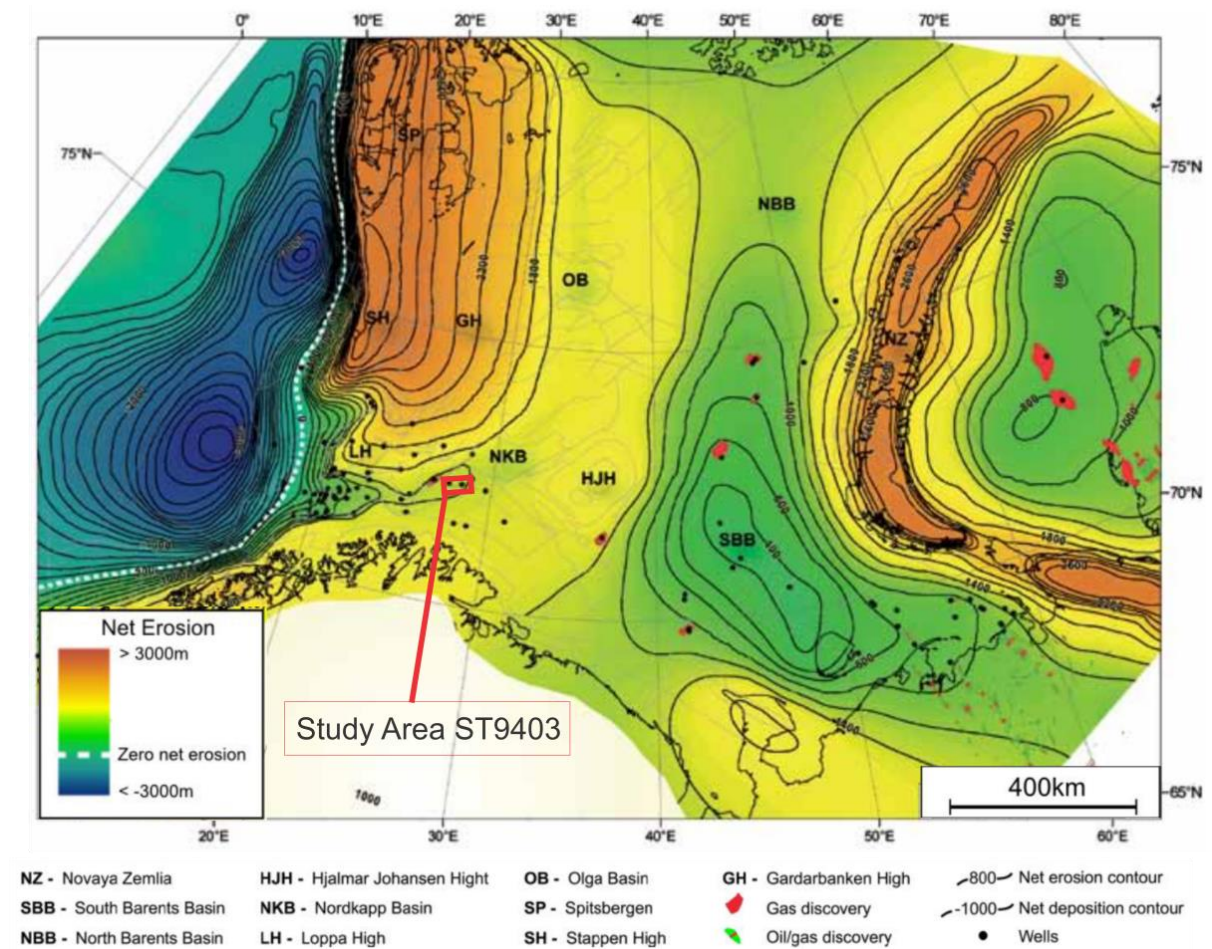

Figure 2-2: A regional map showing the differences in net erosion of The greater Barents Sea. The total net erosion varies from 0-3000m. ST9403 is highlighted by a red rectangle. The study area is located within the yellow-green category of net erosion. Modified after Henriksen et al. (2011a).

The stages of uplift and erosion have affected the properties of the deposited rocks within the Barents Sea. The removal of overburden has led to e.g. leakage of hydrocarbons in several places. It has also resulted in a generally lower reservoir quality, as the rocks have been buried deeper than present-day depths. In addition, the sealing properties are considered lower than at the rest of the Norwegian Continental Shelf (NCS). This is mainly due to evidence of HC-seepage and uplift (Henriksen et al., 2011b, Halland et al., 2013, Henriksen et al., 2011a).

2.2 The Nordkapp Basin

The Nordkapp Basin is located along a SW-NE trending rift and is therefore partially fault-controlled. The basin is bound by The Nysleppen Fault Complex to the northwest, The Måsøy

Fault Complex to the southeast, and The Bjarmeland – and Finnmark Platform the northwest and southeast, respectively (Figure 2.1A). The basin has extensive deposits of Upper Paleozoic sediments, with thick evaporite accumulations from The Gipsdalen Group (Halland et al., 2013, Larssen et al., 2002). These deposits have resulted in extensive salt diapirism since the Early Triassic. The basin has additional, significant sequences of Mesozoic age, where thick Triassic sequences are dominating. A total overview of the sediment accumulations in The Nordkapp Basin is displayed in Figure 2-1C. The mentioned diapirs have been confirmed by exploration wells in the area (Halland et al., 2013, Henriksen et al., 2011b). E.g. the drilled track 7228/7-1S encountered a Permian carbonate block. This Permian block is interpreted to be linked to a nearby salt diapir within the basin (NPD, 2015, Henriksen et al., 2011b). An overview of the salt basin play, linked to the well tracks 7228/7-1S and 7228/7-1A, is displayed in Figure 2-3. The main well of this thesis, 7228/7-1A, is a sidetrack of 1-S and is indicated as the deviated well away from the Permian carbonate.
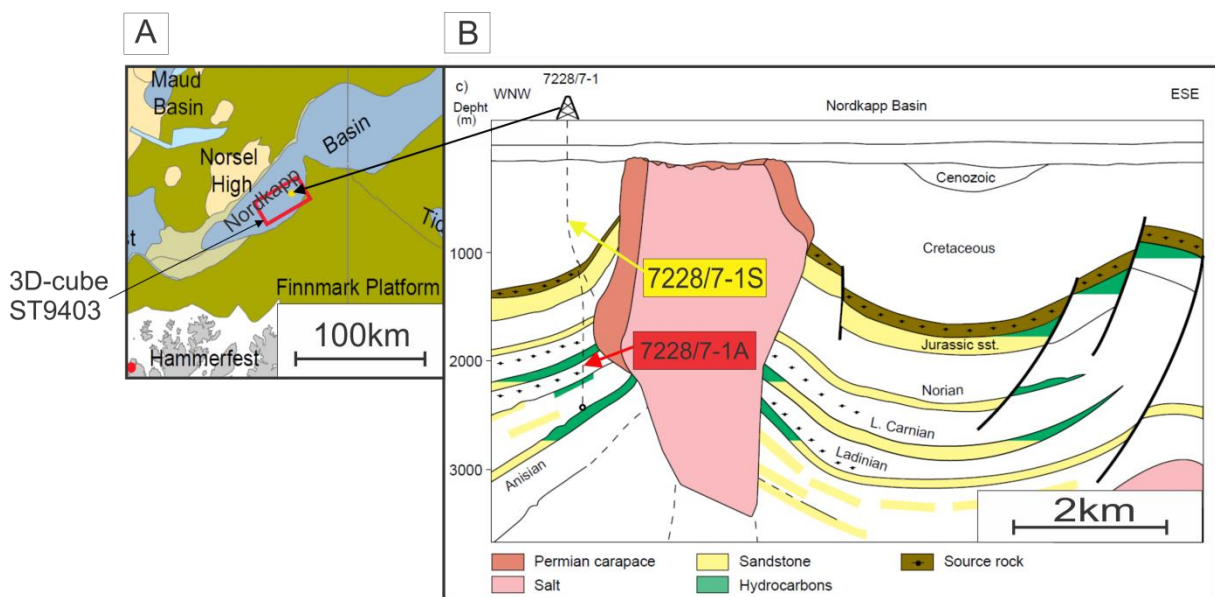

Figure 2-3: A) Location of the 3D-cube with the well 7228/7-1 (yellow circle) within the Nordkapp Basin. B) Sketch of a salt basin play with well tracks 1S and 1A. The main well of this thesis, 7228/7-1A is a sidetrack of 1-S and is displayed as the deviated well away from the Permian carbonate (NPD, 2015). Modified after Henriksen et al. (2011b).

As mentioned in section 2.1, the sediments of The Barent Sea have been uplifted in several stages. Reservoir property measurements have shown uplifts of 500m-1500m from the west to the east of The Nordkapp Basin. The differences in burial depths result in a general, eastward trend of loss in porosity across the basin. Porosity measurements from 7228/7-1S (6-28%), together with reconstructions of maximum burial depth, indicate an uplift of

approximately 1300m for the study area. In general, the reservoir rocks within The Barents Sea appears to have a decrease in porosity of approximately 8% per km (Henriksen et al., 2011a).

2.2.1 The Kapp Toscana Group

The Kapp Toscana Group consists of the Realgrunnen and the Storfjorden subgroups. Kapp Toscana is of Middle Jurassic to Middle Triassic age, and the interval comprises The Snadd Formation (The Storfjorden Subgroup) together with the Fruholmen-, the Tubåen-, the Nordmela- and the Stø formations (The Realgrunnen Subgroup).

The Storfjorden Subgroup (The Snadd Formation) is defined above The Kobbe Formation and below The Fruholmen Formation in Figure 2-1C. Wells have proven thickness variations of the subgroup of 200m-944m throughout The Nordkapp Basin. The bottom of the subgroup is marked by a shale interval and consists of mainly grey sandstones and siltstones. Calcareous layers are relatively common in the lower parts of the unit, with thin, coaly lenses in the upper parts. The lower parts of the subgroup consist of distal, marine deposits which are interpreted to have accumulated after a major transgression. A succeeding extensive progradation then followed the transgression, resulting in deposits with higher sand contents (Halland et al., 2013, Bugge et al., 2002).

The Realgrunnen Subgroup (the Fruholmen-, the Tubåen-, the Nordmela- and the Stø formations) are situated on top of The Storfjorden Subgroup and below The Adventdalen Group (Figure 2-1C). It consists of thick, sandy deposits with particular good quality in its parts of the Stø-, the Nordmela- and the Tubåen Formation. This has been proven from measurements conducted in 7228/7-1S (NPD, 2015).

The extensiveness of the subgroup is variable, with thickness variations within 424-871m throughout The Nordkapp Basin. The dominant lithology within the lower parts of The Fruholmen Formation consists of mainly shale deposits. Here, basal shales, at the base of The Fruholmen Formation, define the lowermost boundary towards The Snadd Formation. Sandy deposits dominate in the middle parts of the formation, while the upper parts consist of shale deposits. Sandy deposits also make up the uppermost- and lowermost part of The Tubåen Formation, with interbedded shale deposits in the middle. The Nordmela Formation have accumulations of interbedded siltstones, mudstones, shale and sandstones, where the sandstone deposits are dominant within the upper parts. The Stø Formation is less dominated by shale than The Nordmela Formation, and is generally considered as a homogenous and mineralogical

mature sand package. In general, The Realgrunnen Subgroup is interpreted to be deposited in a near-shore environment, where the upper parts are deposited closer to shore than the lower parts. The upper parts are generally distinguished by a higher content of coastal- and shallow-marine deposits, while the lower parts have characteristics of more distal compositions (Halland et al., 2013, Bugge et al., 2002).

2.2.2 The Adventdalen Group and the Gipsdalen Group

The Adventdalen Group is situated on top of The Kapp Toscana Group in the well 7228/7-1A, according to NPD (2015). The Adventdalen Group is subdivided into the Fuglen-, The Hekkingen-, The Knurr- and The Kolmule formations. The thickness of the group varies from 300m-1100m throughout The Nordkapp Basin, and is generally dominated by marine, dark mudstones. Local carbonates (limestone and dolomite), siltstone and shelf sandstones are present, and generally The Adventdalen Group is considered a good cap rock. Particularly The Hekkingen Formation and The Fuglen Formation is proven to have appropriate sealing qualities (Halland et al., 2013).

The Gipsdalen Group is also worth mentioning, as thick evaporite deposits (domes of halite) are found within The Nordkapp Basin (NPD, 2015). The depositional environment of these extensive salt diapirs is interpreted to be a result of a warm, arid climate. The halite accumulations on the basinal highs of The Nordkapp Basin are assumed to be deposited in a sabkha environment, while halite accumulations in deeper areas are linked to deposition under water (Larssen et al., 2002).

Study Area

3   Data and Methods

3.1   Seismic Data

The database, used in this thesis, is the migrated 3D-seismic dataset, ST9403. The location of the dataset is within the southwestern parts of The Nordkapp Basin in the Southern Barents Sea (Figure 3-1A). The study area is approximately 44km in Inline-direction and 24km in Xline-direction, and constitutes a total area of $1056km^2$.

The outline of ST9403 is displayed as the pink cube in Figure 3-1A/B. However, the dataset contains areas of noise, and when referring to a location, the blue and red outlines within the pink cube in Figure 3-1B, will be used. The data outside these figures is too noisy to be interpreted. The blue outline will mainly be used for large-scale displays, and the red, inner outline will be used in detailed investigation. Data near salt domes are also poor, and will be outlined further in section 4.2.1. The green arrow points northwards, and will be displayed in all figures to indicate locations.

3.1.1   Well Logs

The focus of this thesis will be on well 1A, with additional information from well 1S, as outlined in the beginning of section 2 (NPD, 2015). 1A and 1S are tracks of the well 7227/7-1, and the location of 7228/7-1 is displayed in Figure 3-1 below.

The available information is used for evaluating a potential CO_2-storage reservoir. The targeted reservoir formations are of Middle Jurassic-Middle Triassic age, where wellbore 1A will function as an injection well for the CO_2. Seismic data has been provided by North Energy ASA and well log data is publically available at NPD (NPD, 2015).
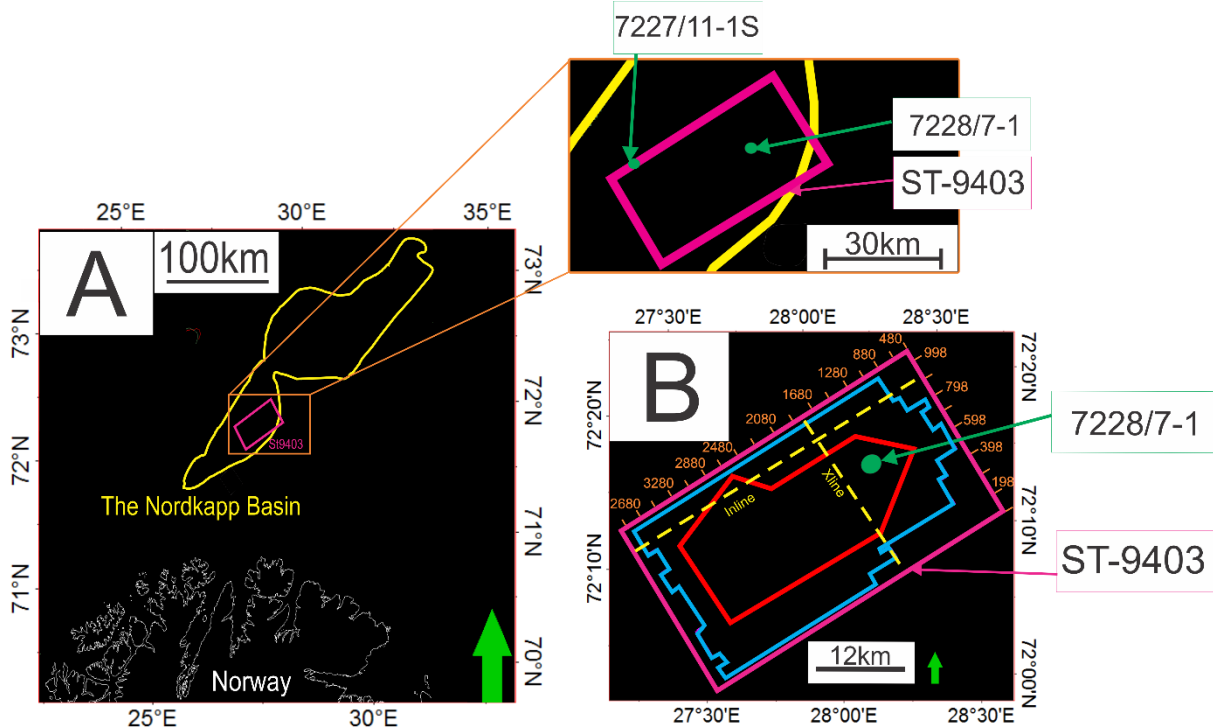
Figure 3-1: A) Location of study area ST9403 (pink rectangle) in The Nordkapp Basin (yellow structure), southern Barents Sea. The study area is penetrated by displayed wells 7227/11-1S and 7228/7-1 (green dots). 7228/7-1A will be the main focus in this thesis and is a well-section of 7228/7-1. B) When referring to a location in the 3D-dataset ST9403, the blue or the red outline, within the pink rectangle, will be used. This is due to poor data. Green arrow points north-wards.

3.2 Velocities

The sonic log from well 1A is lacking measurements <600m measured depth (mMD) below seafloor. A general velocity of 2000ms^{-1} is therefore estimated for <600m within the 3D-cube. The velocity is also implemented for the interval 600-1314mMD. Velocities deeper than 1314mMD is estimated from Figure 3-2, where an average velocity of 2610ms^{-1} is used for 1314-1361mMD and 3718ms^{-1} for 1361-1494mMD.

The velocities are not considered reliable enough to e.g. depth-convert horizons (from ms TWT to m). Present salt domes within the area (NPD, 2015), adds further uncertainty, as the velocities are unknown within the salt domes. Hence, horizons and thicknesses in between horizons are preferably displayed in TWT (ms) throughout this thesis.
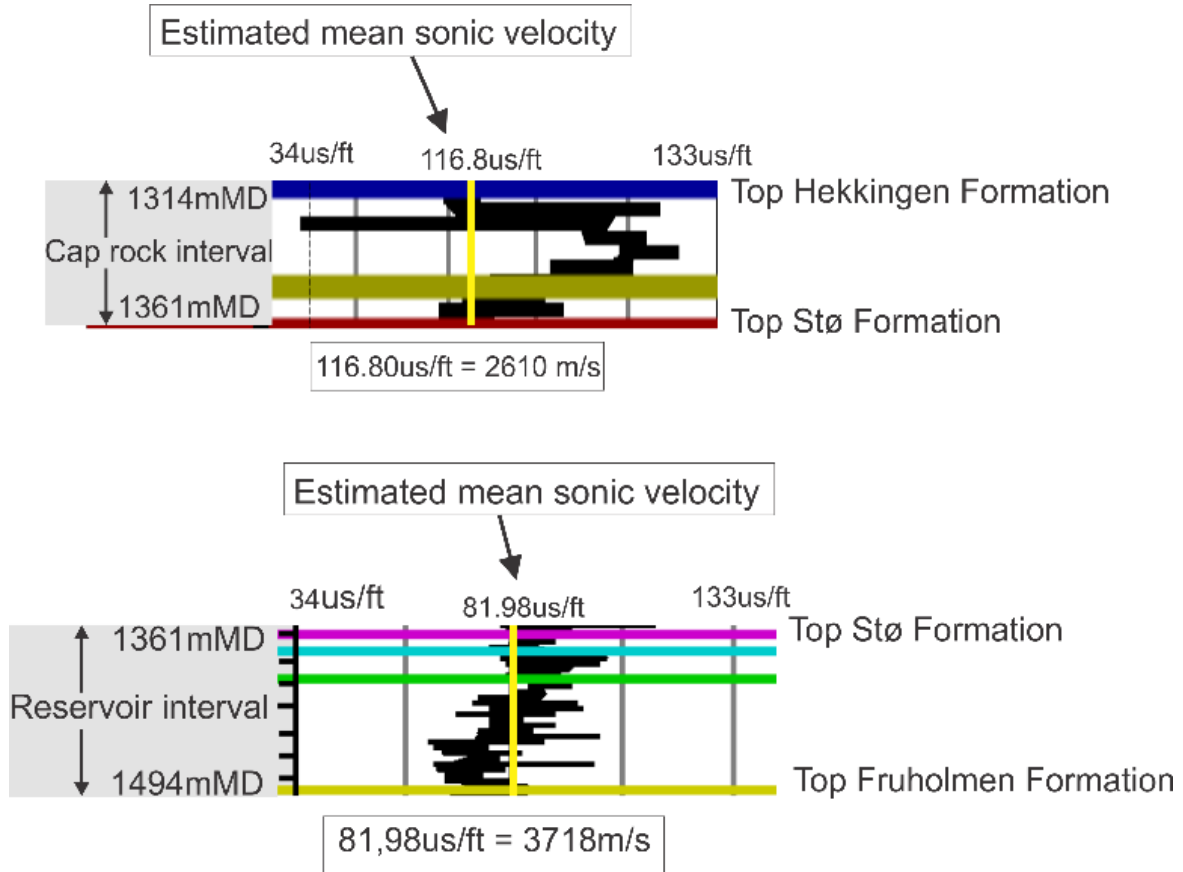
Figure 3-2: Average velocity is estimated to be 2610ms^{-1} for the interval 1314-1361mMD and 3718ms^{-1} for the interval 1361-1494mMD. The velocities are estimated from the sonic log of 1A (NPD, 2015).

3.3 Seismic Data Analysis

3.3.1 Seismic Reflection

A reflective layer in seismic data is produced by a change in acoustic impedance (Z). This change is a result of variations in velocities (V_p) and densities (ρ) of the mediums in the subsurface, while a seismic wave is propagating (Equation 3-1). The contrast produces a reflection coefficient (RC) between 1 and -1 (Equation 3-2), and is usually related to sedimentary bedding planes, pore fill characteristics or unconformities (Andreassen, 2009).

$$Z = \rho \times v$$

Equation 3-1: The acoustic impedance contrast (Z) is a product of density (ρ) and velocity (v) in a medium.

$$RC = \frac{Z2 - Z1}{Z2 + Z1} = \frac{(\rho2 \times v2) - (\rho1 \times v1)}{(\rho2 \times v2 + \rho1 \times v1)}$$

Equation 3-2: The reflection coefficient (RC) quantifies the strength of the change in acoustic impedance above and below an interface. Here, ρ1 and v1 is the density and velocity of the layer above the interface and ρ2 and v2 is the density and velocity of the layer below the interface. This is valid for vertical incidence.

23

3.3.1.1 Seismic Resolution

Seismic resolution is the ability of a seismic survey to detect and separate two interfaces that are located closely together. The resolution is dependent on the frequency (f), the wavelength (λ) and the velocity (v) and this relation is displayed in Equation 3-3.

$$v = \lambda \times f$$

Equation 3-3: Relationship between velocity (v) (ms⁻¹), wavelength (λ) (m) and frequency (f) (s⁻¹).

The equation for the vertical resolution of seismic data is displayed in Equation 3-4. This resolution means that two layers closer than λ/4 (m) will not be recognized as two, separate layers within the subsurface (Rafaelsen, 2005).

$$Vertical\ resolution\ (m) = \frac{\lambda}{4}$$

Equation 3-4: Vertical resolution of seismic data is dependent on the wavelength (λ). A high vertical resolution is a result of a short wavelength.

The horizontal resolution is determined by the Fresnel zone. This zone displays the portion of the energy reflected back from an interface, within a half-cycle after the onset of the reflection. Migrated 3D-seismic surveys decrease the Fresnel zone to about $\frac{1}{4}$ wavelength (Rafaelsen, 2005). The frequency spectrum for the 3D-cube is 5-45Hz, with a dominant frequency of 25Hz (Figure 3-3). The velocities from section 3.2 are 2000-3718ms⁻¹, resulting in a vertical- and horizontal resolution of 20-148m, according to Equation 3-3 and Equation 3-4.
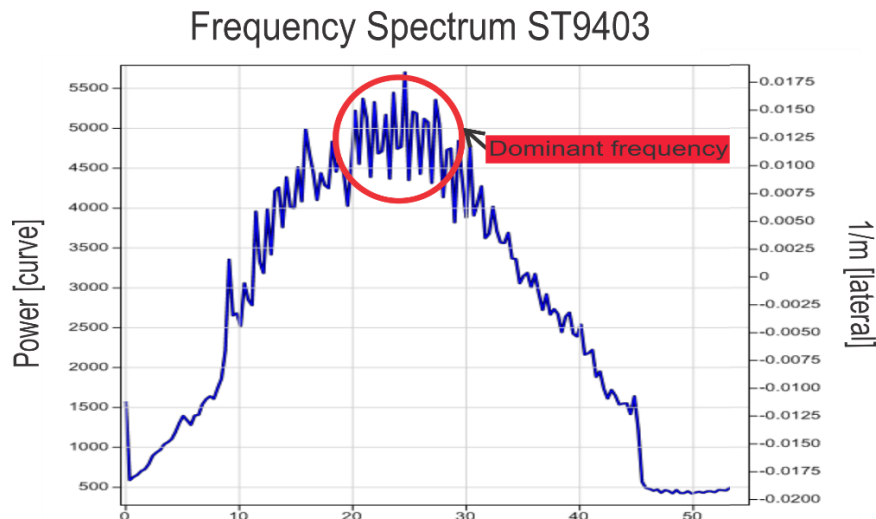

Figure 3-3: The frequency spectrum for the 3D-cube is 5-45Hz. The dominant frequency is approximately 25Hz (red circle).

24

3.3.2   Petrel Software

The results in this thesis are based on Petrel© E&P Software Platform 2013 from Schlumberger. Petrel is a useful interpretation- and visualization tool when correlating and interpreting seismic datasets and well logs.

3.3.2.1   Interpretation

This thesis utilizes manual interpretation, guided autotracking and 2D seeded autotracking as a basis of interpretation, and often several tools are conducted simultaneously. This is due to poor data, mentioned in section 3.1.

Manual interpretation requires the user to follow seismic reflectors throughout the dataset, and is conducted in this thesis if reflectors show discontinuity and are of poor reflection strengths. **Guided autotracking** is conducted by selecting two points on a reflector, and letting Petrel interpret the path of this reflector between the selected points. This tool is used for clear and continuous reflectors. **2D seeded autotracking** is also used on clear and continuous reflectors, and the function only stops if the reflector becomes discontinuous (Schlumberger, 2011). This thesis uses 2D seeded autotracking for the seabed-reflection, as it is prominent and continuous, while deeper reflectors are interpreted with guided autotracking- and/or manual interpretation-tools, depending on the reflection strength. Horizons are created after the interpretation-tools have been utilized.

Seismic peaks, troughs and zero-crossings are interpreted in this thesis, depending on which reflector is of importance to map the dataset.

The wavelets of ST9403 are zero-phased, and the seabed-reflection is a positive zero-phase signal of normal polarity displayed in Figure 3-4. As mentioned in section 3.3.1, a positive reflection coefficient (RC+) is connected to a change in acoustic impedance, where the lower medium of the reflector contains parameters of higher values than the medium above (Andreassen, 2009). This RC creates the displayed positive peak, where the color of the peak is marked by seismic default settings in Petrel. Color settings may vary to a certain extent, but generally default settings will be used throughout this thesis.
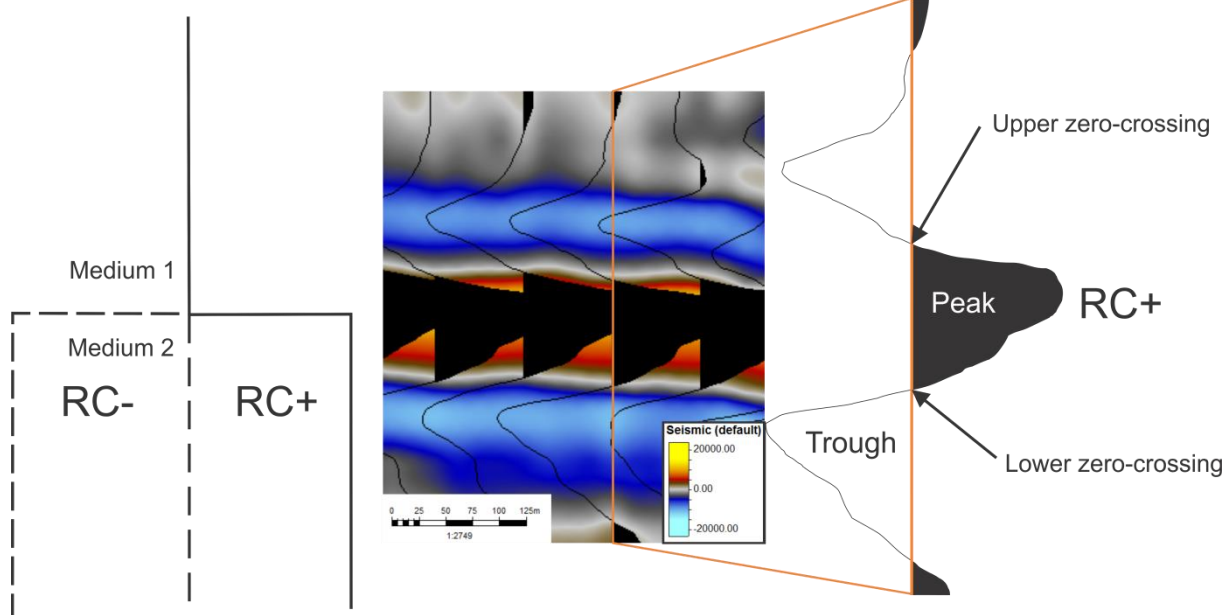
Figure 3-4: A positive reflection coefficient (RC+) is a result of a positive acoustic impedance contrast, as explained in section 1.5.1. The figure displays a positive RC at the seabed-reflection of ST9403, where medium 2 contains parameters of higher value than medium 1. The color chart (right corner) used in this thesis is based on seismic default settings in Petrel, where RC+ is marked by yellow and RC- is displayed in blue.

The Petrel Software displays depths in negative two-way travel time (TWT). For simplicity, when referring to depths in this thesis, a positive TWT is used.

3.3.2.2 *Seismic Attributes*

Seismic attributes is applied in Petrel to visualize and enhance seismic parameters. Some useful attributes applied in this thesis are isochron thickness maps and variance. All information from Schlumberger (2011).

Isochron thickness maps are maps calculated by a time-difference between two horizons. This function is useful when interpreting e.g. reservoir thicknesses.

Variance (Edge method) is useful in edge detection, and applicable as a stratigraphic attribute. Variance may be used for detection of horizontal discontinuities in amplitudes within a window to localize faults, channels etc.

3.3.3 Stratigraphic Correlation

Well tops are available from the well 1A. The well tops were originally in depth, and was converted to time by using check-shot data. The time-converted well is then correlated with the seismic data of the 3D-cube.

3.4   Storage Capacity and Risking

The seismic data is used to indicate volumes, thicknesses and suitable trapping mechanisms within the CO_2-reservoir. Well data from 1A is used to estimate the physical properties of a reservoir (e.g. porosity, N/G etc.) and tightness of a cap rock.

   If information is lacking, or is absent from seismic data or well logs, assumed properties from analogous CCS-projects, The Snøhvit Site and The Sleipner Site, will be implemented. These parameters are listed in Table 3-1 below. The Tubåen Formation, and not The Stø Formation, will be used for comparison at The Snøhvit Site. This choice is based on more articles being available for The Tubåen Formation than The Stø Formation.

   A storage capacity calculation and risk tables, outlined in section 1.4.2.8, will be included in section 5. The calculation is displayed in Figure 1-10 and the risk tables are similar to Table 1-1, after (Halland et al., 2013). The risk table is meant to sum-up the uncertainties and qualities of the CO_2-storage complex, while the storage capacity calculation estimates the amount of injectable CO_2 (in kg) within the reservoir.

Parameters	The Sleipner Field (The Utsira Formation)	The Snøhvit Field (The Tubåen Formation)	Denomination
Location	The North Sea	The Barents Sea	
Reservoir depth	800-1000	2400-2600	m (below seafloor)
Reservoir volume	4.5	12.3	km^3
Porosity (φ)	35-40	10-16	%
Density CO_2 (ρ)	675-715	650-750	kgm^{-3}
N/G	95	80-90	%
Storage efficiency (S_{eff})	5	3	%
Injectable CO_2	$(20\text{-}60)\times10^6$	40×10^6	tonnes (t)
Water content in gas	>550	<550	ppm

Table 3-1: Reservoir parameters from The Sleipner Field in The Utsira Formation and The Snøhvit Field in The Tubåen Formation. The parameters listed in this table will be used to estimate some of the parameters for the CO_2-storage complex. The number (40Mt) of The Tubåen Formation (Osdal et al., 2014), and the higher number (20-60Mton) in The Utsira Formation (Lindeberg et al., 2009) are based in the predicted amount of expected injectable CO_2. The numbers in the table are based on published work after Osdal et al. (2013), Osdal et al. (2014), Hansen et al. (2013), Grude et al. (2013), Maldal and Tappel (2004), Hansen et al. (2013), Halland et al. (2013), Chadwick et al. (2004), Lindeberg et al. (2009), Estublier and Lackner (2009), Wischnewsk (n.d.) and Hansen et al. (2011).

4   Results

The following results are displayed to estimate thicknesses, extent and features of geological formations within the 3D-cube.

4.1   Stratigraphic Correlation

A stratigraphic correlation is used to locate the seismic reflections of the different formations within the 3D-cube. This correlation procedure is described in section 3.3.3. The seismic reflections, within 1A, are displayed within the column "ST9403 ZeroPhase" in Figure 4-1, with well tops. The well tops (coloured lines) imply formation depths. The Top Kobbe Formation, at the top of Figure 4-1, is included to mark the bottom of the target interval, and The Nordland Group and The Adventdalen Group display the overburden.

Seismic reflections from The Kapp Toscana Group (yellow rectangle) are enlarged at the bottom, as these reflections include the Stø-Snadd formations, the target interval of this thesis.

It is observable at the bottom of Figure 4-1 that the seismic reflections are zero-crossings, positive- and negative reflections. The Top Fuglen Formation and The Top Nordmela Formation are zero-crossings, while The Top Hekkingen Formation and The Top Tuåben Formation corresponds with positive reflections. The Top Stø Formation, The Top Fruholmen Formation and The Top Snadd Formation display negative reflections.

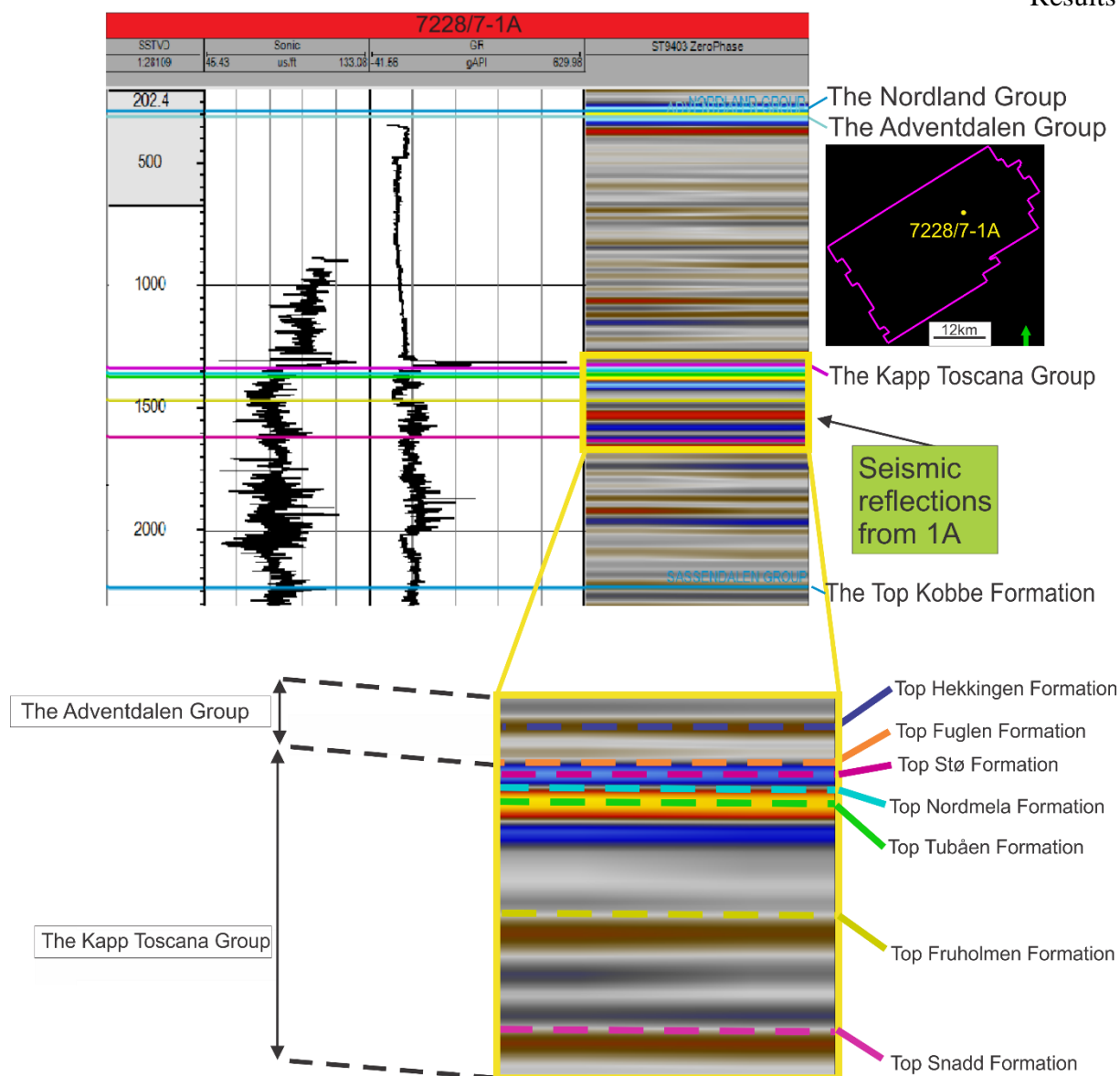Location of well 1A is indicated on the map (black square).

Figure 4-1: Depths, gamma-ray response, sonic log and seismic reflections of 1A from ST9403. The seismic reflections include The Nordland Group, The Adventdalen Group, The Kapp Toscana Group and The Sassendalen Group. Formations of The Kapp Toscana Group are enlarged at the bottom, as the target reservoir interval include the formations of Stø-Snadd. Location of 1A is displayed to the right (black square).

The enlarged reflections, at the bottom of Figure 4-1, are correlated with the reflections of the 3D-cube, as described in section 3.3.3. The procedure is exemplified in Figure 4-2. Interpretation is conducted in the 3D-cube for the reflections of Top Hekkingen (red line), Top Stø (green line), Top Fruholmen (yellow line), Top Snadd (pink line) and Top Kobbe (blue line).
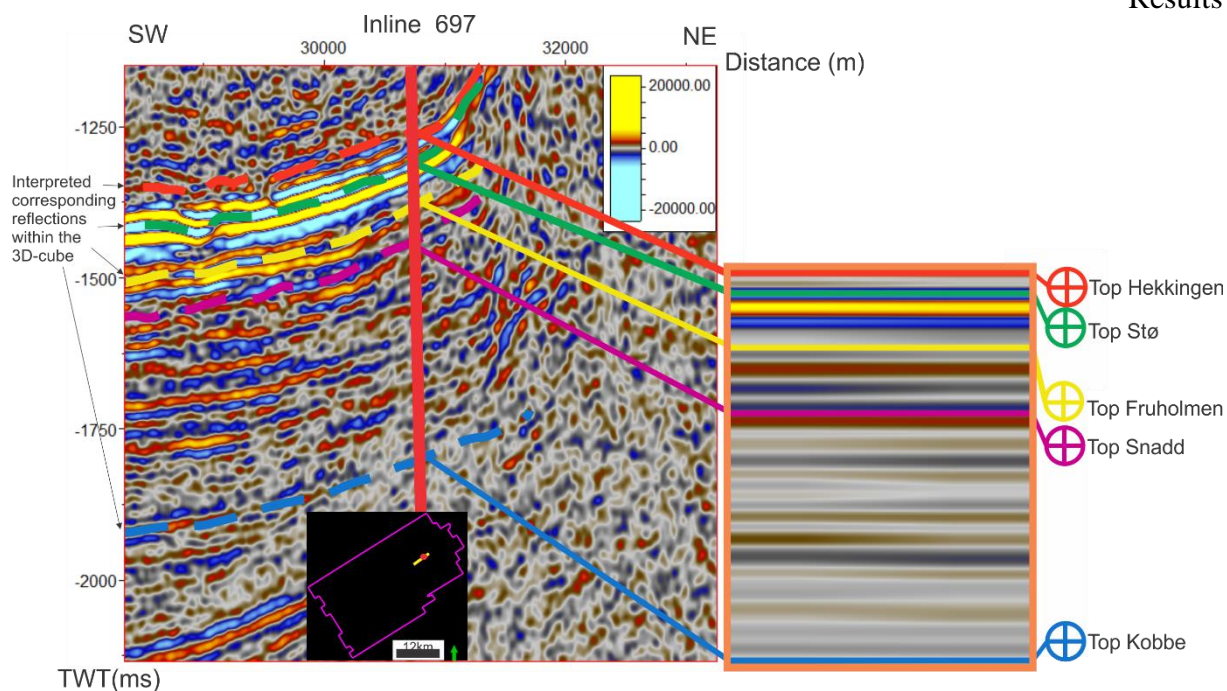
Figure 4-2: Interpretation is conducted in the 3D-cube by recognizing similar seismic reflections from 1A. The well path of 1A is displayed as a red line intersecting Inline 697 (NB! Not to scale!). The correlation procedure is displayed for The Top Hekkingen Formation (red line), The Top Stø Formation (green line), The Top Fruholmen Formation (yellow line), The Top Snadd Formation (pink line) and The Top Kobbe Formation (blue line). Location of Inline 697 (yellow line) and well 1A (red dot) is displayed at the bottom.

4.2 Horizons and Stratigraphy

4.2.1 Interpreted Horizons

In total, five seismic horizons are interpreted. The horizons are interpreted to assess general formation thicknesses and properties. This will be addressed more closely in Figure 4-8 and onwards.

The horizons are displayed in Figure 4-3. The horizons are displayed in TWT (ms) and named The Top Hekkingen Reflector, The Top Stø Reflector, The Top Fruholmen Reflector, The Top Snadd Reflector and The Top Kobbe Reflector. The Top Stø Reflector marks the top of the investigated interval, while The Top Kobbe Reflector marks the bottom, as mentioned in the previous section. The Top Hekkingen Reflector is included to mark parts of the overburden.
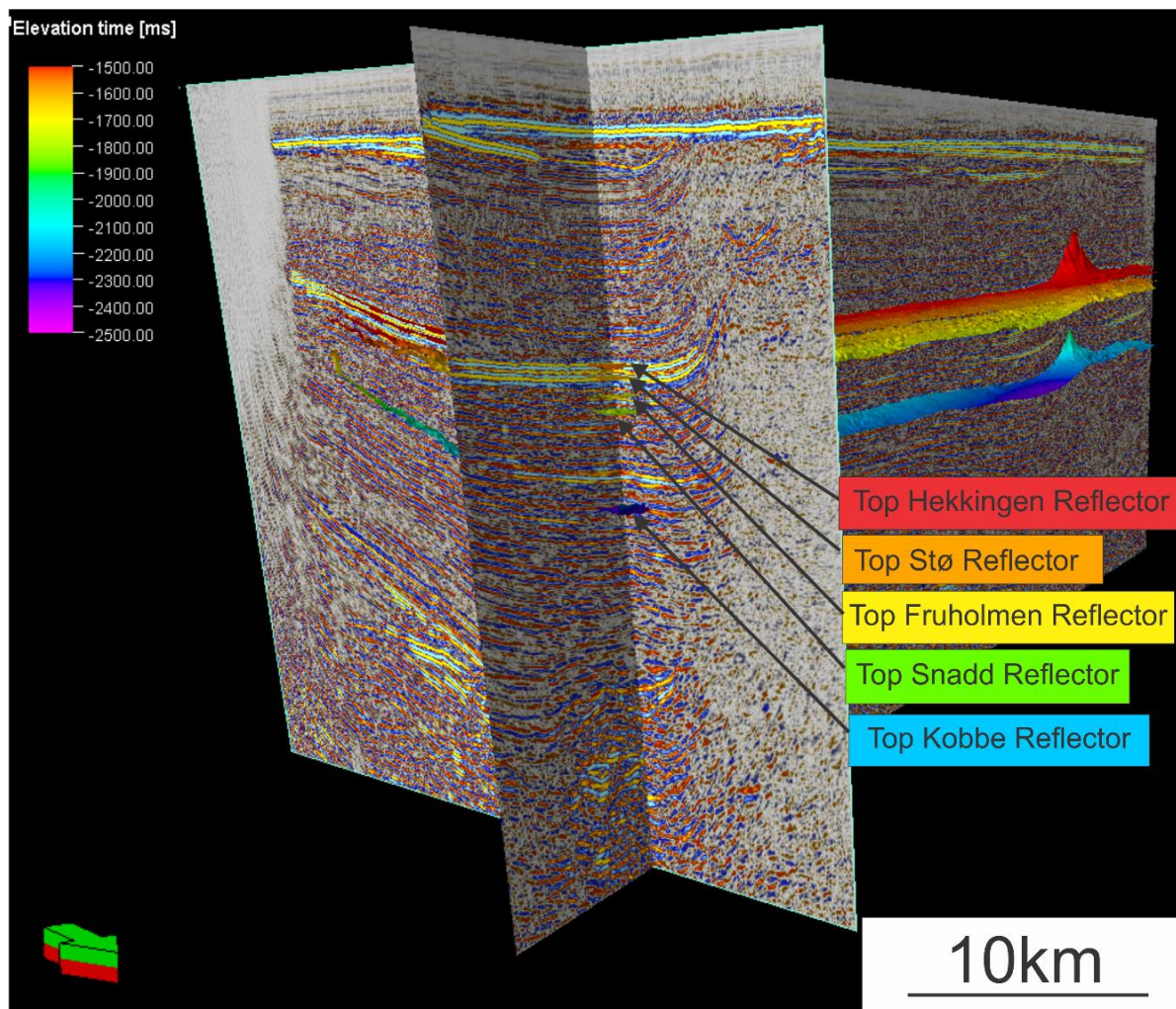
Figure 4-3: Interpreted horizons named The Top Stø Reflector, The Top Fruholmen Reflector and The Top Snadd Reflector are all parts of the possible CO$_2$-reservoir in this thesis. The Top Hekkingen Reflector is included to mark parts of the overburden and The Top Kobbe Reflector marks the bottom of the reservoir interval.

The same horizons are displayed in TWT (ms) in Figure 4-5,

Figure 4-6 and Figure 4-7 below for more detailed inspections. Horizons are preferably displayed in time in this thesis, as outlined in section 3.2.

It is observable from Figure 4-3, and in Figure 4-5 to Figure 4-7, that the interpreted horizons are relatively parallel, with peaks in the same areas from horizon to horizon. The Nordkapp Basin, where the 3D-cube is located, is known for an extensive amount of salt domes, interpreted to cause the peaks in the figures. The salt domes are bending the surrounding strata, indicated by Xline 2276 and Inline 652 in Figure 4-4 (NPD, 2015), and a general thinning of strata towards the salt domes is therefore expected. The salt domes are considered stable enough for hydrocarbon exploration, where well 1S encountered the rightmost salt pillow in Inline 652

(Figure 4-4) (Henriksen et al., 2011b, NPD, 2015). However, the salt pillows are cropping out in close proximity of the seafloor in the figure, indicating recent movement. Most trap types of The Nordkapp Basin are also highly influenced by, and often linked to, these salt domes.

A yellow, dotted line in Figure 4-4 to Figure 4-7, marks the areas on the horizons, in which these salt pillows occur. However, due to poor data near the apex of the salt domes, as mentioned in section 3.1, the encircled area are only infilled by Petrel and not based on actual seismic interpretation. The horizons are only interpreted manually outside the encircled areas. Although, the domes are still included, as a guidance for the reader, to get an idea of a local, structural high.

The general noise level, outlined in section 31, has influenced the interpretation of the horizons in Figure 4-5 to Figure 4-7, as details are lost with increasing depths.
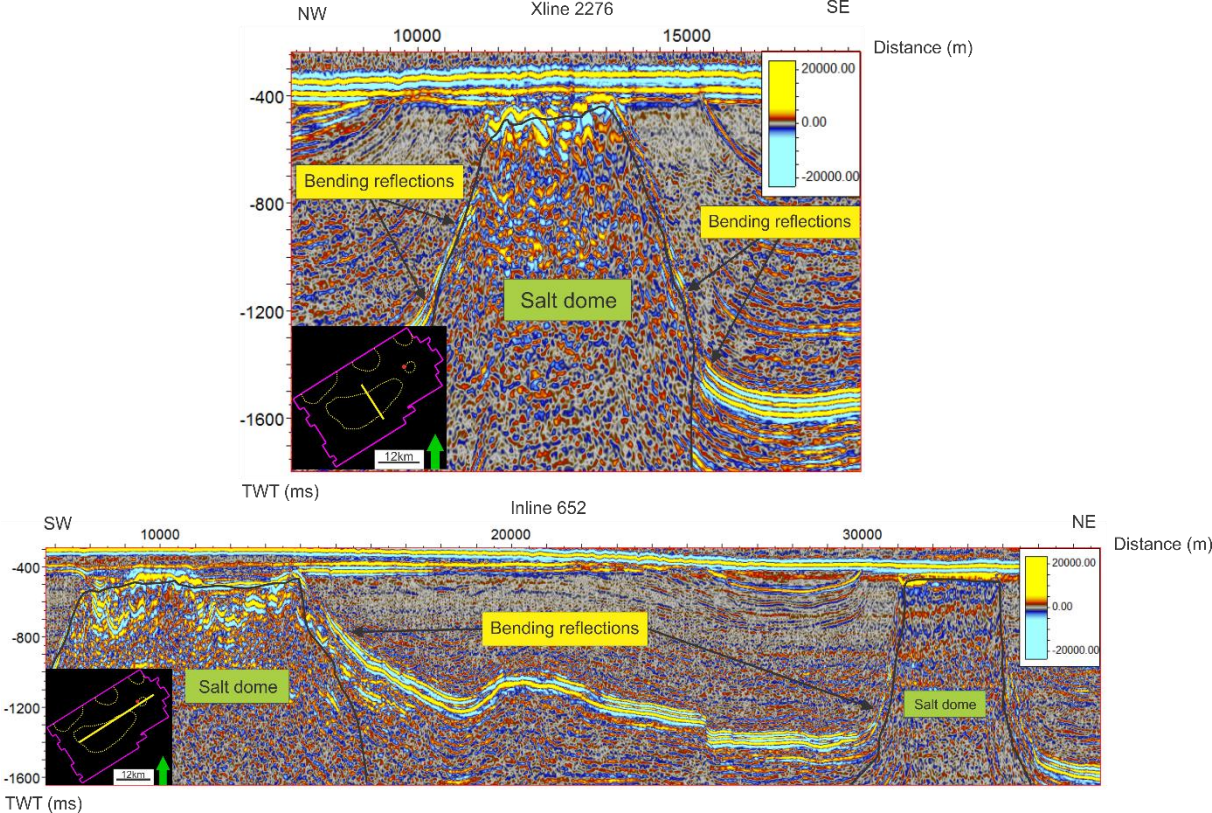

Figure 4-4: Several salt domes are present in the 3D-cube ST9403. The salt dome displayed in Xline 2276, and to the left in Inline 652, is the largest salt dome within the area. The rightmost salt dome in Inline 652 is the salt dome encountered in 1S, located close to the injection well 1A (red circle) (NPD, 2015, Henriksen et al., 2011b). The outer boundaries of the salt domes (black line), in the seismic section, are only to be considered as a relative guidance, and are not mapped in detail. The salt domes are cropping out in close proximity of the seafloor, but are considered stable. Location of Xline 2276 and Inline 652 are marked as a yellow, straight line on the map, where the outer boundaries of the salt domes are marked as a yellow, dotted line.

The Top Hekkingen Reflector
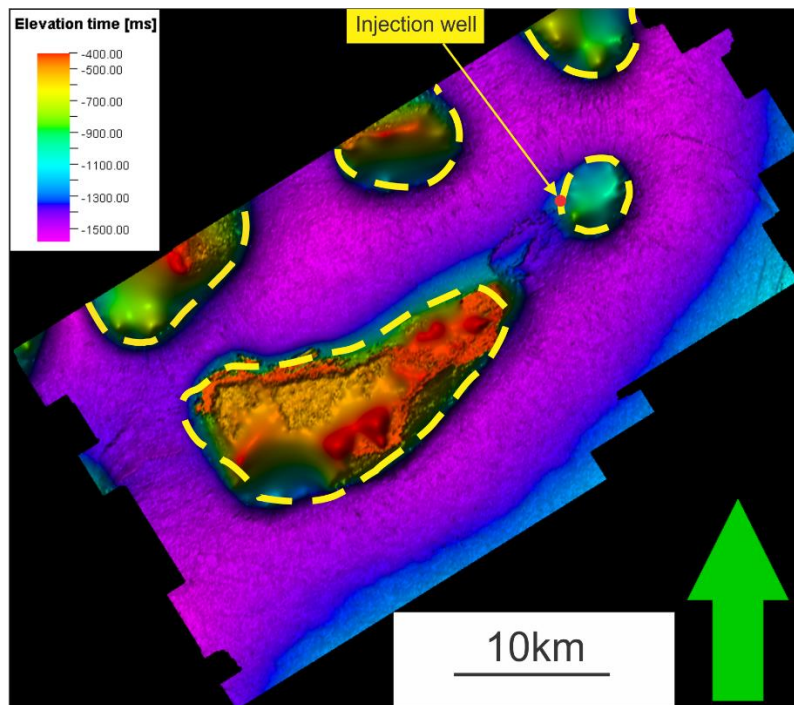
The Top Stø Reflector
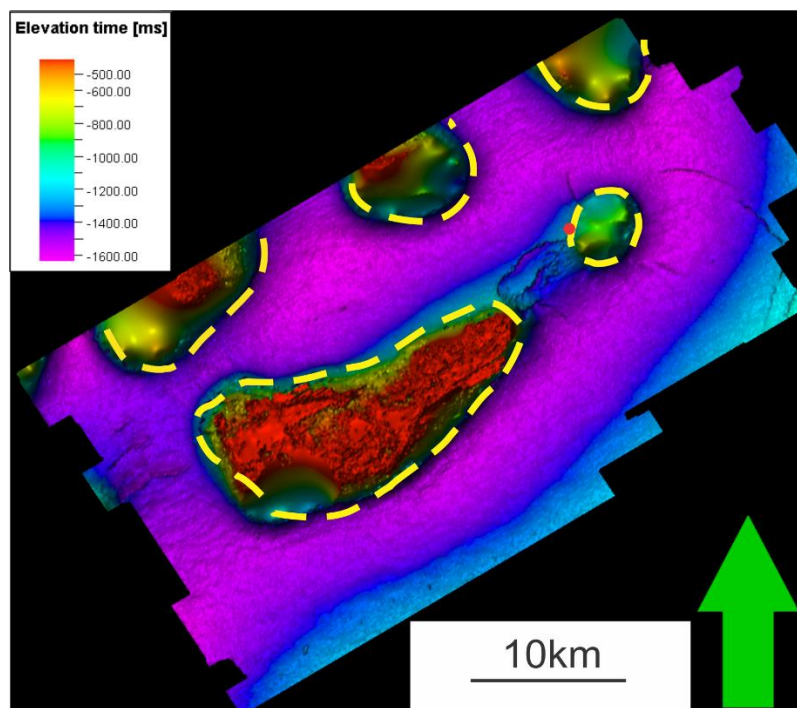
Figure 4-5: The interpreted Top Hekkingen Reflector and The Top Stø Reflector. The interpreted horizons seem to have relatively parallel highs and lows, but areas within the salt domes (yellow, dotted lines) are particularly variable, as they are automatically infilled by Petrel. These peaks are however included for the reader to get an idea of a local, structural high. Horizons are displayed in TWT (ms). Injection well, 1A, is marked as a red circle.

The Top Fruholmen Reflector
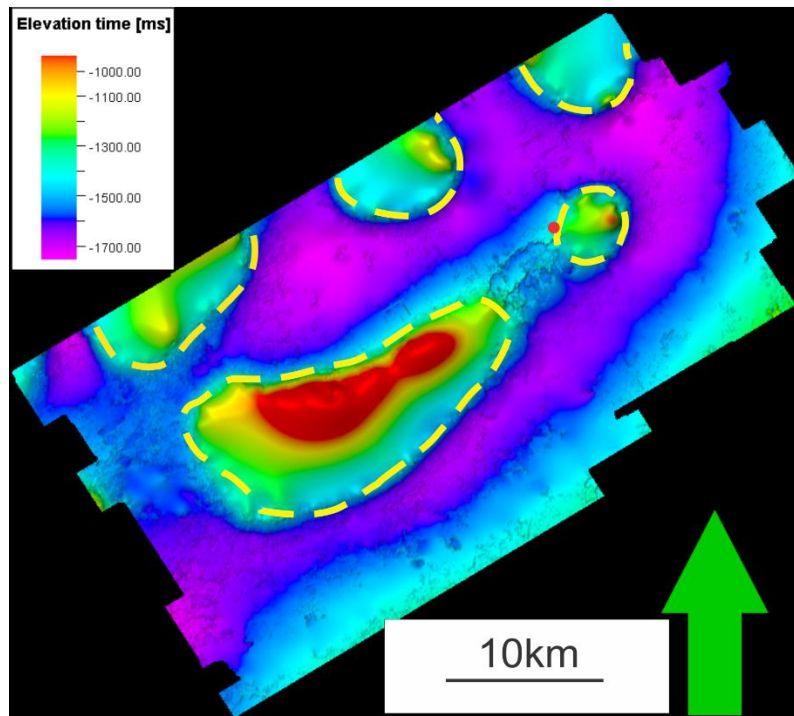
The Top Snadd Reflector

Figure 4-6: The interpreted Top Fruholmen Reflector and The Top Snadd Reflector. The interpreted horizons have depth variations within the same areas. However, the areas within the yellow, dotted lines are variable, as they are automatically infilled by Petrel. These areas are however included for the reader to get an idea of a local, structural high. Horizons are displayed in TWT (ms). Injection well, 1A, is marked as a red circle.

The Top Kobbe Reflector

Figure 4-7: Interpretation of Top Kobbe Relector. The area within the yellow, dotted lines are automatically infilled by Petrel, and are not a part of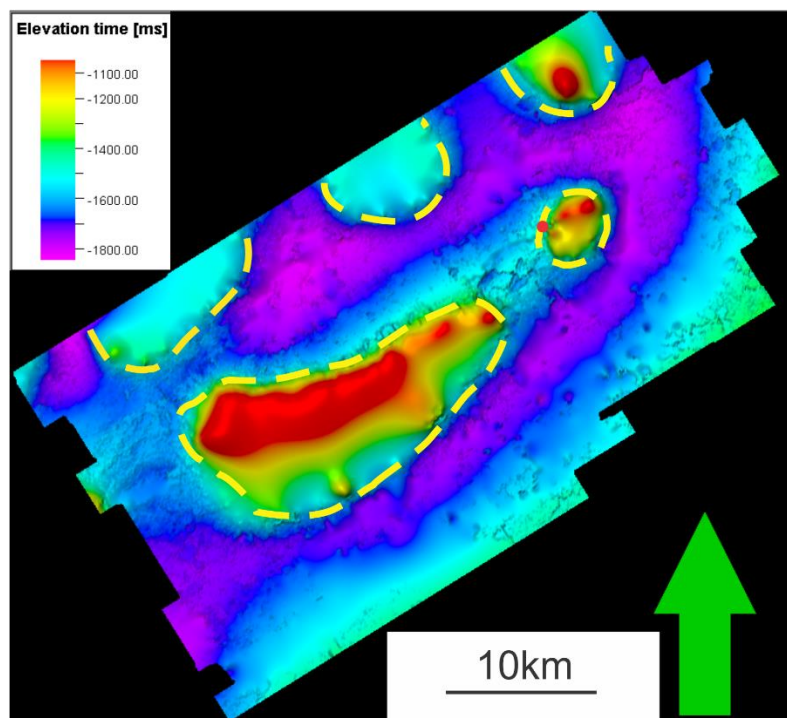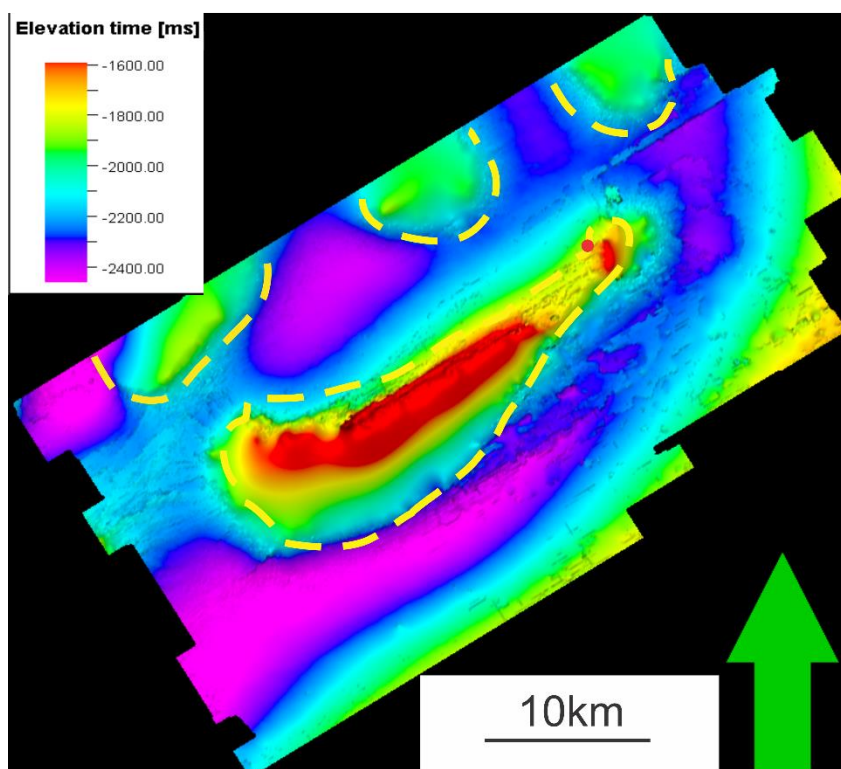 the interpretation. These areas are however included for the reader to get an idea of a local, structural high. Horizons are displayed in TWT (ms). Injection well, 1A, is marked as a red circle.

4.2.2 Stratigraphy

1A encountered several formations when it was drilled in 2001 (NPD, 2015). The Hekkingen Formation and The Fuglen Formation was penetrated at 1314-1361mMD in 1A. This interval is interpreted to be equivalent to the interval between The Top Hekkingen Relfector and The Top Stø Reflector in Figure 4-5. The Hekkingen – and the Fuglen formation is dominated by marine, dark mudstones within The Barents Sea, and The Hekkingen Formation is generally considered a good cap rock, as outlined in section 2.2.2.

The wellbore log from 1A, displayed in Figure 4-9, indicates a particular high gamma log response (GR), from approximately 200gAPI at 1314mMD to >300gAPI below 1340mMD. A significant response is also observable for the bulk density- and the neutron porosity log, in the same interval, where the measurements for density and porosity far exceeds parameters > 2950kgm^{-3} and < -0.15m^{3}m^{-3}. The sonic log varies from approximately 40-160μsft^{-1}. The resistivity log indicates an interval of medium resistivity, approximately 50Ωm. The GR and

the sonic log suggests a tight sediment interval, with a high shale content from 1314-1361mMD. The low neutron porosity log might be caused by gas readings (0.1%) in the well (NPD, 2015). The medium resistivity is expected for a shale interval, as shale is partly conducting (Selley and Sonnenberg, 1998).

The interval between The Top Stø Reflector and The Top Fruholmen Reflector, in Figure 4-5 and

Figure 4-6, is interpreted to consist of The Stø Formation, The Nordmela Formation and The Tubåen Formation. These formations generally consist of clean sandstone-intervals within The Barents Sea, as outlined in section 2.2.2. The formations of Stø-Tubåen were encountered at 1361-1494MD in 1A, below The Fuglen Formation in Figure 4-9. All formations of Stø, Nordmela and Tubåen display excellent reservoir qualities within 1A, as clean sandstone was proven from cores and samples (NPD, 2015).

The GR in Figure 4-9 is relatively low, approximately 170gAPI throughout the interval, except for a section with a GR of approximately 200gAPI at 1420-1440mMD. The density- and neutron porosity log also indicate relatively low measurements, of approximately 2300kgm^{-3} and 0.2m^{3}m^{-3} respectively. These log responses are relatively constant, except for a particularly significant interval, at 1420-1440mMD, where the density increases to approximately 2600kgm^{-3} and the neutron porosity log increase to 0.45m^{3}m^{-3}. The sonic log seems relatively constant throughout The Stø - Tubåen Formation at 82μsft^{-1}. The resistivity log have several intervals where the resistivity increases significantly, but it is generally low throughout, at approximately 20Ωm. However, a particularly high reading occurs at 1420-1440mMD, where the resistivity log increases to approximately 50Ωm.

The homogenous and low gamma-ray response, and the relatively low density-, sonic- and resistivity log, indicate a generally clean sandstone from 1361-1494mMD. The sandstone-interval was proven water-wet from laboratory tests, but had a slight HC-odour, according to NPD (2015). This HC-content may affect the neutron porosity log, where the readings are of 0.2m^{3}m^{-3}. However, the effect on the log here is less than for the interval above, between The Hekkingen Reflector and The Stø Reflector, where the readings reached < -0.15m^{3}m^{-3}, and hence indicate less HC being present within the Stø-Tubåen formation. No exact porosity measurements are available from 1A for the Stø-Tubåen formations, but calculations from 1S estimates 6-28% for the interval (Henriksen et al., 2011a), as mentioned in section 2.2.

The interval at 1420-1440mMD in Figure 4-9 is not mentioned in particular from well reports. It is interpreted to consist of sandstone with a higher shale content than the rest of the Stø-Tubåen interval, with low water-content within the pores. The higher shale content is indicated by a higher GR, higher density and medium resistivity measurements, together with a higher neutron porosity log. The increased neutron porosity suggests a tight rock or a low hydrogen-content within the pores. The first is assumed to be correct, since low HC-reading occur within the interval (NPD, 2015).

The interval below 1494mMD, in Figure 4-9, display well logs from parts of The Fruholmen Formation (NPD, 2015), where the well logs are generally influenced by high readings. An observable very high GR (>250gAPI) and medium resistivity measurements (>50Ωm) indicate a sand-interval with a high shale-content. This is also suggested by a high neutron porosity log (>0.3m^3m^{-3}), indicating a low porosity for the sediment packages below this depth. The interval of 1494-1600mMD is therefore interpreted to consist of interbedded sand and shale.

As mentioned above, Figure 4-9 only display depths down to 1600mMD. This display is chosen for simplicity, as the intervals below The Fruholmen Formation, all the way down to The Kobbe Formation in 1A, display the same well log trends (NPD, 2015), suggesting interbedded shale and sandstone. The interpreted thicknesses below The Top Fruholmen Reflector, all the way down to The Top Kobbe Reflector in

Figure 4-6 and Figure 4-7, are therefore interpreted to consist The Fruholmen Formation and The Snadd Formation, with interbedded shale and sandstone. In other words, The Fruholmen Formation constitute the thickness in between The Top Fruholmen Reflector and The Top Snadd Reflector, and The Snadd Formation make up the thickness in between The Top Snadd Reflector and The Top Kobbe Reflector.

4.2.2.1 *Thicknesses*

The thicknesses of the various formations, outlined above, are displayed in seismic sections in Figure 4-8. The Hekkingen- and The Fuglen Formations are displayed in green (50ms TWT), while the thicknesses of The Stø-Tubåen Formations have a yellow colour (100ms TWT). The thickness of The Fruholmen Formation is coloured in blue (100ms TWT), and the thickness of The Snadd Formation has a pink colour (450ms TWT).

Figure 4-8 shows that some thicknesses are more extensive than others, where e.g. The Snadd Formation is 350ms TWT thicker than the formations of Stø-Tubåen. However, the different intervals seem to have the same thickness-trends in all pictures, where e.g. the formations of Stø-Tubåen are approximately 100ms (TWT) thick in all seismic sections.

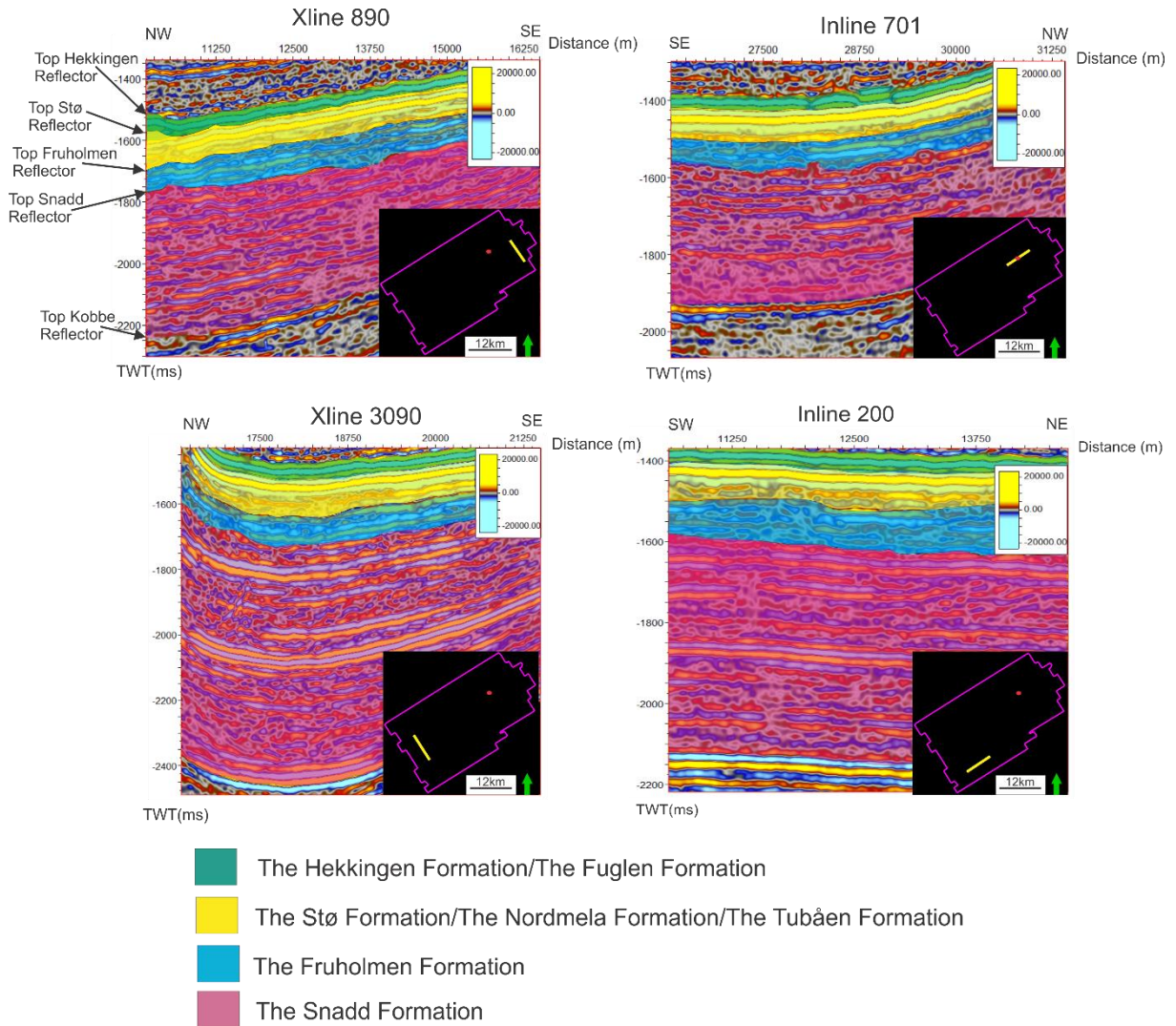**Figure 4-8: The interpreted horizons and the thickness variations in between these horizons are displayed for Xline 890, Inline 701, Xline 3090 and Inline 200 from the 3D-cube ST9403. The interval of Hekkingen-Fuglen is marked in green and Stø-Tubåen has a yellow colour. The Fruholmen Formation is coloured in blue and The Snadd Formation is marked in pink. The interpreted reflectors are also included for convenience.**
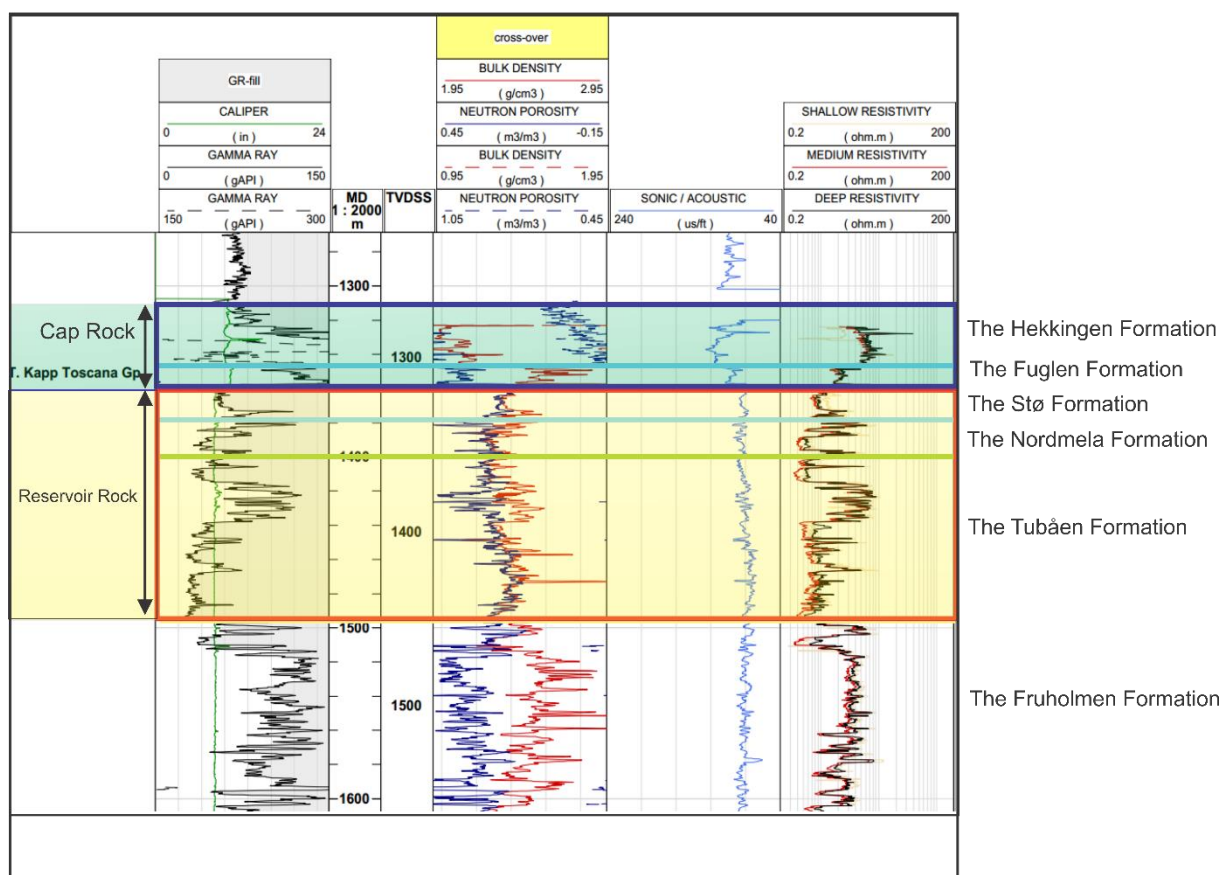
Figure 4-9: Well logs of 1A. The Hekkingen and The Fuglen Formation suggests a tight shale-interval at 1314-1361mMD. A cleaner sandstone is interpreted to occur within The Stø Formation, The Nordmela Formation and The Tubåen Formation at 1361-1494mMD, except for a tighter interval at 1420-1440mMD. Interbedded sandstone and shale occur below The Fruholmen Formation, down to The Kobbe Formation. Modified after NPD (2015).

A lithology log is created for the tightest shale and the cleanest sandstone. These intervals constitute the Hekkingen – and the Fuglen formations (shale) and the Stø-, the Nordmela- and the Tubåen formations (sandstone). The lithology log is displayed in Figure 4-10. The figure is meant to display the same sediment properties as the wellbore log indicates in Figure 4-9, where the interval of Hekkingen-Fuglen is displayed in green. The interval of Stø-Tubåen has a yellow colour, and the tighter sandstone-interval between 1420-1440mMD is indicated in red. Only parts of the interval between The Fruholmen Formation is included in the figure, which generally show an increase in tightness of the sediments (NPD, 2015). A red colour is therefore assumed suitable for The Fruholmen Formation and below in Figure 4-10.

Lithology Interpretation
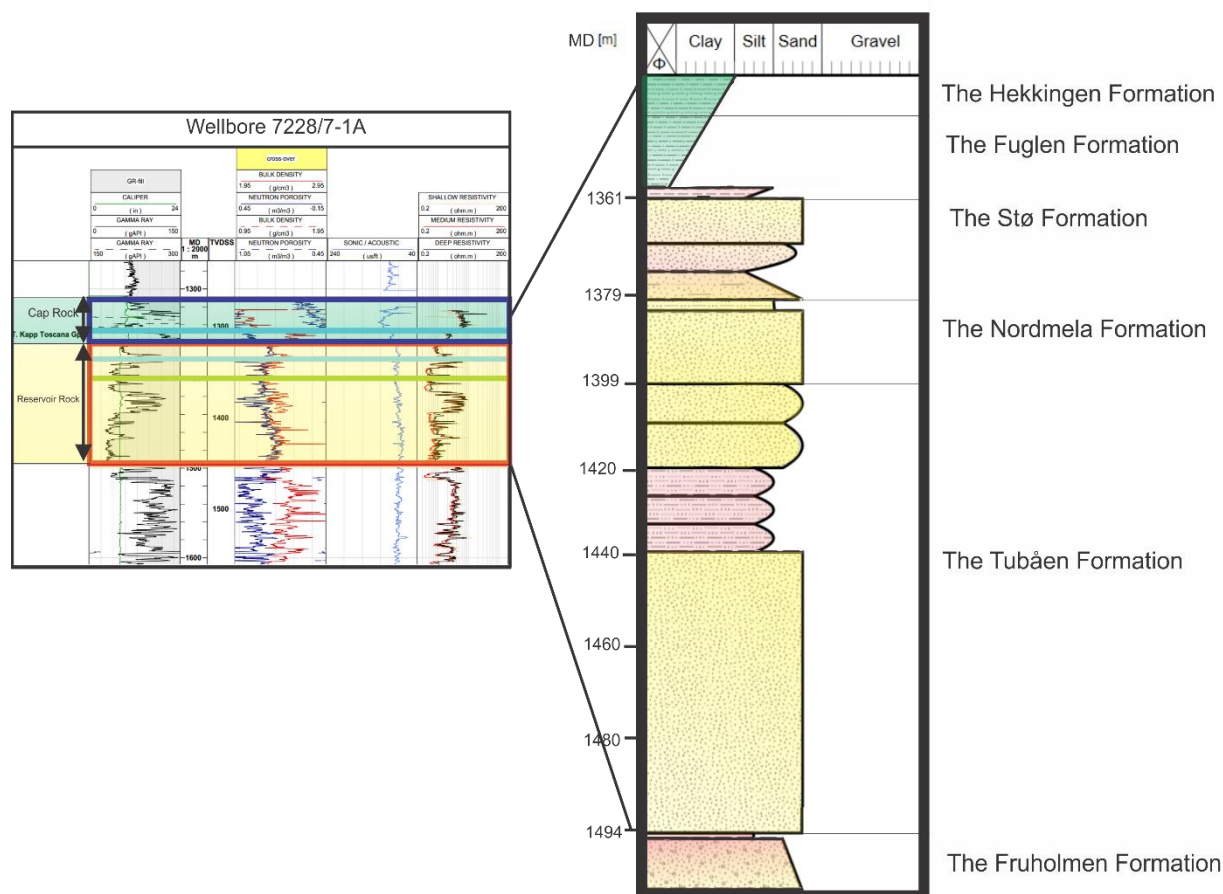
Figure 4-10: Lithology log of the cleanest sand- and shale-intervals. The shale interval (green) consist of the formations of Hekkingen and Fuglen, while the sandstone interval constitute the Stø-Tubåen formations. A tighter interval, within The Tubåen Formation, at 1420-1440mMD, is displayed in red. Upper parts of The Fruholmen Formation, is marked by a red colour. It consists of interbedded shale and sand. Modified after NPD (2015).

4.2.2.1.1 The Stø-Tubåen Formations

The text in the remaining parts of section 4 will focus on the area within the dotted lines in Figure 4-11, Figure 4-13, Figure 4-15 and Figure 4-16. The boundaries of these dotted lines will be discussed in section 5.1.

Some figures, Figure 4-11 and Figure 4-16, are displayed in 3D. This is because the salt domes make the flanks almost vertical near the salt domes, and difficult to see in 2D.

The thickness of Stø-Tubåen is indicated in yellow in seismic sections. These thicknesses are seen in Figure 4-12, Figure 4-14 and Figure 4-17. The red areas in figures mark the Hekkingen-Fuglen interval, while the blue areas indicate the extent of the salt domes.

Figure 4-11 displays an isochron thickness map in TWT (ms) for the Stø-Tubåen interval. The injection well 1A (orange line) is displayed to the north on the map, and the largest salt dome, the salt dome in the middle of e.g. Figure 4-5, is displayed to the south.

Area 3 marks the thinnest interval of Stø-Tubåen in Figure 4-11. It has an elongated shape located in an NS-direction, with a suggested thickness of 25ms TWT in Xline 3032 in Figure 4-12. The size is approximately 500m in width and 3km in length in Figure 4-11, and the location of Xline 3032 is displayed as a red line. A thin interval is expected within Stø-Tubåen, as the sediments are thinning towards the apex of the salt domes, as outlined in section 4.2.1. Two areas are particularly thick, marked as 1 and 2 on the map. These thicknesses are not to be considered as real, as they are results of noisy data near salt domes, as mentioned in section 3.1 and 4.2.1.

The maximum thickness of the Stø-Tubåen interval is assumed 100ms TWT. This thickness is observable near the bottom of the yellow, dotted line, in Figure 4-11 (green-blue colours). This dotted line will be discussed in section 5.1.2.1.

Isochron Thickness Map TWT(ms)
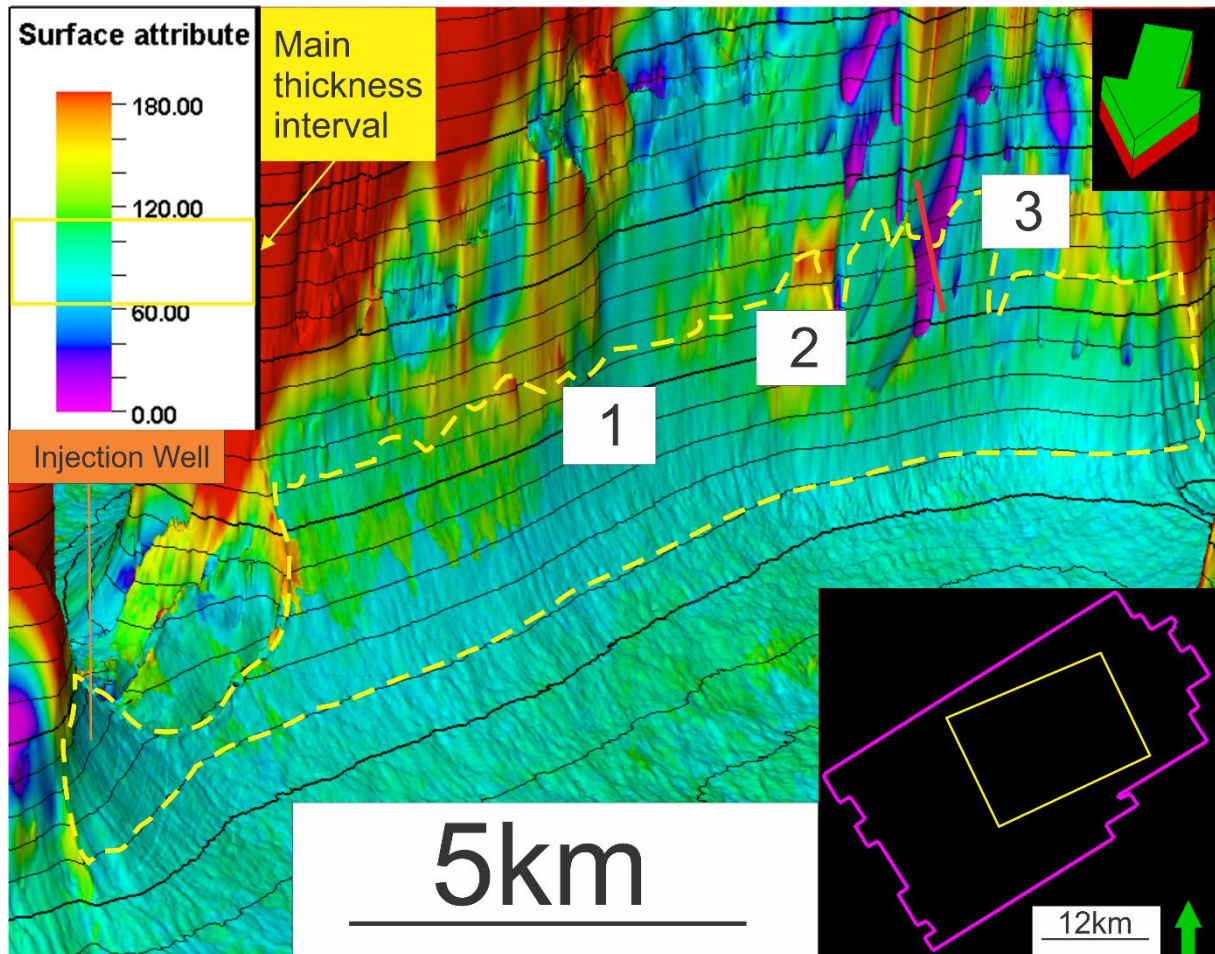## Top Stø Reflector-Top Fruholmen Reflector

Figure 4-11: An Isochron thickness map in TWT (ms) of the formations of Stø-Tubåen. Injection well (orange line) is included for convenience. Location of Xline 3032 (Figure 4-12) is marked as a red line, intersecting the thinnest part of the Stø-Tubåen interval. The contour lines are located on top of The Stø Reflector.
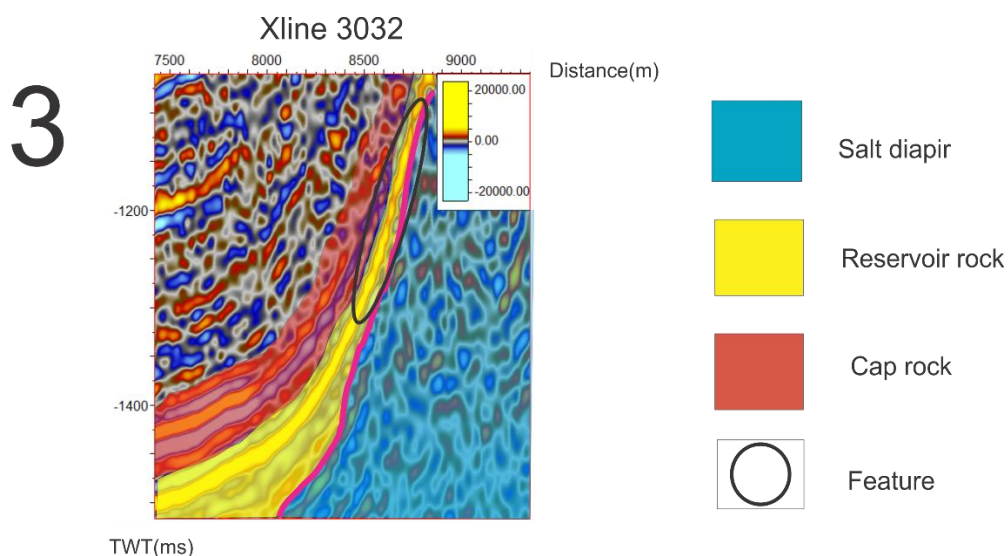
Figure 4-12: The thinnest interval of Stø-Tubåen is encircled in black. The interval of the Hekkingen-Fuglen formations is marked in red and the salt dome is marked in blue.

4.2.2.1.2 The Hekkingen-Fuglen Formations

The thickness of the Hekkingen-Fuglen interval is displayed as an isochron thickness map in TWT (ms) in Figure 4-13. A dotted line encircles the area of investigation, as mentioned in the previous section. The encircled area is slightly larger in Figure 4-13, than in Figure 4-11, and will be discussed in section 5.1.2.1.1.

The thinnest interval (4) of Hekkingen-Fuglen is located at the northern end of the largest salt dome in Figure 4-13, where the area is marked by a purple colour. It has a circular shape with a diameter of approximately 1km, with a suggested thickness of 10ms TWT from Xline 2054 in Figure 4-14. A general thinning is expected near the salt domes, as mentioned in the previous section.

Thicker intervals within Hekkingen-Fuglen (5 and 6) are seen further south in Figure 4-13. The thick intervals have elongated shapes, located in an NW-SE-direction, with lengths of 3-5km. Width measurement indicate 500m for both. The thicknesses are approximately 80-100ms TWT in Xline 2446 and Xline 3062 in Figure 4-14. Even though a general thinning of the formations are to be expected near the salt domes, as mentioned above, deformation of sediments may also result in thicker formations.

The maximum thickness Hekkingen-Fuglen is approximately 50ms TWT. This is observable near the bottom of the black, dotted line in Figure 4-13 in green-blue colours.

Isochron Thickness Map TWT(ms)
Top Hekkingen Reflector - Top Stø Reflector)
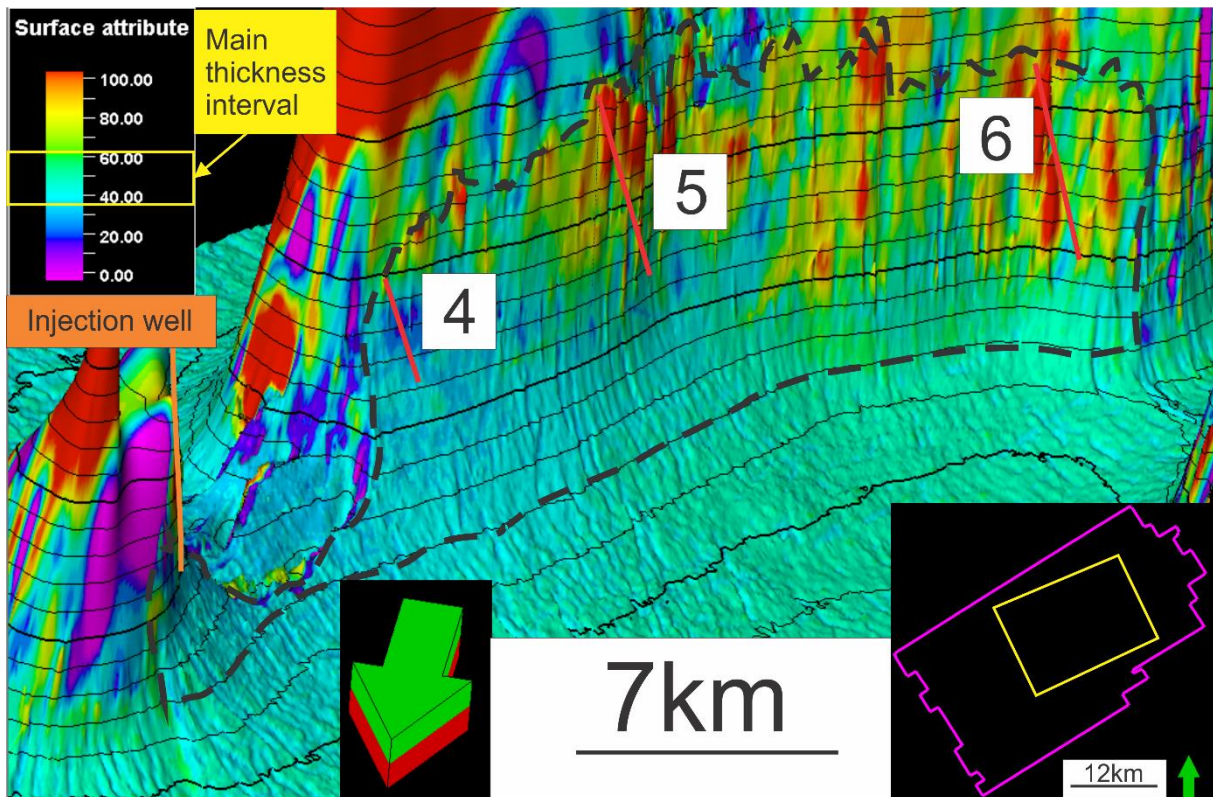
Figure 4-13: An Isochron thickness map in TWT (ms) of the Hekkingen-Fuglen formations. The thickness interval is approximately 50ms TWT, near the bottom of the investigated area (black, dotted line). Injection well (orange line) is included (orange line). Seismic lines are marked as red lines and displayed in Figure 4-14. The contour lines of the thickness map are located on top of The Hekkingen Reflector.
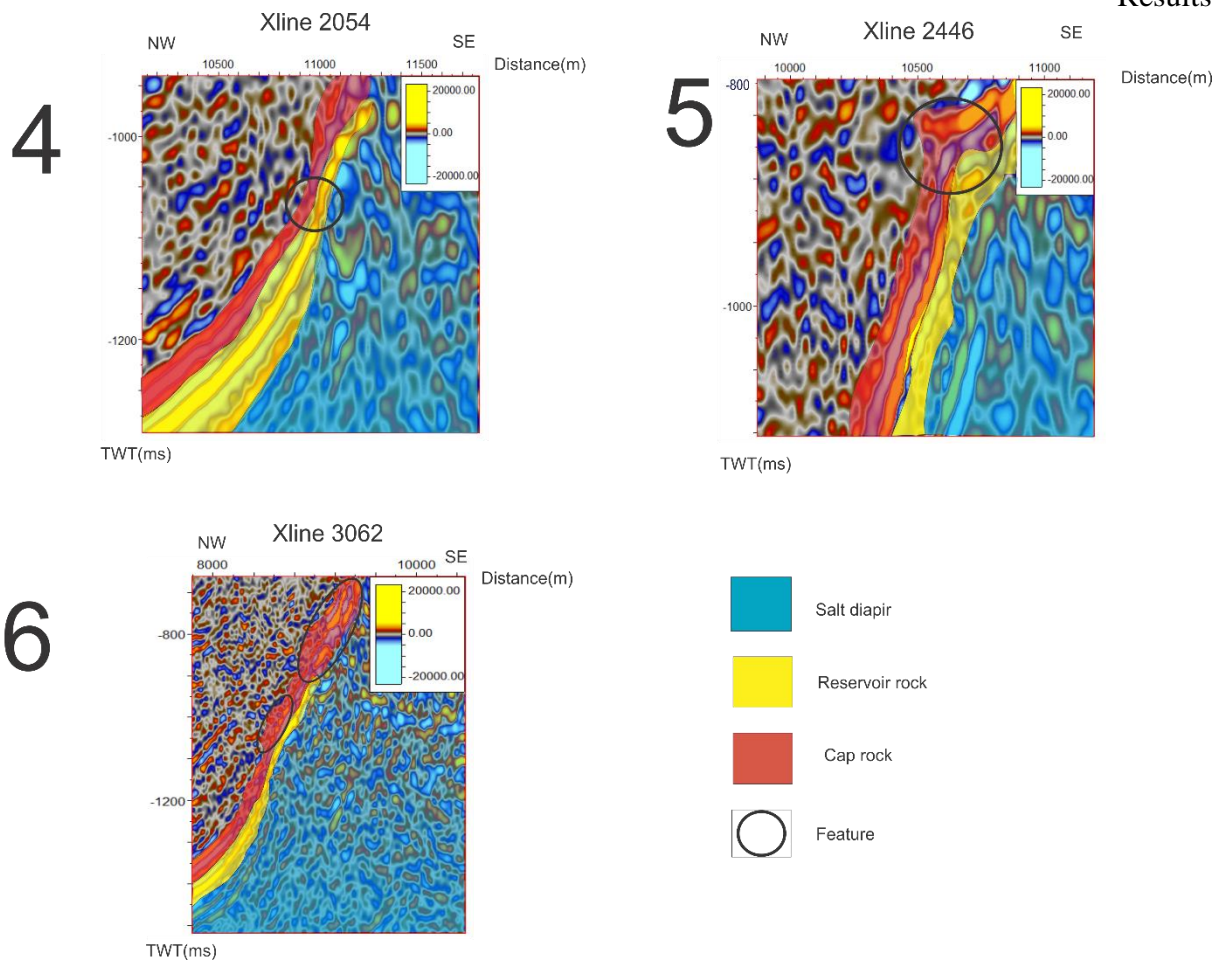
Figure 4-14: Seismic lines intersecting Figure 4-13. Xline 2054 marks the thinnest part of Hekkingen-Fuglen (black circle). Xline 2446 and Xline 3062 display the thickest parts of the interval of Hekkingen-Fuglen (black circles). The interval of Stø-Tubåen is marked in yellow and the salt dome is marked in blue.

4.2.3   Structural Boundaries

Structural boundaries of the intervals of Stø-Tubåen and Hekkingen-Fuglen are estimated in this section.

4.2.3.1   The Top Stø Reflector

A variance map is created for The Top Stø Reflector (Figure 4-15). The figure displays the top of the interval of Stø-Tubåen with discontinuous amplitudes. Only the area within the yellow boundary is considered, in resemblance to section 4.2.2.1.1.

46

Variance Map The Top Stø Reflector

Figure 4-15: A variance map for The Top Stø Reflector, the top of the interval of Stø-Tubåen. Yellow lines mark location of seismic lines. These seismic lines are displayed in Figure 4-17. A yellow circle marks the injection well.

The upper box (7) in Figure 4-15 displays a northern, elongated anticline. The anticline stretches between the yellow, seismic lines (7a and 7b), in a NW-SE-direction, for approximately 2km. The seismic lines are displayed in Figure 4-17, suggesting a height of approximately 50ms TWT high and width of 500m. The anticline is highly affected by faults (green lines) in Figure 4-17. These faults are stretching from the yellow area of Stø-Tubåen and up through the red area of Hekkingen- Fuglen. The faults are therefore interpreted to penetrate both intervals, and are most likely related to the underlying salt dome, seen in Figure 4-17. This salt dome penetrates the Stø-Tubåen interval and the Hekkingen-Fuglen interval in the upper part of the northern anticline (near the salt dome).

The middle box in Figure 4-15 is interpreted to display a fault-complex. The fault-complex stretches between the two seismic lines (8a and 8b), parallel to the yellow, dotted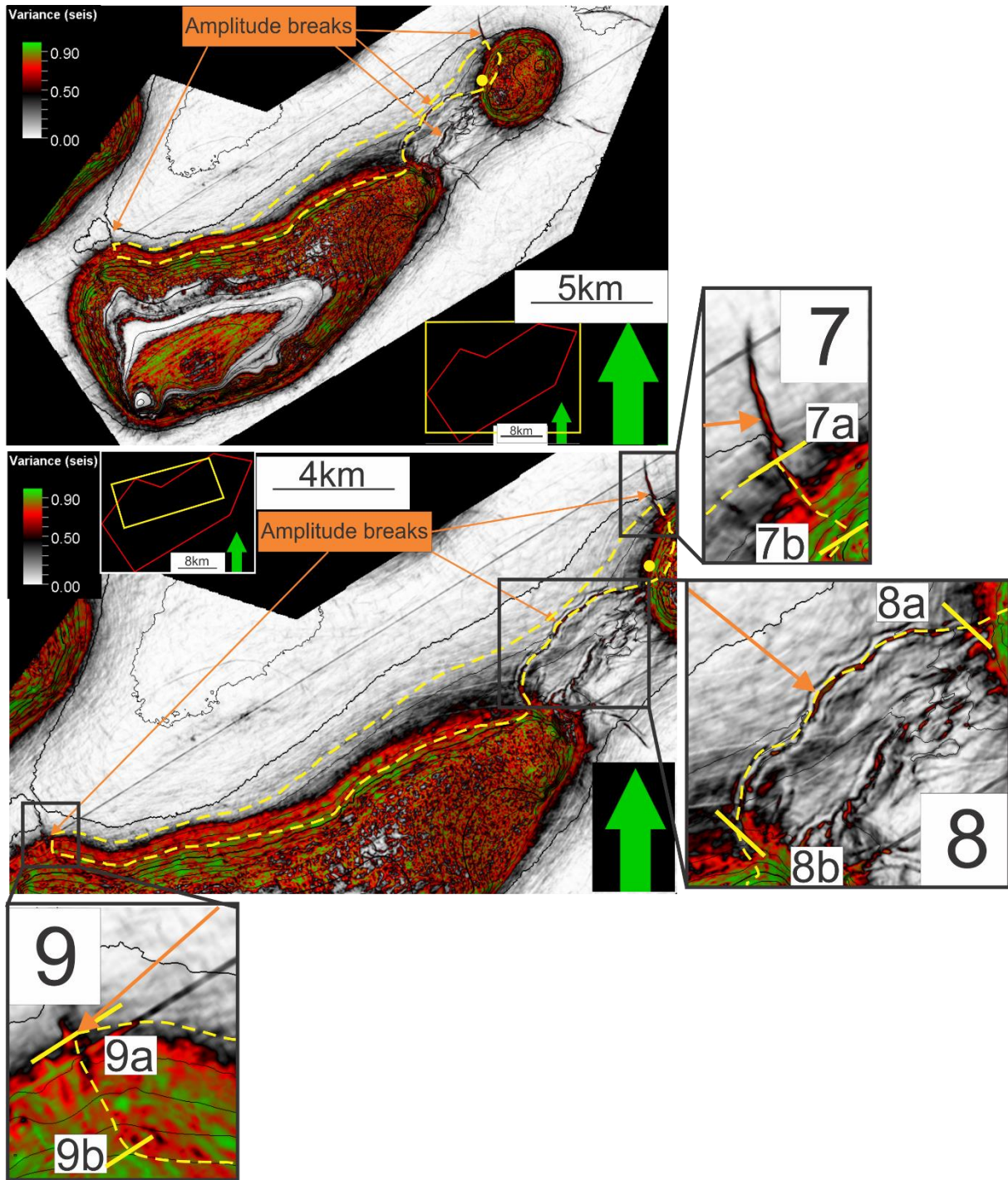 line in Figure 4-15. The seismic lines are displayed in Figure 4-17. The complex stretches in an NE-SW-direction for about 10km, and the fault throw is approximately 80-100ms TWT, suggested by Figure 4-17. The faults in Figure 4-17 suggests that the fault-complex penetrates both Stø-Tubåen and Hekkingen-Fuglen, in resemblance to the northern anticline, described above. The fault-complex is most likely caused by the underlying salt dome in Figure 4-17.

The lower box in Figure 4-15 displays a southern, elongated anticline, in resemblance to the northern anticline, described above. The anticline is 1.5km long and 500m wide in Figure 4-15, and extends in an NW-SE-direction, between the yellow, seismic lines (9a and 9b). The extension of the anticline is parallel to the yellow, dotted line. The height of the anticline is approximately 50-140ms TWT, suggested by Figure 4-17. The anticline is penetrated by faults (green lines) and a salt dome (blue body) in Figure 4-17. The faults are penetrating Stø-Tubåen and Hekkingen-Fuglen, similar to the faults of the northern anticline and the fault complex. The faults are most likely related to the underlying salt dome, as the salt dome penetrates the anticline in Figure 4-17. The salt dome is interpreted to penetrate the whole southern anticline of Stø-Tubåen.

The anticlines and the fault-complex are also displayed in Figure 4-16 below. Figure 4-16 is included as salt dome bends the interval Stø-Tubåen, making it difficult to recognize in 2D (Figure 4-15) near the salt domes.

The Top Stø Reflector TWT (ms)
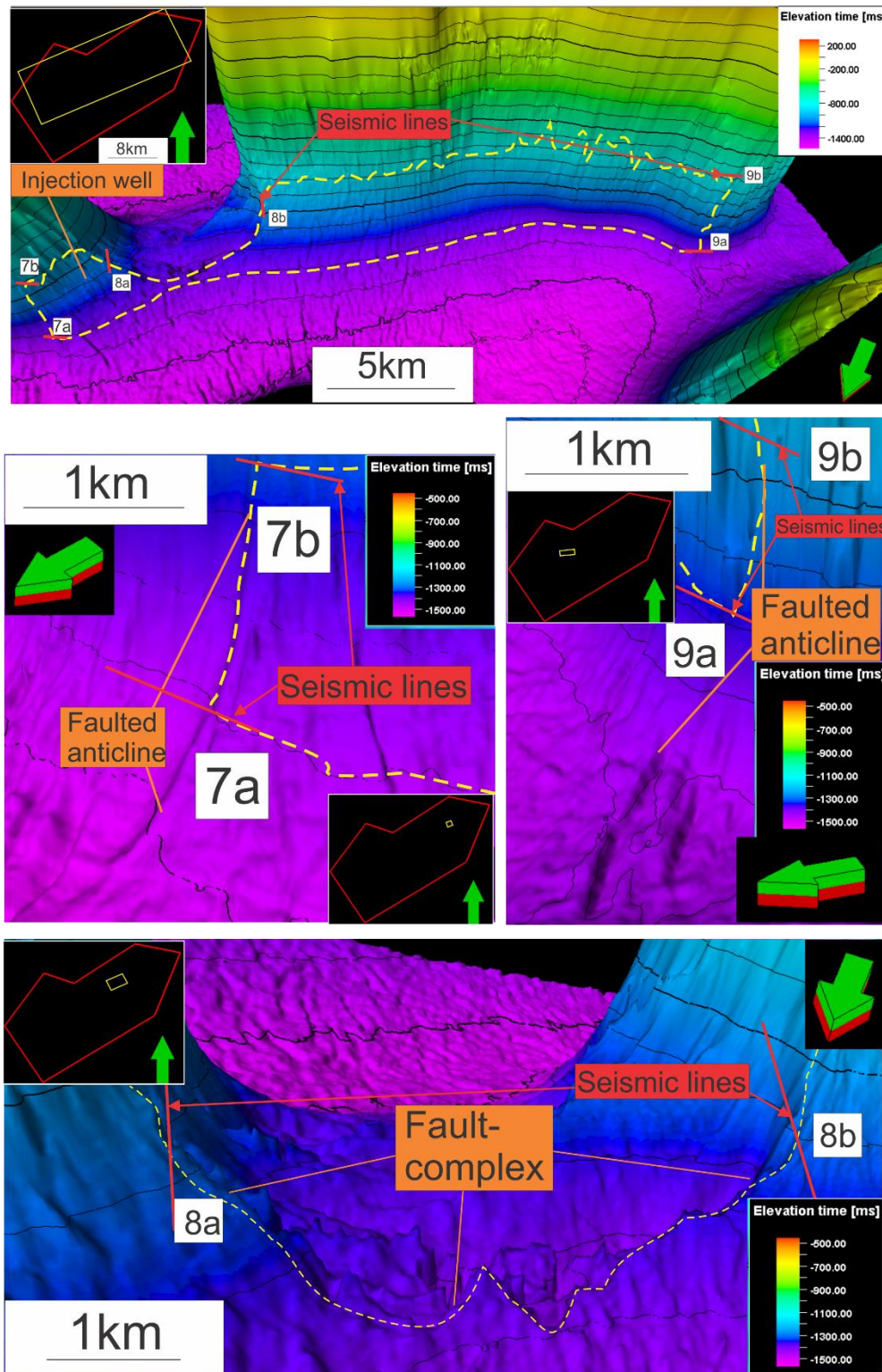
Figure 4-16: The Top Stø Reflector displayed in depth of TWT (ms). The Top Stø Reflector marks the top of the interval of Stø-Tubåen. Seismic lines (red lines) intersect the northern anticline (stretching between 7a and 7b), the southern anticline (stretching between 9a and 9b) and the fault-complex (stretching between 8a and 8b). The seismic lines are displayed in Figure 4-17. A yellow, dotted line outlines the investigated area.
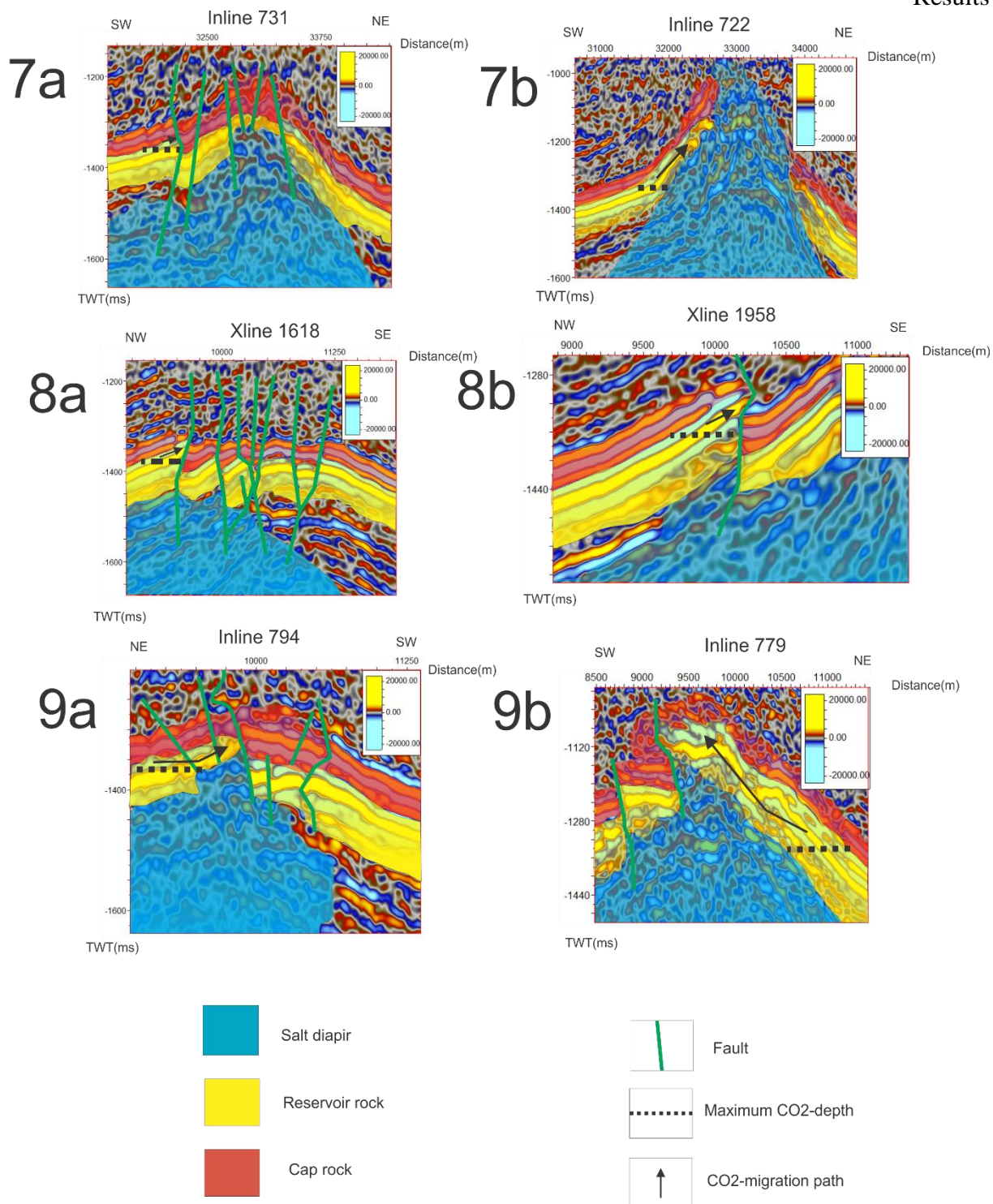
Figure 4-17: Structures from Figure 4-15 and Figure 4-16, displayed in Inline 731, Inline 722, Xline 1618, Xline 1958, Inline 794 and Inline 779. Inline 731 and 722 intersect the northern anticline, while Xline 1618 and 1958 penetrates the fault-complex. Inline 794 and 779 cross the southern anticline. Faults (green lines) intersect both the yellow area (Stø-Tubåen), and the red area (Hekkingen-Fuglen). The blue area marks extension of salt domes.

4.2.3.2   The Top Hekkingen Reflector

A variance map is created for The Top Hekkingen Reflector in Figure 4-18. The Top Hekkingen Reflector marks the top of the interval Hekkingen-Fuglen. Only the area within the green, dotted line is considered, in resemblance to section 4.2.2.1.2. Seismic lines are marked as yellow lines in Figure 4-18
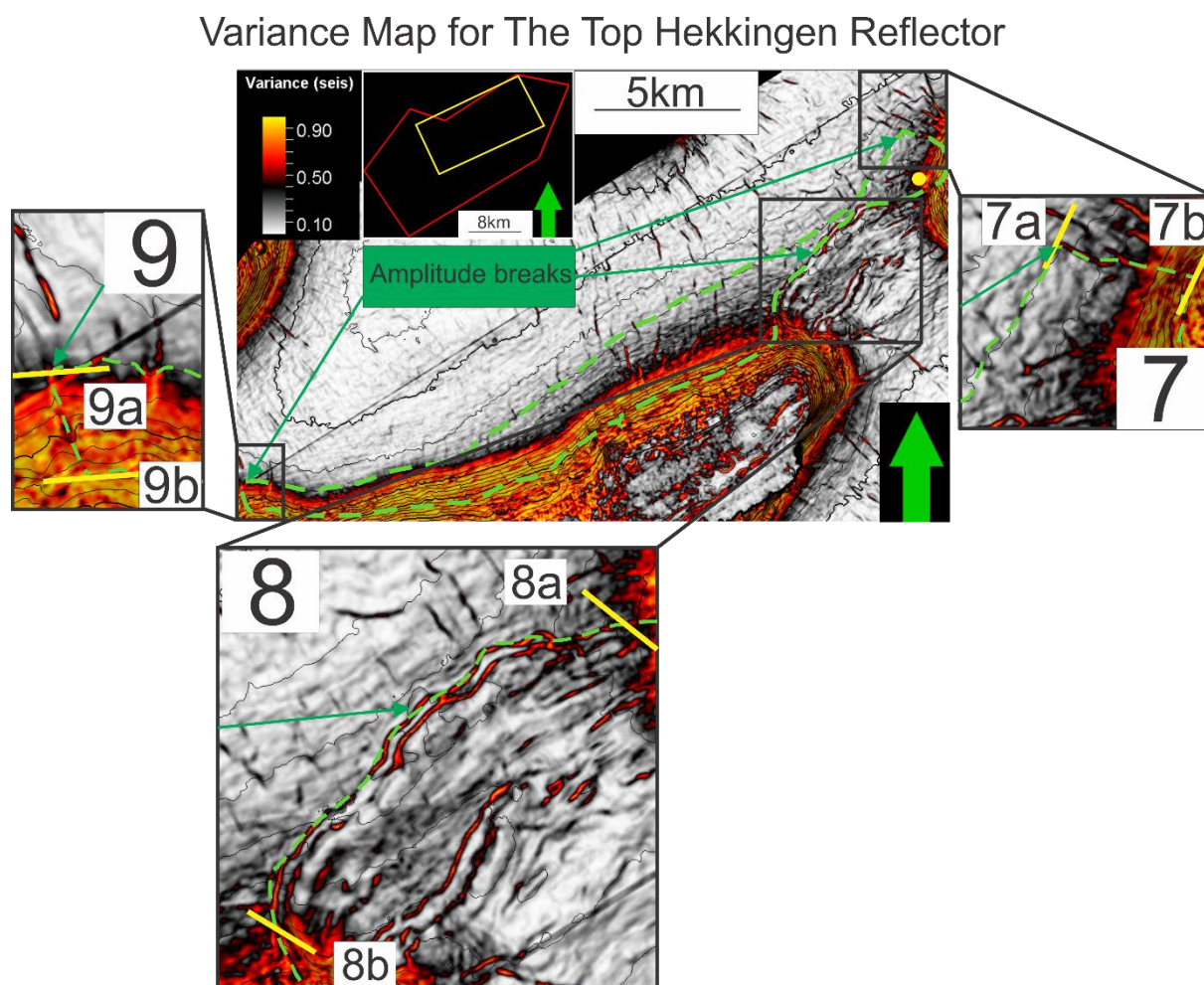
Figure 4-18: A variance map for The Top Hekkingen Reflector. Yellow lines mark location of seismic lines. These seismic lines are displayed in Figure 4-17. A yellow circle marks the injection well.

The upper box in Figure 4-18 displays the northern anticline (7), described in section 4.2.3.1, for the top of the Hekkingen-Fuglen interval. The penetrating faults and shape of the anticline, described in section 4.2.3.1, extends through Stø-Tubåen and Hekkingen-Fuglen in Figure 4-17, and this extension is seen in Figure 4-18, in red colours in between the seismic lines (yellow).

The same is the case for the fault-complex (8) and the southern anticline (9), described in section 4.2.3.1. The faults and shapes extends through Stø-Tubåen and Hekkingen-Fuglen (Figure 4-17), and this extension is seen in red in Figure 4-18, in between the seismic lines.

5 Discussion

5.1 The CO$_2$-Storage Complex

The following section will discuss the quality, thickness and boundaries of the reservoir and the cap rock. An estimation of the storage potential will follow at the end of this section.

5.1.1 Formation Intervals

5.1.1.1 Reservoir Rock

The preferred reservoir for CO$_2$-storage constitutes The Stø Formation, The Nordmela Formation and The Tubåen Formation, situated in between The Top Stø Reflector and The Top Fruholmen Reflector, as outlined in section 4.2.2. The choice is based on good reservoir properties, thick sand intervals and location of a reservoir at reasonable depths. The reservoir is displayed as the yellow area in Figure 5-1. Figure 5-1 is meant to sum-up all estimations conducted in section 4, including faults, anticlines, cap rock etc. and will be discussed in the following text.

The good reservoir properties are interpreted from well 1A in section 4.2.2. The reservoir interval, from 1361-1494mMD, consist of particularly clean, homogenous sandstone (NPD, 2015), more extensive and homogenous than the sand intervals within The Fruholmen Formation or The Snadd Formation below. The reservoir seems to consists of a 133m thick sand package (Figure 4-10), but the tighter interval, at 1420-1440mMD, reduces the total reservoir thickness to 113m. This tighter interval is discussed in section 5.2.4.

The reservoir is as thin, or thinner, than the formations of Fruholmen and Snadd, as suggested in section 4.2.2.1. The formations of Fruholmen-Snadd are more extensive, but the shale-content is higher. The well logs of 1A indicate a much more homogenous reservoir for Stø-Tubåen, and the Stø-Tubåen interval is preferable. The formations of Stø-Tubåen are located at shallower depths, which is still is within the preferred CO$_2$-storage depth-window (800-2500m) (Halland et al., 2013). A shallower injection depth indicates less economical expenses, and speaks in favor of Stø-Tubåen as a reservoir.

5.1.1.2 The Cap Rock

The best suitable cap rock is interpreted to consist of the Hekkingen – and the Fuglen formations. These formations are situated in between The Top Hekkingen Reflector and The

Top Stø Reflector, as outlined in section 4.2.2. The interval is encountered in 1A, located on top of the reservoir (Figure 4-9). The well logs indicate a particularly thick and homogenous shale-interval (47m), and the general assumptions about The Hekkingen Formation being a particularly suitable cap rock in The Barents Sea (Halland et al., 2013), adds additional weight to the choice. The interpretation of the cap rock being located right above the reservoir contributes. A closely located cap rock increases the amount of control for the CO_2-storage complex.

The homogeneity is assumed for the whole reservoir and cap rock. 1A is the only well drilled in close proximity of the reservoir, and the only reference point for measurements.

5.1.2   Extension of Storage Complex

5.1.2.1   Reservoir Extension and Thickness

The following anticlines and the fault-complex are outlined in section 4.2.3.1, and are displayed in cross-sections (black boxes) at the top of Figure 5-1. Red lines mark the location of the black boxes on the map in Figure 5-1, and all spill-points are interpreted from Figure 4-17. The following text outline why the reservoir extension is chosen (yellow area in Figure 5-1), bound by the anticlines and the fault-complex.

When the CO_2 is injected into the reservoir, from the injection well 1A, the CO_2 is expected to migrate towards the apex of the smallest, northernmost salt dome, seen on the map in Figure 5-1. However, this migration route is limited by the northern anticline (orange dotted, line) and the fault-complex (black lines). If migration occurs around the northern salt dome in Figure 5-1, the spill-point of the northern anticline (1500ms TWT) needs to be exceeded (black box). This spill-point is interpreted from 7a in Figure 4-17, as the anticline is flattening to the NE. No migration will occur across the upper parts of the northern anticline (7b in Figure 4-17), near the salt dome, as the salt dome separates the upper reservoir. This is outlined in section 4.2.3.1. Migration will only occur in the lower parts of the northern anticline and is displayed in Figure 5-1. Before the injected CO_2 reaches 1500ms TWT in the lower parts, the CO_2-plume will migrate along the fault-complex in Figure 5-1 (map), towards the larger salt dome further south. This southward migration occurs at 1375ms TWT (orange box). The limit is interpreted from e.g. Figure 4-16 by following the contour lines on the map. This lower limit will be discussed later in this section.

54

The same southward migration-scenario occurs if the plume is expected to migrate SE-wards, around the smallest salt dome and across the fault-complex on the map in Figure 5-1. The spill-points of the fault-complex are 1400-1440ms TWT (black boxes in Figure 5-1) and spill-points are interpreted from Figure 4-17 (8a, 8b), as mentioned earlier. The spill-points are below the limit for southward migration along the fault-complex (1375ms TWT), as outlined above. Migration of CO_2 around the smallest salt dome will not happen, as migration occurs in southward directions when depths exceed 1375ms TWT.

If injection depths are less than 1375ms TWT, the CO_2-plume will be held in place by the northern anticline and the fault-complex, and prevented from migrating southwards. The resulting area is seen as Area 2 in Figure 5-1. The amount of injected CO_2 will be very limited, as the gross rock volume is relatively small. The volume is rejected as a suitable reservoir, as the resulting volume is considered too small (approximately $0.18km^3$, calculated in Figure 5-2).

A larger reservoir area is encountered, if storage around both salt domes (the southernmost- and northernmost salt domes) on the map in Figure 5-1 is conducted. This reservoir is rejected due to an extensive salt-contact (blue areas in Figure 5-1). Salt is associated with hazardous chemical reactions and waste, as outlined in section 1.4.2.6.2, and storage around both domes is preferable to avoid.

The reservoir is chosen (yellow area in Figure 5-1), to limit the salt-contact. Injected CO_2, at depths of 1375ms TWT, will be trapped by the northern anticline and the fault-complex, with spill points at 1400ms TWT and 1400-1440ms TWT respectively (black boxes, Figure 5-1), as outlined above. The anticline and the fault-complex will prevent northward- and eastward migration. Further southward migration is prevented by the southern anticline (seen on map and black box in Figure 5-1). No migration will occur across the southern anticline, as the reservoir is separated by a salt dome (9a, 9b in Figure 4-17), as outlined in section 4.2.3.1.

The reservoir in Figure 5-1 is therefore enclosed by the anticlines and the fault-complex at 1375ms TWT, where 1375ms TWT is the lower reservoir limit. The lower limit is displayed on the map and in the cutting-segment (bottom figure) of Figure 5-1.

The shape of the lower reservoir limit, in between the structures in Figure 5-1, is based on following the contour lines, occurring at 1375ms TWT, in Figure 4-11, Figure 4-15 and Figure 4-16, as mentioned above.

The maximum injection depth (1375ms TWT), outlined above, is relatively uncertain. If a sediment velocity of $2000ms^{-1}$ is assumed, the injection depth in Figure 5-1 occurs at

1375m. The same injection depth is relocated to 1794m depth, if a velocity of 2610 ms^{-1}, from well 1A (Figure 3-2), is used. Both calculated depths are within the preferable CO_2-depths (800-2500m), according to Halland et al. (2013).

The upper reservoir limit is marked on the map and in the cutting-segment in Figure 5-1, at 850ms TWT (orange box). The upper reservoir limit is interpreted from where the reservoir terminates against the salt dome in Figure 4-14, and is displayed in Figure 4-11, Figure 4-15 and Figure 4-16. If approximate depths were to be considered for the upper reservoir-limit, in accordance to the lower reservoir-limit outlined above, the upper limit will be located between 850m (at 2000ms^{-1}) and 1109m (at 2610ms^{-1}). This is within the preferred storage depths outlined above. The Sleipner Site (Table 3-1) injects CO_2 at 800-1000m depth (Lindeberg et al., 2009, Halland et al., 2013), and proves that it is feasible. Therefore, the reservoir in Figure 5-1 is interpreted to be located at safe storage depths, as most calculations are within 800-2500m for both the upper- and lower limit.

Based on the reservoir limits (850-1375ms TWT) in Figure 5-1, the maximum reservoir thickness should be 525ms TWT. This is not in accordance with section 4.2.2.1.1 (Figure 4-11, Figure 4-12), where the reservoir thickness is 100ms TW. A thickness of 100ms TWT is also supported by section 4.2.2.1.2 (Figure 4-14) and 4.2.3.1 (Figure 4-17). A general thickness of 100ms TWT is therefore considered more reliable. This thickness is calculated in Figure 5-2.

The upper reservoir limit in Figure 5-1 is most likely the cause of this measurement gap, between 525 and 100ms TWT. The upper limit is based on random lines in Figure 4-14, as outlined above, with noisy data, as mentioned in section 3.1. However, the upper reservoir-limit is included as a relative guidance of reservoir extension, even though it is not accurately measured.

5.1.2.1.1 Cap Rock Extension

The cap rock is not assessed in the same amount of detail as the reservoir, but is still important to highlight a few key factors.

All seismic sections, throughout this thesis, indicate a covering cap rock for the reservoir (Figure 4-8 to Figure 4-17). This cover is displayed as red lines, covering the reservoir area, on the map in Figure 5-1. Figure 4-8 suggests a covering cap rock in areas outside the reservoir, but this is left out on the map in Figure 5-1 for simplicity. The covering cap rock is indicated in the cutting-segment (bottom figure) in Figure 5-1, where the cap rock (red colour) is

extending outside the reservoir and further up the salt dome. This further extension is interpreted from section 4.2.2.1.1 (Figure 4-12 to Figure 4-17). However, the exact upper cap rock-limit is not calculated.

The cap rock follows the same thinning-trend towards the salt domes in Figure 5-1 as the reservoir, as outlined in section 4.2.2.1.2.

To sum up section 5.1.2 so far, the reservoir is assumed to be located in between a cap rock and two salt domes. The cap rock and the salt dome are assumed to be vertical barriers, holding the CO_2 in place within the reservoir. The horizontal barriers are formed by the anticlines and the fault-complex. The CO_2 is assumed to be held in place by a trap structure, caused by salt domes, where inclined sediments against the salt domes form the trap structure.
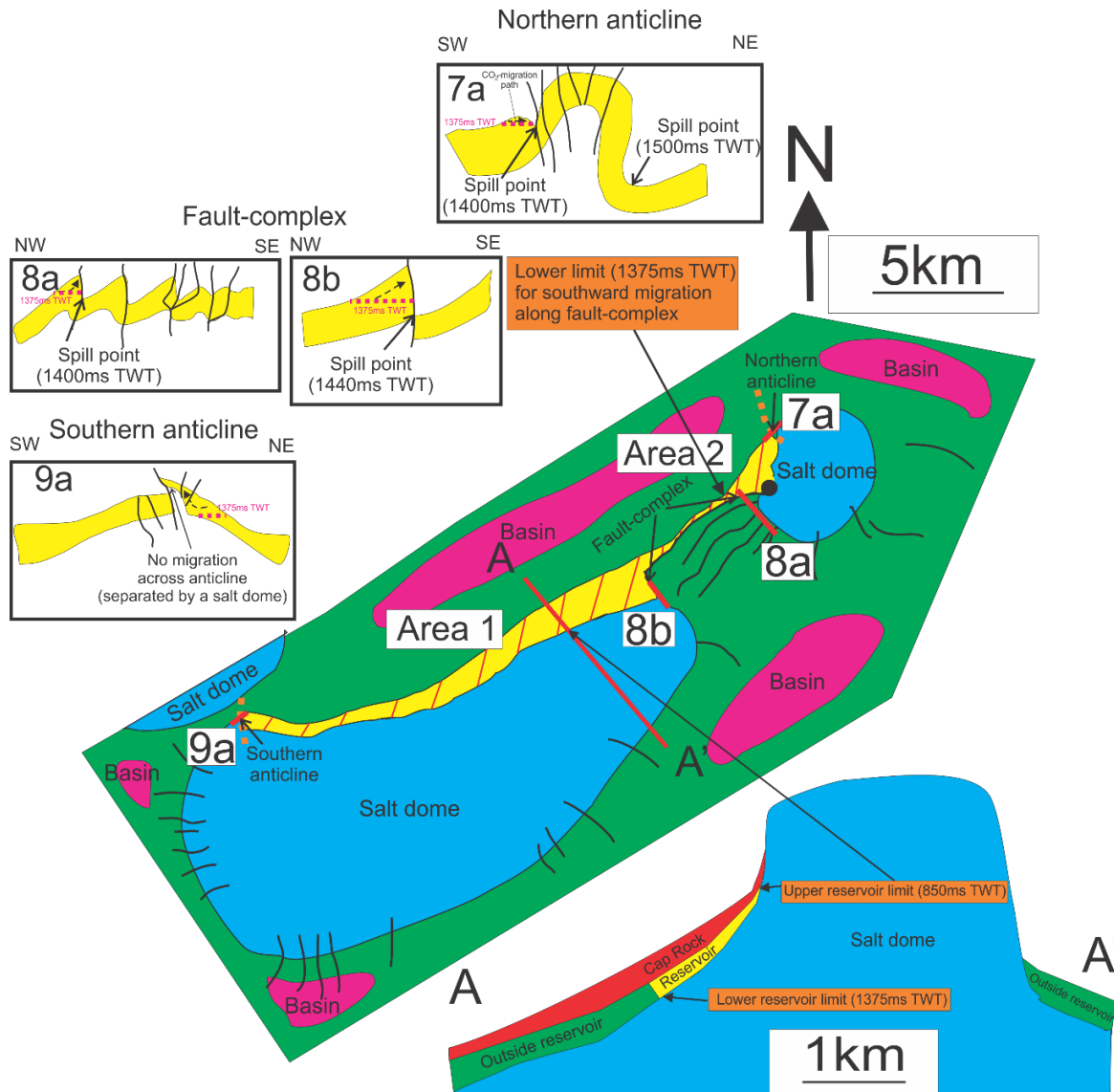
Figure 5-1: A summarized model of the CO₂-storage complex. Extensions of the anticlines and the fault-complex are estimated from Figure 4-15 to Figure 4-18, and the spill-points from Figure 4-17. The overall structure of the reservoir (Stø-Tubåen), the cap rock (Hekkingen-Fuglen) and the salt domes are based on Figure 4-3 to Figure 4-18. The upper reservoir limit is estimated from Figure 4-14, while the lower reservoir limit is estimated from the contour lines of Figure 4-11, Figure 4-15 and Figure 4-16.

Top figure (black boxes): The fault-complex (8a, 8b) and the northern (7a)- and the southern anticline (9a) are displayed in cross-sections with spill-points. The faults (black lines) are penetrating both the reservoir and the cap rock.

Middle figure (map): The CO₂-reservoir within Stø-Tubåen is marked in yellow, the cap rock (Hekkingen-Fuglen) is displayed as red lines covering the reservoir. The green and pink colours mark Stø-Tubåen outside the reservoir, where the pink colour display the lowest points (basins). The cap rock is assumed to cover the whole interval of Stø-Tubåen (yellow, pink and green colours), but only displayed above the reservoir for simplicity. Salt domes (blue) marks the highest points in the figure. Injection well is marked as a black circle. An orange, dotted line on the map marks the extension of the anticlines, and faults are displayed as black lines. The red lines, penetrating the fault-complex and the anticlines, mark where the black boxes (top figure) intersect. These boxes display the anticlines and the fault-complex in cross-sections. The reservoir is limited by the anticlines and the fault-complex. The numbers (7a, 8a, 8b, 9a) resemble Figure 4-17. 7b and 9b from Figure 4-17 are excluded for simplicity. The lower limit for southward migration (1375ms TWT), outlined in section 5.1.2.1, is marked (orange box) along the fault-complex.

Bottom figure (cutting-segment): The salt dome (blue) is the highest point in the model. The green colour marks Stø-Tubåen outside the reservoir. The reservoir (yellow) forms a trap structure as it is thinning towards the salt dome. The cap rock (red) covers Stø-Tubåen throughout (yellow and green areas) and extends further up the salt dome than the reservoir. Maximum injection depth (pink, dotted line) is defined at 1375ms TWT and upper reservoir limit at 850ms TWT.

5.1.2.1.2   Volume- and Thickness Calculations

The gross rock volume is calculated in Figure 5-2, based on a top- and base reservoir interpretation (wedge model in cutting-segment of Figure 5-2). The thinnest part of the wedge marks the termination of the reservoir against the salt domes, 0ms thick (at 850ms TWT), and the thickest part of the wedge is 50ms thick (at 1375ms TWT), as outlined in section 5.1.2.1.

Since the reservoir (yellow area) decreases along the fault-complex in Figure 5-1, two wedges are calculated. Area 1 in Figure 5-1 is particularly variable in width, and an average width is therefore estimated. The average velocity for the reservoir is estimated in Figure 3-2 (3718ms^{-1}), and the total area (length and width) is measured by distance-tools in Petrel. The total reservoir volume is *2km^3*.

A general thickness estimation is also conducted for the cap rock. This calculation is displayed in Figure 5-3. The cap rock is assumed to cover the whole reservoir, as outlined in the previous section. Therefore, only a cap rock-thickness is of interest. The cap rock is 25ms at its thickest, as outlined in section 4.2.2.1.2. The velocity is estimated from Figure 3-2 (2610ms^{-1}), and the maximum thickness is therefore *65.25m*. The thinnest interval in the figure (*47m*) is calculated from the cap rock-interval within 1A, at 1314-1361mMD in Figure 4-9. This minimum thickness is based on the cap rock extending further up the salt dome than the reservoir, as outlined in the previous section. 1A is located close to the upper reservoir-limit, and is a reasonable value for the cap rock-thickness.

It is important to enhance that the volume- and thickness-calculations are related to a degree of uncertainty. Estimation of an average velocity and use of distance-tools in Petrel are the most significant.

Reservoir Volume

Width

Reservoir volume

$(50 \times 10^{-3}\text{ s}) \times 3718\text{m/s} = \textbf{186m}$
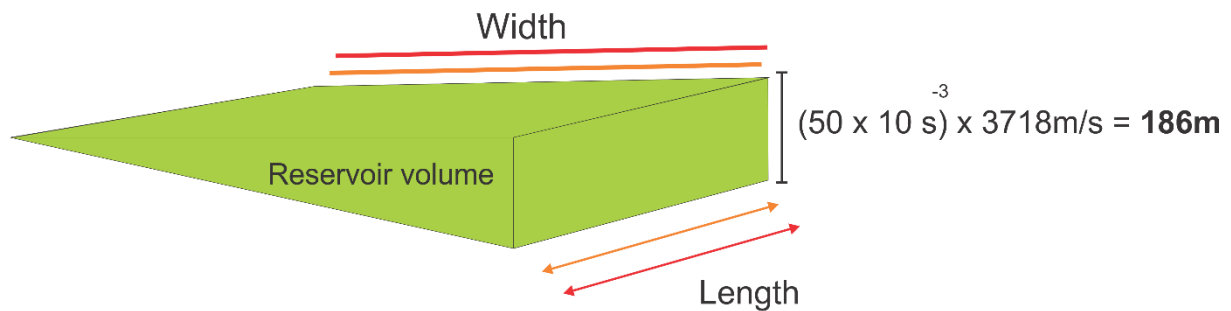
Length

Area1

Length = **15844m**
Width = (1757 + 664)m/2 = **1210.5m**

Area 2

Length = **2164m**
Width = **876m**

Total Area

21 074 826 m^2 = **21km²**

Total Volume

$(21\text{km}^2 \times 0.186\text{km})/2 = \textbf{2km}^3$

Figure 5-2: A general volume calculation for the CO_2-reservoir in Figure 5-1. The length and width of the reservoir is measured by distance-tools in Petrel, with an average width-estimation for Area 1. The thickness is based on an average velocity (3718ms^{-1}) from 1A (Figure 3-2) and a general reservoir thickness of 100ms TWT.

Cap Rock Thickness

Cap rock thickness

$(25 \times 10^{-3}\text{s})\ 2610\text{m/s} = \textbf{65.25m}$

47m (from 1A)

Minimum thickness

Reservoir

Maximum thickness
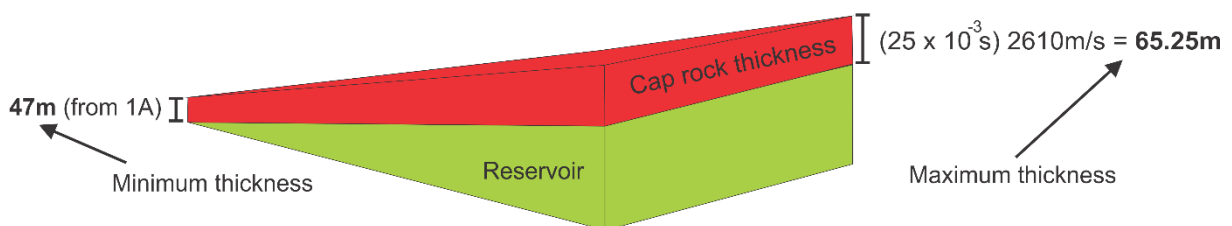
Figure 5-3: Only a thickness-estimation is of interest for the cap rock, since the extension is similar to the reservoir in Figure 5-2. The thinnest part of the cap rock is from 1A (47m) and the thickest is 50ms TWT. The velocity is estimated from Figure 3-2 (2610ms^{-1}).

5.1.3 CO_2-Storage Potential

The storage potential is calculated for the reservoir, as outlined in section 1.4.2.8 and 3.4.

Since the reservoir consists of homogenous sandstone (section 5.1.1.1), and porosity-measurements from 1S amount to 6-28% (section 4.2.2 and 2.2), a porosity of 10% seems

60

reasonable for the reservoir. This is also supported by porosity-measurements from The Snøhvit Site (Table 3-1), with porosity measurements of 10-16% at 2400-2600m depth. The reservoir is located at 1361m depth in 1A (NPD, 2015), but studies have indicated a maximum burial of the reservoir down to 2600m, as outlined in section 2.2. Hence, the reservoir has a burial history down to similar depths as The Snøhvit Site.

As outlined in section 5.1.1.1, the reservoir has clean sand intervals of 113m. However, this includes storage of CO_2 both above and below the tighter interval at 1420-1440mMD in 1A. A net-to-gross of $\left(\frac{113}{133}\right) \times 100\%$ or 84% is estimated for the reservoir, assuming storage both above and below the tight interval.

The density of CO_2 at storage conditions, outlined in section 1.4.2.6.1, is difficult to estimate for the CO_2-storage complex, as pressure-measurements are lacking from the reservoir. A general pressure gradient at 105 barkm^{-1} and a pressure gradient of 30°Ckm^{-1} is reasonable for The Nordkapp Basin, as outlined in section 1.4.2.6.1, and the reservoir conditions will be 143-157 bar and 41-45°C. The resulting density of CO_2 at reservoir conditions is 749-750kgm^{-3} (Wischnewsk, n.d.). This value is within the upper limits of the CO_2-density at The Snøhvit Site (650-750kgm^{-3}).

The last, estimated value from Table 3-1 is the storage efficiency factor (S_{eff}), as outlined in section 1.4.2.2. This factor is particularly difficult to estimate for the CO_2-storage complex, as it is variable from reservoir to reservoir (Halland et al., 2013). It is reasonable to assume that the reservoir is in contact with a larger aquifer, as the Stø-Tubåen interval extends beyond the reservoir area in Figure 5-1. The pore pressure within the reservoir is assumed hydrostatic, and a storage efficiency factor close to 5% is reasonable. An average value of 4% is implemented as an average from both CO_2-storage sites in Table 3-1.

The amount of injectable CO_2 (from Figure 1-10):

$$Mass\ of\ Injectable\ CO_2\ (M_{CO_2}) = V_b \times \varnothing \times \frac{N}{G} \times \rho_{CO_2} \times S_{eff}$$

$$M_{CO_2} = 2 \times 1000^3 m^3 \ \times 0.1 \ \times 0.84 \ \times 750 kgm^{-3} \times 0.04$$

$$M_{CO_2} = 5.04 \ \times 10^9 kg = \mathbf{5.04 Mt}$$

The predicted amount of CO_2 for the storage complex is 5.04Mt. Compared to the predicted amount from The Snøhvit- (40Mt) and The Sleipner Site (60Mt) in Table 3-1, this number is relatively small. It amounts to about 12% of the predicted amount into Snøhvit and 8% of the predicted amount into Sleipner.

The small number may have several causes, and one of the factors is the rock volume. The volume is only about half of the volume of The Sleipner Site and about a sixth of The Snøhvit Site. However, if the volume of the CO_2-storage complex is going to be increased, then an increasing salt- and fault-contact needs to be assessed, as outlined in 5.1.2.1.

The calculation is influenced by a relatively modest estimation for the porosity, as the porosity of the reservoir may be a bit higher (up to 28%). The N/G is relatively high for the reservoir, but not as high as the Snøhvit- and Sleipner sites in Table 3-1 (90% and 95%). The N/G is considered a good estimate for the reservoir, if injection occurs beneath and above the denser interval (1420-1440mMD).

The density at reservoir pressure is considered reasonable, since the maximum burial depth of the reservoir coincides with the injection depth at The Snøhvit Site (2600m), as outlined above. The exact density is difficult to determine without direct measurements of temperature and pressure. The most uncertain value of the calculation is the S_{eff}, as mentioned above. The S_{eff} is hard to predict before injection starts.

5.2 Leakage-Scenarios

This section will discuss leakages related to thickness of cap rock, faults, chemical reactions and pressure build-ups.

5.2.1 Cap Rock-Thickness

The properties of the cap rock is closely related to leakage, as outlined in section 1.4.2.4. A thick cap rock is preferable (>50m), and Figure 5-3 indicated a cap rock of 47-65m. The cap rock is safe, as the maximum thickness is close to 50m. Weight from the overburden, weight of 1314m thick sediment packages, adds additional safety. The thinnest part of the cap rock is described in section 4.2.2.1.2. The thinnest part of the cap rock is approximately 30m, if a velocity of $2610ms^{-1}$ is assumed. It is a bit thinner than the preferred thickness (>50m), but is not considered a problem, as overburden will contribute.

5.2.2 Faults

The faults of the anticlines and the fault-complex (Figure 5-1) are extending through the reservoir and up through the cap rock, as outlined in section 4.2.3.1.

The origin of the faults may be related to glacial cycles, as outlined in section 2.1, but are most likely related to the underlying salt domes, as the salt domes are in close proximity. The salt domes are considered stable enough for hydrocarbon exploration, as outlined in section 4.2.1, and the faults of the fault-complex and the anticlines are therefore not active. This inactiveness suggests tight faults, and the faults are therefore not considered a leakage risk. The exact vertical extent of the faults were impossible to map, due to noisy data (section 3.1).

5.2.3 Hazardous Chemical Reactions

5.2.3.1 Salt-Related Risks

The reservoir is a saline aquifer, as the reservoir was proven water-wet in 1A (NPD, 2015). The reservoir has a high chance of increased salinity near the salt domes in Figure 5-1. Salty water (brine) absorb less CO_2 than brackish water, as outlined in section 1.4.2.6.2. This increased salinity results in less CO_2 reacting with formation water, and hence less carbonic acid will form, as outlined in section 1.4.2.6.3. This decrease in dissolution of CO_2 will increase the amount of occupied pore space and lower the amount of solubility trapping, outlined in section 1.4.2.3. The reservoir is in contact with a larger aquifer, as outlined in section 5.1.3, and little

dissolved CO_2 is not considered a risk, as the CO_2 will push the formation water away from the injection well.

The formation water has a high salinity, as mentioned above. This high salt-content will most likely lead to salt precipitation within the reservoir. Salt causes blockage near the injection well, as outlined in section 1.4.2.6.2. If the injected CO_2 is dry (<50 ppm water content (Halland et al., 2013)), more salt might precipitate. A drying of the rock formations occurred at The Snøhvit Site, as outlined in section 1.4.6.2. A methyl-ethyl-glycol-injection (MEG) prevented this precipitation (Hansen et al., 2013), but increased the economic expenses. If the CO_2 is water-wet (>50ppm (Halland et al., 2013)), the chances of corrosion within pipelines and well-equipment increases. The Sleipner Site is injecting water-wet CO_2 (Koeijer et al., 2013), and a water-wet gas is therefore the best solution for the CO_2-storage complex, as salt precipitation is considered likely to occur, due to high salinity.

5.2.3.2 *Carbonate-Related Risks*

It is commonly known that carbonic acid dissolves carbonates, and the well 1S encountered an unexpected carbonate ($CaCO_3$) during drilling, as mentioned in section 2.2. This carbonate is located near the northernmost salt dome in Figure 5-1. The carbonate is not recognizable from seismic data, and the exact extension of the carbonate is therefore not known. Figure 5-4 displays a suggested carbonate extent, where the work after Henriksen et al. (2011b) is correlated with the seismic data of this thesis (Inline 697). The reservoir extension of the CO_2-storage complex is displayed in yellow in Figure 5-4 and the cap rock is displayed in green. The injected CO_2 will most likely encounter this carbonate.
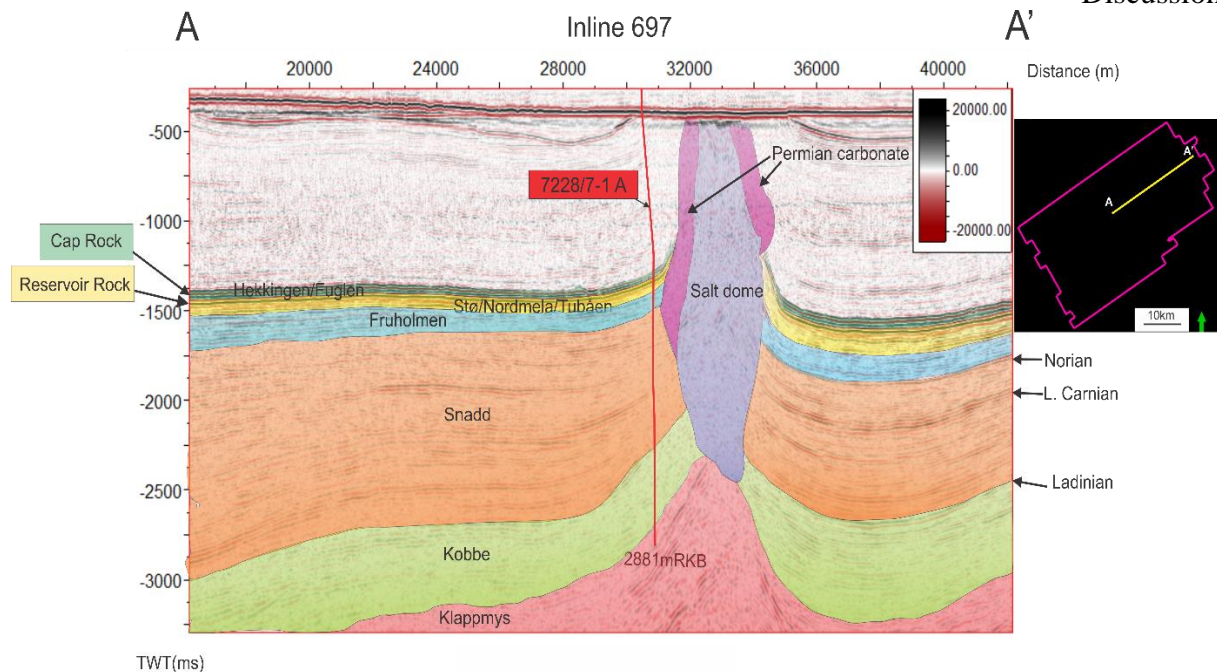
Figure 5-4: Model for the extension of the carbonate, which is not recognizable from seismic. The exact extension of the carbonate is not known. The injected CO₂ may encounter the Permian carbonate, and risks related to the following chemical reactions needs to be assessed. Model is based on work after NPD (2015) and Henriksen et al. (2011b) and correlated with the seismic data of this thesis (Inline 697). The injection well is marked in red.

Precipitation of calcium bicarbonate, as outlined in section 1.4.2.6.3, is considered unlikely to occur within the CO_2-storage complex. Precipitation occurs at high pH-values, and the storage complex is assumed a little acidic. The acidity occurs from dissolved CO_2, as outlined in the previous section.

Hydrogen chloride (HCl) may form due to contact between hydrons (H^+) and chloride (Cl), as outlined in section 1.4.2.6.3. The reservoir temperature is 41-45°C, calculated in section 5.1.3, and carbonates are of retrograde solubility (section 1.4.2.6.3). Even if the temperature allows dissolution of carbonate, the reaction is dependent on composition of unknown formation fluids. It is therefore impossible to conclude on the matter. If dissolution occurs, the CO_2 is allowed to penetrate the carbonate (pink colour) in Figure 5-4. The figure suggest a possible migration route in between the salt dome (purple area) and the cap rock (green area). The escape route will have devastating effects. Dissolution produces more CO_2, as outlined in section 1.4.2.6.3, which will in turn increase the reservoir pressure and increase the migration.

Tests related to CO_2-storage within carbonate rocks have been carried out and is feasible (Izgec et al., 2006). CO_2-storage with present salt formations are implemented, as mentioned in section 1.4.2.1 and 1.4.2.6.2. However, little information is published on CO_2-storage with both

carbonates and salt domes present. The corresponding chemical reactions of carbonates and salt domes are therefore the biggest risk of the CO_2-storage complex of this thesis.

5.2.4 Injection Intervals

The tight interval within the reservoir (1420-1440mMD), outlined in section 5.1.1.1, remains to be considered. This tightness is assumed continuous throughout the reservoir, as mentioned in section 5.1.1.2.

In general, a maximization of injected CO_2 is preferable for the CO_2-storage complex, with injection both above and below the tight interval. If pressure increases below the tight interval, injection will only occur above the tight interval. The pressure build-up is not expected, as the properties of the reservoir are good (NPD, 2015).

5.3 Potential Storage Locations

Salt and carbonates are preferable to avoid, as outlined above. Could the reservoir be located anywhere else within the 3D-cube for safer storage?

The salt domes extends throughout the 3D-cube, and are in close proximity of the present-day seafloor, as outlined in section 4.2.1. The salt domes are therefore difficult to avoid for CO_2-injection. If a storage unit is located within the basins (purple areas) in Figure 5-1, migration will occur towards the salt domes. This will happen if storage occurs in other formations too, as the sediments are parallel (section 4.2.1). In other words, CO_2 will encounter a salt dome no matter where it is injected within the 3D-cube.

The Permian carbonate is of less extent. The well tracks 1A and 1B did not encounter any carbonate (NPD, 2015), which suggests that the carbonate is relatively small. A reservoir further away from the carbonate is a better solution, as the carbonate is avoidable. A possible storage unit is the salt dome NW of the reservoir, extending outside the 3D-cube in Figure 5-1. The salt dome is far away from the encountered carbonate and well 1A.

5.4 Risking

The following tables sum up the qualities and uncertainties related to the reservoir properties (Table 5-1) and sealing properties (Table 5-2) for the CO_2-storage complex assessed in this thesis. The risking process is modified after Halland et al. (2013). The process includes giving quality numbers 0-3, where 0 is a low quality number and 3 is a high quality number, as outlined in section 1.4.2.7 and 3.4.

Table 5-1 displays the structure of the reservoir, its belonging properties and possible chemical reactions between the CO_2 and the reservoir. A low quality number in the table implies little available information, assumed low quality of the reservoir properties, assumed low quality of reservoir structure, or a high risk of hazardous chemical reactions. A high quality number implies a lot of available information together with good quality indications or low chance of dangerous chemical reactions.

Table 5-2 displays risks related to holding the CO_2 in place after injection. These risks involve the encountered fault-complex, anticlines, the two salt domes and the overlying cap rock. A low quality number for Table 5-2 implies little available information available or a high chance of leakage through the sealing mechanisms. A high quality number implies a lot of available information and a low chance of leakage.

Reservoir Properties	High Quality	Low quality	Description of Reservoir	Quality number
Aquifer structuring	Mapped or possible closures	Tilted, few/uncertain closures	Slightly tilted towards salt structures. Relatively flat aquifer, except near salt domes.	1
Chemical properties	No risk of dangerous chemical reactions	High risk of chemical reactions	High risk of leakage due to hazardous chemical reactions between CO_2, carbonate and salt domes.	0
Traps	Defined sealed structures	Poor definition of traps	Salt pillows have created the overall trap structure. Vertical extension of faults are uncertain, but the faults are tight. Some faults have a low throw, resulting in a chance of migration across the faults at 1400ms TWT for the fault-complex and the northern anticline.	1
Reservoir volume	>10km^3	<2km^3	Relatively small reservoir volume (2 km^3), even at 1375ms TWT injection depth.	1
Net thickness (N/G)	>50m	<15m	113m within 1A, if injection depth occurs above and below 1420-1440mMD. Reservoir is thinning towards the salt pillows.	3
Depth	800-2500m	<800m or >2500m	Velocity in sediments are unknown <600mMD, and an upper limit at 800m depth and lower limit at 1375m is therefore estimated for the reservoir. However, the reservoir is considered to be located at safe storage depths.	2
Homogeneity	Homogenous	Heterogeneous	Good properties proven in 1A. Homogeneity is assumed for the whole reservoir.	2
Pore pressure	Hydrostatic or lower	Above hydrostatic	Assumed hydrostatic, due to extension of the Stø-Tubåen formations outside the reservoir area and across the 3D-cube.	2
Average porosity	>25%	<25%	Measurements of 6-28% in 1S. Assumed 10% for reservoir in 1A.	1

Table 5-1: The table displays the structure of the reservoir, its belonging properties and chemical reactions within the reservoir. The table displays aquifer structuring, chemical properties, traps, reservoir volume, N/G, depth, homogeneity, pore pressure and average porosity together with high (e.g. 3) - and low (e.g. 0) quality-examples. A short description of reservoir is included. Table is modified after Halland et al. (2013).

Sealing Properties	High Quality	Low Quality	Unacceptable Values	Reservoir Properties	Quality number
Sealing layer	More than one seal	One seal	No known sealing layers	Overburden above the cap rock are most likely contributing to an additional seal. Salt domes are considered reliable sealing mechanisms in general, but salt and CO_2 have unfortunate chemical reactions increases chance of salt precipitation near injection well.	1
Properties of seal	Proven pressure barriers/ >100m thickness	<100m thickness		The cap rock is 47-65m. The Hekkingen Formation is generally considered a tight cap rock within The Barents Sea. Chemical reactions with salt, carbonate and CO_2 may result in leakage through or beyond cap rock extent.	0
Composition of seal	Homogenous, high clay content	Silty seal or silty layers within seal		High clay content within cap rock. Homogeneity is assumed for the whole cap rock.	2
Faults	No faulting through seal	Big throw through seal	Tectonically active faults	No active faults. Throw through seal at the edges (penetrates the northern- and the southern anticline and the fault-complex), but faults are considered tight. Cap rock is only penetrated by faults at outer boundaries.	1
Wells (exploration/pr oduction)	No drilling through seal	High number of drilled wells		A slight risk of leakage through the blocked 1S. Other wells in the area, 7227/11 is considered too far away to be a risk.	2
Other breaks through seal	No fractures	Sand injections etc.	Active chimney with gas leakage	No other known breaks through seal	3

Table 5-2: The table displays risks related to holding the CO_2 in place after injection. The risks are related to other wells, faults, salt domes and the cap rock. The table displays sealing layers, properties of seal, composition of seal, faults, wells and other breaks through seal, together with high (e.g. 3)- and low (e.g. 0) quality-examples. A short description of the reservoir is included. Table is modified after Halland et al. (2013).

Discussion

6   Conclusion

The interval of The Stø Formation, The Nordmela Formation and The Tubåen Formation is considered the most suitable reservoir for CO_2-storage. This interval consists of clean, homogenous sandstone (113m), with a small permeability barrier within The Tubåen Formation (20m).

The CO_2 will be stored in a salt-related trap, formed by two salt domes, and held in place by a suitable cap rock. The cap rock consists of The Hekkingen Formation and The Fuglen Formation, with a tight, homogenous shale-content. The cap rock is assumed to cover the whole reservoir and have a satisfying thickness throughout (approximately 50m).

The storage potential of the reservoir is 5.04Mt. The storage potential is relatively small, about a tenth of the Sleipner- and the Snøhvit sites. The reservoir has a limited salt-contact, where the reservoir is bound by faulted anticlines and a fault-complex in horizontal directions. The penetrating faults, at the outer reservoir boundaries, are inactive and tight. The maximum injection depth is 1375ms TWT.

The injected CO_2 will most likely have chemical reactions with the salt domes and a carbonate rock. The carbonate is not recognizable from seismic and the extent is not known. The largest risks of chemical reactions are related to salt precipitation within the reservoir and dissolution of the carbonate rock.

References

ANDREASSEN, K. 2009. Marine Geophysics, PP 1-54. *Marine Geophysics, Lecture Notes for GEO-3123.* University of Tromsø.

BACHU, S. 2000. Sequestration of CO2 in geological media: criteria and approach for site selection in response to climate change. *Energy Conversion and Management,* 41**,** 953-970.

BACHU, S., GUNTER, W. D. & PERKINS, E. H. 1994. Aquifer disposal of CO2: Hydrodynamic and mineral trapping. *Energy Conversion and Management,* 35**,** 269-279.

BAKLID, A. & KORBØL, R. 1996. Sleiper Vest CO2 Disposal, CO2 Injection into a shallow underground Aquifer, PP 1-4. *SPE Annual Technical Conference and Exhibition.* Denver, Colorado: STATOIL, SINTEF.

BRAATHEN, A., BÆLUM, K., CHRISTIANSEN, H. H., DAHL, T., EIKEN, O., ELVEBAKK, H., HANSEN, F., HANSSEN, T. H., JOCHMANN, M. & JOHANSEN, T. A. 2012. The Longyearbyen CO2 Lab of Svalbard, Norway - Initial Assessment of the Geological Conditions for CO2 Sequestration, PP 353-376.

BRUANT, R. G., JR, JR., CELIA, M. A., GUSWA, A. J. & PETERS, C. A. 2002. Peer Reviewed: Safe Storage of CO2 in Deep Saline Aquifers. *Environmental Science & Technology,* 36**,** 240-245.

BRUVOLL, A. & LARSEN, B. M. 2004. Greenhouse gas emissions in Norway: do carbon taxes work? *Energy Policy,* 32**,** 493-505.

BUGGE, T., ELVEBAKK, G., FANAVOLL, S., MANGERUD, G., SMELROR, M., WEISS, H. M., GJELBERG, J., KRISTENSEN, S. E. & NILSEN, K. 2002. Shallow stratigraphic drilling applied in hydrocarbon exploration of the Nordkapp Basin, Barents Sea. *Marine and Petroleum Geology,* 19**,** 13-37.

BÜENZ, S., FAVEROLA, A. P. & PANIERI, G. 2014. *RE: Lecture Notes from GEO-3151.*

BÖHRINGER, C., RUTHERFORD, T. F. & TOL, R. S. J. 2009. THE EU 20/20/2020 targets: An overview of the EMF22 assessment. *Energy Economics,* 31, Supplement 2**,** S268-S273.

CHADWICK, R. A., ZWEIGEL, P., GREGERSEN, U., KIRBY, G. A., HOLLOWAY, S. & JOHANNESSEN, P. N. 2004. Geological reservoir characterization of a CO2 storage site: The Utsira Sand, Sleipner, northern North Sea. *Energy,* 29**,** 1371-1381.

CO2 CRC LIMITED. 2011. *CCS facilities* [Online]. Available: http://www.co2crc.com.au/images/imagelibrary/gen_diag/ccs_facilities_media.jpg [Accessed 26 January 2015].

COHEN, J. E. 2010. Population and Climate Change. *Proceedings of the American Philosophical Society,* 154**,** 158-182.

CROSSLEY, N. 1998. Conversion of LPG Salt Caverns to Natural Gas Storage" A TransGas Experience". *Journal of Canadian Petroleum Technology,* 37**,** 37-47.

DEPARTMENT OF ECOLOGY. n.d. *What is Climate Change?* [Online]. Washington State: Access Washington. Available: http://www.ecy.wa.gov/climatechange/whatis.htm [Accessed 19 January 2015].

ESTUBLIER, A. & LACKNER, A. S. 2009. Long-term simulation of the Snøhvit CO2 storage. *Energy Procedia,* 1**,** 3221-3228.

GLOBALIS. n.d. *Kyoto-protokollen* [Online]. Available: http://www.globalis.no/Avtaler/Kyoto-protokollen [Accessed 22 January 2015].

GRUDE, S., LANDRØ, M. & OSDAL, B. 2013. Time-lapse pressure–saturation discrimination for CO2 storage at the Snøhvit field. *International Journal of Greenhouse Gas Control,* 19**,** 369-378.

HALLAND, E. K., BJØRNESTAD, A., GJELDVIK, I. T., BJØRHEIM, M., MAGNUS, C., MELING, I. M., MUJEZINOVIC, J., RIIS, F., RØD, R. S., PHAM, V. T. H. & TAPPEL, I. 2013. *CO2 Storage Atlas The Nowegian Continental Shelf, PP 20-144,* Norway, The Norwegian Petroleum Directorate.

HANSEN, O., EIKEN, O., ØSTMO, S., JOHANSEN, R. I. & SMITH, A. 2011. Monitoring CO2 Injection into a Fluvial Brine-filled Sandstone Formation at the Snøhvit Field, Barents Sea, PP 1-4. 4.

HANSEN, O., GILDING, D., NAZARIAN, B., OSDAL, B., RINGROSE, P., KRISTOFFERSEN, J.-B., EIKEN, O. & HANSEN, H. 2013. Snøhvit: The History of Injecting and Storing 1 Mt CO2 in the Fluvial Tubåen Fm. *Energy Procedia,* 37**,** 3565-3573.

HENRIKSEN, E., BJØRNSETH, H. M., HALS, T. K., HEIDE, T., KIRYUKHINA, T., KLØVJAN, O. S., LARSSEN, G. B., RYSETH, A. E., RØNNING, K., SOLLID, K. & STOUPAKOVA, A. 2011a. Chapter 17 Uplift and erosion of the greater Barents Sea: impact on prospectivity and petroleum systems. *Geological Society, London, Memoirs,* 35**,** 271-281.

HENRIKSEN, E., RYSETH, A. E., LARSSEN, G. B., HEIDE, T., RØNNING, K., SOLLID, K. & STOUPAKOVA, A. V. 2011b. Chapter 10 Tectonostratigraphy of the greater Barents Sea: implications for petroleum systems. *Geological Society, London, Memoirs,* 35**,** 163-195.

HERMANRUD, C., ANDRESEN, T., EIKEN, O., HANSEN, H., JANBU, A., LIPPARD, J., BOLÅS, H. N., SIMMENES, T. H., TEIGE, G. M. G. & ØSTMO, S. 2009. Storage of CO2 in saline aquifers–Lessons learned from 10 years of injection into the Utsira Formation in the Sleipner area. *Energy Procedia,* 1**,** 1997-2004.

HERZOG, H. J. 1998. The Economics of CO2 Capture, PP 1-4. *In:* LABORATORY, M. I. O. T. M. E. (ed.) *The Fourth International Conference on Greenhouse Gas Control Technologies.* Interlaken, Switzerland.

HOLLOWAY, S. 2005. Underground sequestration of carbon dioxide—a viable greenhouse gas mitigation option. *Energy,* 30**,** 2318-2333.

HOTINSKI, R. 2011. *Carbon Mitigation Initiative, PP 1-8* [Online]. Princeton University. Available: http://cmi.princeton.edu/wedges/ [Accessed 21 January 2015].

IPCC 2005. IPCC Special Report on Carbon Dioxide Capture and Storage. Prepared by Working Group III of the Intergovernmental Panel on Climate Change, PP 1-442 [Metz, B., O. Davidson, H. C. de Coninck, M. Loos, and L. A. Meyer (eds.)]. The United States of America: Cambridge University Press, Cambridge, United Kingdom and New York, NY, U.S.A.

IPCC 2007. Climate Change 2007: Mitigation. Contribution of Working Group III to the Fourth Assessment Report of the Intergovernmental Panel on Climate Change, PP 1-862 [B. Metz, O.R. Davidson, P.R. Bosch, R. Dave, L.A. Meyer (eds)]. *In:* C. U. PRESS ED. (ed.). Cambridge University Press, Cambridge, United Kingdom and New York, NY, U.S.A.

IPCC 2014. Climate Change 2014: Mitigation of Climate Change. Contribution of Working Group III to the Fifth Assessment Report of the Intergovernmental Panel on Climate Change, PP 1-688 [Edenhofer, O., R. Pichs-Madruga, Y. Sokona, E. Farahani, S. Kadner, K. Seyboth, A. Adler, I. Baum, S. Brunner, P. Eickemeier, B. Kriemann, J. Savolainen, S. Schlömer, C. von Stechow, T. Zwickel and J.C. Minx (eds.)]. Cambridge University Press, Cambridge, United Kingdom and New York, NY, U.S.A.

IZGEC, O., DEMIRAL, B., BERTIN, H. J. & AKIN, S. 2006. Experimental and Numerical Modeling of Direct Injection of CO2 Into Carbonate Formations PP 1-16. *SPE Annual Technical Conference and Exhibition.* San Antonio, Texas, U.S.A.: Society of Petroleum Engineers.

KAWAKITA, K. & TSUTSUMI, Y. 1966. A Comparison of Equations for Powder Compression. *Bulletin of the Chemical Society of Japan,* 39**,** 1364-1368.

KOEIJER, D. G. D., HELLEVANG, H., RIIS, F., TITLESTAD, G. O., AAGAARD, P., KÅRSTAD, O., TVERANGE, J., OLAUSSEN, S. & JOCHMANN, M. 2013. *RE: Geological Constrains of CO2 Sequestration. Lecture Notes from AG-341.*

LARSSEN, G. B., ELVEBAKK, G., HENRIKSEN, L. B., KRISTENSEN, S.-E., NILSSON, I., SAMUELSBERG, T. J., SVÅNÅ, T. A., STEMMERIK, L. & WORSLEY, D. 2002. *Upper Paleozoic Lithostratigraphy of the Southern Norwegian Barents Sea, PP 1-53* [Online]. NPD. Available: http://www.nhm2.uio.no/norges/litho/Barents/intro/geology.html#Nordkapp [Accessed 5 February 2015].

LINDEBERG, E., VUILLAUME, J.-F. & GHADERI, A. 2009. Determination of the CO2 storage capacity of the Utsira formation. *Energy Procedia,* 1**,** 2777-2784.

LIU, H. & LIANG, X. 2011. Strategy for promoting low-carbon technology transfer to developing countries: The case of CCS. *Energy Policy,* 39**,** 3106-3116.

LOKHORST, A. & WILDENBORG, T. 2005. Introduction au stockage géologique du CO2 - Classification des options de stockage. *Oil & Gas Science and Technology - Rev. IFP,* 60**,** 513-515.

MAIER-REIMER, E. & HASSELMANN, K. 1987. Transport and storage of CO2 in the ocean ——an inorganic ocean-circulation carbon cycle model. *Climate Dynamics,* 2**,** 63-90.

MALDAL, T. & TAPPEL, I. M. 2004. CO2 underground storage for Snøhvit gas field development. *Energy,* 29**,** 1403-1411.

MARSHALL, J. & PLUMB, R. A. 2008. *Atmosphere, Ocean and Climate Dynamics. An Introductory Text, PP 1-307,* London, United Kingdom, Elsevier.

MCKERROW, W. S., MAC NIOCAILL, C. & DEWEY, J. F. 2000. The Caledonian Orogeny redefined. *Journal of the Geological Society,* 157**,** 1149-1154.

MULLER, N., QI, R., MACKIE, E., PRUESS, K. & BLUNT, M. J. 2009. CO2 injection impairment due to halite precipitation. *Energy Procedia,* 1**,** 3507-3514.

NICHOLS, G. 2009. *Sedimentology and stratigraphy, PP 385-393*, John Wiley & Sons.

NPD. 2015. *Wellbore Fact Pages* [Online]. www.npd.no: NPD. Available: http://factpages.npd.no/FactPages/default.aspx?nav1=discovery&nav2=PageView%7cAll&nav3=1630384 [Accessed 2 February 2015].

OSDAL, B., ZADEH, H. M., JOHANSEN, S. & GILDING, D. 2013. CO2 Saturation and Thickness Prediction from 4D Seismic Data at Snøhvit Field, PP 1-4. *75th EAGE Conference & Exhibition incorporating SPE EUROPEC 2013.* London, UK: EAGE.

OSDAL, B., ZADEH, M., JOHANSEN, S., GONZALEZ, R. R. & WÆRUM, G. O. 2014. Snøhvit CO2 Monitoring using Well Pressure Measurement and 4D seismic, PP 2-5. *Fourth EAGE CO2 Geological Storage Workshop Demonstrating Storage Integrity and Building Confidence in CCS.* Stavanger, Norway: EAGE.

POTERBA, J. M. 1991. Tax Policy to Combat Global Warming: On Designing a Carbon Tax, PP 1-42. *National Bureau of Economic Research Working Paper Series,* No. 3649.

PRUESS, K. 2008. On CO2 fluid flow and heat transfer behavior in the subsurface, following leakage from a geologic storage reservoir. *Environmental Geology,* 54**,** 1677-1686.

RAFAELSEN, B. 2005. Seismic resolution and frequency filtering, PP 1-4. *Mat. Svalex*.

RIDER, M. H. 1986. *The Geological Interpretation of Well Logs, PP 1-192,* New York, U.S.A., John Wiley and Sons, Inc.

SCHLUMBERGER 2011. *Petrel Geophysics, PP 223-229,* Houston, USA, Schlumberger.

SCHLUMBERGER. 2015. *Oilfield Glossary* [Online]. Available: http://www.glossary.oilfield.slb.com/en/ [Accessed 20.04 2015].

SELLEY, R. C. & SONNENBERG, S. A. 1998. *Elements of Petroleum Geology, PP 7-455,* San Diego, USA, Academic Press.

SIVERTSEN, A. & HOMMEDAL, M. 2013. *Kampen mot CO2-klokka* [Online]. Available: http://www.npd.no/no/Tema/Lagring-og-bruk-av-CO2/Temaartikler/Kampen-mot-CO2-klokka/ [Accessed 4 February 2015].

THE NATIONAL RESEARCH COUNCIL 1984. On Changing Climate. *Population and Development Review,* 10**,** 161-167.

WISCHNEWSK, B. n.d. *Calculation of thermodynamic state variables of carbon dioxide* [Online]. Available: http://www.peacesoftware.de/einigewerte/co2_e.html [Accessed 16.04 2015].